Modeling and Characterization of Rate Phenomena in Complex Electrochemical Systems: Sodium-Metal Chloride Batteries and Ni/SiC Co-Deposition

Damla Eroglu

Submitted in partial fulfillment of the
requirements for the degree of
Doctor of Philosophy
in the Graduate School of Arts and Sciences

COLUMBIA UNIVERSITY

2013

© 2013

Damla Eroglu

All rights reserved

ABSTRACT

Modeling and Characterization of Rate Phenomena in Complex Electrochemical Systems: Sodium-Metal Chloride Batteries and Ni/SiC Co-Deposition

Damla Eroglu

In the first part of the dissertation (Chapters 3-5), the effect of a cationic dispersant, polyethyleneimine (PEI) on the co-deposition of micro and nano SiC particles with nickel is characterized and modeled. A major challenge in Ni/SiC co-deposition for wear-resistant coatings is that the dispersants that are used to stabilize the particles in the electrolyte to ensure high and uniform particle incorporation into the deposit can significantly affect the electrodeposition kinetics. To overcome this challenge, studies of particle dispersion and electrodeposition are integrated. The effect of PEI on the electrodeposition of Ni/SiC composites is characterized as a function of SiC and PEI bath concentration, current density, rotation speed, molecular weight of PEI and particle size. A pre-coating procedure, in which SiC particles are pre-coated with PEI in a different electrolyte prior to plating, is described. With the pre-coating procedure, high particle stability in the plating bath is obtained. In addition, a significant increase on the SiC incorporation rate is seen without any substantial decrease on the current efficiency for both micro- and nano-composites. Furthermore, using pre-coated particles in the presence of a leveling agent is found to be advantageous relative to the direct addition of PEI into the electrolyte. The efficacy of employing the pre-coating procedure in manufacturing, where plating baths need a long life, is also found to be satisfactory. The use of pre-coated SiC particles changes the morphology, decreases the surface roughness and

increases the hardness of the deposits for both particle sizes. Finally, a mathematical model of the co-deposition is proposed. The rate of incorporation is proportional to the residence time, inversely proportional to the burial time, and is proportional to the number density of particles on the surface. These times are influenced by the hydrodynamics, particle size, current density, and concentration of dispersants. SiC incorporation increases with the introduction of PEI due to an increase in the residence time of the particles on the surface.

In the second part of the dissertation, a sodium-metal chloride battery, which is another important complex electrochemical system, is studied. A one-dimensional mathematical model of the porous cathode of a sodium-iron chloride battery for an isothermal, constant-current discharge-charge cycle is presented. In sodium-iron chloride batteries, it is desirable to maintain low $FeCl_2$ solubility to minimize redistribution of active material in the cell. However, the iron chloride is sparingly soluble, and with increased cycling, it does redistribute. None of the previous models can predict this movement of the metal that takes place in the cell with increased cycling that can cause the failure of the cell. An advance offered by the model presented is that it accounts for the change in the solubility of $FeCl_2$ within the cell and predicts the relocation of the iron by including the flux of a sparingly soluble ferrous complex. For instance, the model predicts that at the end of the fifth cycle, the iron amount decreases by ~1% near the sodium tetrachloroaluminate reservoir.

TABLE OF OF CONTENTS

LIST OF FIGURES

Chapter 1

Chapter 2

Chapter 3

Chapter 5

LIST OF TABLES

ACKNOWLEDGMENTS

I would like to express my deepest gratitude to my advisor Prof. Alan C. West for his guidance, support and patience throughout my thesis. He guided me with his valuable advice and enthusiasm in every step. I am very grateful to do my PhD under the tutelage of such a great mentor.

I also wish to thank to our collaborators Prof. Ponisseril Somasundaran and Dr. Annamaria Vilinska for their help and enthusiasm throughout this study. Special thanks to The Boeing Company; this work is primarily funded by them. I would also like to thank to all the past and current members of the West group, especially to Dr. Robert von Gutfeld, Dr. Igor Volov, Feng Qiao, Derek Sun, Ruixing Zhu, Roel Mercado and Kevin Knehr for their support and friendship. Special thanks to Dr. Asli Sahin not only for her help and support throughout my studies but also for her great friendship.

I want to thank to my family, Inci, Mehmet and Cagla Eroglu for their endless love and support in every step of my life. I could not achieve any of these without their belief in me. Finally, I want to express my deepest gratitude to Aytug Pala, who has supported me in every step with his love, patience, understanding and encouragement.

CHAPTER 1

INTRODUCTION

1.1. Ceramic Particle Incorporation Into Electrodeposited Films

1.1.1. Ni/SiC Co-Deposition Overview

The use of nickel/silicon carbide composites as coatings has attained a great significance in the last decade as a result of their high anti-wear, hardness, and anti-corrosion properties [1-17]. Electrochemical deposition of nickel and silicon carbide as a means of producing these composites has the advantage of low cost and operating temperature [13].

The schematic diagram of the co-deposition process can be seen in Figure 1.1. During co-deposition, SiC particles are incorporated into the growing Ni film in the presence of dispersants and plating additives. Dispersants are added to stabilize the ceramic particles in the electrolyte whereas plating additives are present to control the final film properties [18]. The hydrogen evolution reaction is inevitable during Ni deposition because of its thermodynamic potential. Therefore the current efficiency, which is the percentage of the total current that goes into nickel deposition, is significant [18]. The reactions on the electrode surface are:

$$Ni^{+2} + 2e^{-} \rightarrow Ni \quad (1)$$

$$2H^{+} + 2e^{-} \rightarrow H_2 \quad (2)$$

with thermodynamic cell potentials of -0.46 V and -0.49 V vs Ag/AgCl at a pH of 4.4, respectively [19].

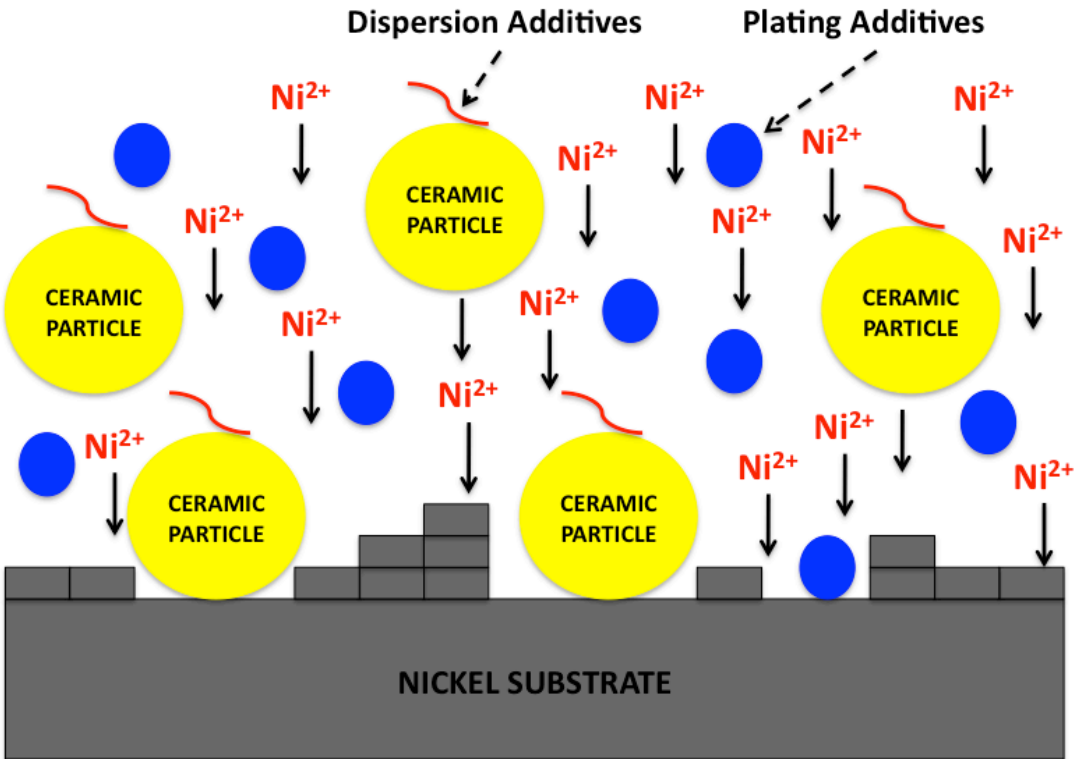

Figure 1.1. Schematic diagram of Ni/SiC co-deposition. SiC particles are incorporated into growing Ni film in the presence of dispersants and plating additives.

The amount and uniformity of the SiC particles in the deposit have an effect on a film's tribological and mechanical properties. Therefore, improving the dispersion of SiC particles in the plating bath and controlling the amount of SiC particles co-deposited with nickel are two keys to obtaining enhanced composite properties [13]. Previous studies show that the amount of SiC particles in the deposit depends on the particle characteristics (size, surface properties, concentration), operating parameters (current density, temperature, hydrodynamics, electrodeposition technique) and plating bath properties (bath type, concentration, pH, presence of dispersion and plating additives) [10, 16].

The effect of ceramic particle concentration in the plating bath is one of the most commonly investigated variables [1, 3-9, 11, 14]. In most of the studies, it is observed that the volume fraction of SiC in the film increases with increasing SiC bath concentration up to a point, and does not change any further at higher concentrations. Current density has also been widely investigated [1, 7, 8, 12, 14]; however, its effect depends on the other system variables such as particle type and size and rotation speed, and generalized trends have been difficult to ascertain. Agitation in the plating bath also has a significant effect [7, 8, 20]. It is seen that the amount of ceramic particle in the deposit increases with increasing stirring rate up to an optimum value, and beyond this rate of stirring, any further increase in mixing causes the SiC incorporation to decrease.

The size of the ceramic particle is another variable that affects the co-deposition significantly; nano-particle composites often have superior mechanical and tribological properties compared to micro-particle composite films [5, 10, 21, 22]. However, lower SiC fractions in the deposit have been seen for these smaller particles [5, 10]. Decreasing the agglomeration of the particles in the electrolyte and increasing the particle incorporation into the deposit are two main challenges for nano-composites.

1.1.2. Previous Studies on Ni/SiC Co-Deposition in the Presence of Dispersants

The type and concentration of the dispersion additive plays a crucial role in co-deposition. Stabilization of the particles in the plating bath can result in higher and more uniform ceramic particle incorporation [5, 6, 8, 11, 12, 14]. Both cationic and anionic dispersants are investigated in the literature for Ni/SiC co-deposition as shown in Table 1.1.

Cationic additives not only prevent the agglomeration of the ceramic particles but also result in more positively charged SiC particles with higher affinity to the cathode [5, 11, 12, 23]. In most of the studies it has seen that ceramic particle amount in the deposit increases with increasing dispersant concentration in the plating bath [1, 5, 6, 14, 23]. However, some of the studies show that increasing the additive concentration beyond an optimum leads to a decrease in SiC volume fraction [11, 12].

Table 1.1. Dispersants investigated in the literature for Ni/SiC co-deposition.

Anionic Dispersants	*Cationic Dispersants*
Sodium dodecylsulfate [1, 23]	Cationic surfactant AZTAB [11, 12]
Sodium hexanitrocobaltate [14]	Cetyltrimethylammonium bromide [5, 6]
Xanthan gum [8]	Hexadecylpyridinium bromide [23]

Polyethyleneimine (PEI) is a cationic polymer that was previously investigated as a dispersant for aqueous SiC suspensions [24-28]. These studies indicate that PEI is an effective dispersant for SiC particles in aqueous media [24, 26, 28]. In addition to dispersion studies, PEI has also been investigated as a suppressor in copper and nickel electrodeposition [29, 30]. However, the effect of PEI on Ni/ceramic particle co-deposition has not been investigated.

1.1.3. Previous Studies on the Modeling of Ceramic Particle Incorporation into Electrodeposited Films

Although there are many experimental studies on ceramic particle incorporation, mechanistic studies have been somewhat limited [8, 14, 31-37]. The effect of critical variables such as ceramic particle bath concentration, current density, hydrodynamic conditions, and particle size are known as described in the previous section. Yet, qualitative experimental trends may be difficult to predict, and explaining these effects theoretically is still a major challenge [8, 14, 31-37]. The existing models in the literature explain the incorporation mainly through the emphasis of (1) electrophoresis, (2) mechanical entrapment, (3) particle adsorption, or (4) mass transfer [16, 36].

Guglielmi has proposed a mechanism based on a two-step adsorption process [32]. In the first step, the particles are loosely adsorbed on the cathode. This step is purely physical in nature. Guglielmi proposed that the loosely adsorbed particles are in equilibrium with the suspension and therefore the loose adsorption coverage can be expressed with a classical Langmuir adsorption isotherm. In the second adsorption step, some fraction of these loosely adsorbed particles is incorporated irreversibly into the metal film. This second step takes electrophoresis into account and depends on the electrode overpotential [32]. Guglielmi's model has been adopted by many researchers. For instance, Celis and Roos [34] have suggested that the model is valid for the incorporation of Al_2O_3 particles into copper films. In their study, it was concluded that the second adsorption step is rate-determining [34]. Guglielmi's model describes the effect of ceramic-particle bath concentration and current density on the incorporation rate, however it does not include hydrodynamic effects and is not readily extended to

account for particle characteristics [16]. Bercot et al. [31] modified Guglielmi's model by incorporating a corrective factor which is a function of the rotation speed and particle bath concentration. Hwang and Hwang [36] also developed a mechanism based on the work of Guglielmi. The model proposed that the particles in the suspension are surrounded by an adsorbed layer of ions. These particles are incorporated into the metal film through a three-step process: (1) forced convection to the electrode, (2) loose adsorption on the electrode surface and (3) irreversible incorporation as a result of reduction of the adsorbed ions on the particle [36].

Celis et al. [34] have also described the incorporation process by the formation of an adsorbed layer of ions around the particles, mass transfer, and irreversible incorporation of the particles by the reduction of adsorbed ions. The model is based on a statistical approach; with a probability of particle incorporation assumed to be a function of the amount of adsorbed ions on the particle.

Fransaer et al. [35] have used trajectory analysis to model the incorporation of non-brownian particles on a rotating disk electrode. In their model, a force balance on the particle near the surface defines the incorporation rate. If the sum of the stagnation and adhesion forces on the particle is larger than the shear force, the particle is immobilized and gets incorporated. Maurin and Lavanant [8] also adopted the Fransaer model to explain the effect of rotation speed on the incorporation rate.

Vereecken et al. [33] developed an incorporation model based on convective-diffusion of the particles to the electrode surface. At low current densities, a particle on the surface is either incorporated or desorbs, whereas at large current densities all the particles on the surface are assumed to be buried in the growing metal film. Shao et al.

[37] modified Vereecken's mechanism by accounting for a gravitational force acting on the particles in the reverse direction of the diffusion force.

1.1.4. Scope of Current Work

A key challenge in electrolyte design for Ni/SiC co-deposition is that dispersants that improve the stability of the particles may also have a significant effect on the electrodeposition kinetics. This may impact the robustness of the process especially for complex geometries and may lead to hydrogen embrittlement, a concern for many applications. To overcome this challenge, studies of particle dispersion and electrodeposition need to be integrated.

In the first part of this dissertation, the effect of a cationic polymer, polyethyleneimine (PEI) on Ni/SiC co-deposition is discussed. An integrated research methodology that considers both particle dispersion and electrodeposition in the presence of PEI is described. Chapter 3 discusses the incorporation of micron-sized (1 μm) SiC particles into Ni film in the presence of PEI. The effect of PEI concentration and molecular weight on the SiC incorporation in the deposit is examined. In addition, the effect of system variables such as SiC bath concentration, current density, and rotation speed on the SiC incorporation in the deposit is explored. A pre-coating procedure, in which significant increase in SiC incorporation and high particle stability in the plating bath is seen without any decrease in the current efficiency, is described. In addition, the efficacy of the pre-coating procedure after significant bath aging and in the presence of a leveling agent is discussed.

In Chapter 4, the pre-coating procedure described in Chapter 3 for micro-particle composites is extended to nano-particle incorporation. The effect of pre-coating on Ni/SiC co-deposition is characterized based on current efficiency measurements and the SiC fraction in the deposit. Finally, the morphological properties of the micro- and nano-composites are compared.

After the effect of PEI on the incorporation of micro and nano SiC particles into Ni is discussed in Chapters 3 and 4, a model that describes the Ni/SiC co-deposition in the presence of PEI is proposed in Chapter 5. Although previous mechanisms proposed in the literature explain the effect of system variables such as current density and SiC bulk concentration, none discuss the effect of a dispersant on the incorporation rate. In Chapter 5, a mass-transfer/adsorption model of Ni/SiC co-deposition on a rotating disk electrode that provides a framework to interpret the increase of the incorporation rate due to a cationic dispersant is proposed. The effect of current density, rotation speed, SiC bath concentration and particle size on the incorporation rate is used to test and validate the model.

1.2. Modeling of Reaction Kinetics and Transport in the Positive Porous Electrode in a Sodium-Iron Chloride Battery

1.2.1. Sodium-Metal Chloride Batteries Overview

Advanced secondary battery technologies have been investigated for well over a decade due to diverse applications, which appear to be continuously increasing. Sodium-beta batteries are high-temperature secondary battery systems, with significant promise

for high-energy density applications requiring long cycle life [38-49]. The main characteristic of these cells is the use of liquid sodium and a β"-alumina (β"-Al_2O_3) solid electrolyte [38-50]. The two most common sodium-beta batteries are the sodium-sulfur battery [51] and the sodium-metal chloride battery [38]. Sodium-metal chloride batteries have superior properties over sodium-sulfur batteries such as higher open-circuit cell potentials, wider operating temperature range, safer reaction products, less risk of metallic corrosion, more tolerance to overcharge and overdischarge and a safer failure mode [43, 49, 50]. Sodium-metal chloride batteries also have zero self-discharge and are unaffected by the ambient temperature [44, 48].

The sodium-metal chloride battery contains a liquid sodium electrode and a β"-alumina solid electrolyte, like the sodium-sulfur battery [38-49]. It also contains a second, molten salt electrolyte, sodium tetrachloroaluminate ($NaAlCl_4$), and a porous metal/metal chloride electrode [38-49]. The β"-alumina solid electrolyte only allows Na^+ ions to pass and it has essentially zero electronic conductivity [47-49]. The liquid electrolyte connects the ceramic electrolyte to the metal-chloride electrode for the rapid transport of Na^+ [38-49].

The schematic diagram of a sodium-metal chloride cell is seen in Figure 1.2. There is a positive current collector in the middle of the cell surrounded by the cathode, which consists of the electrode matrix (metal/metal chloride and NaCl) impregnated with molten $NaAlCl_4$. The cathode fills the β"-alumina tube, which separates the liquid sodium anode from the cathode. The sodium anode resides between the β"-alumina tube and the steel outer case, which also acts as the negative current collector [38-50, 52, 53].

These batteries operate in the range of 270-350 ^{0}C since high temperatures are needed to melt the sodium tetrachloroaluminate [38, 41, 48, 49]. In addition, the resistance of the solid electrolyte is low in this temperature range [41, 47-49]. An important feature of these batteries is that even at these high temperatures, the electrodes and the liquid electrolyte do not cause high pressures inside the cell [38].

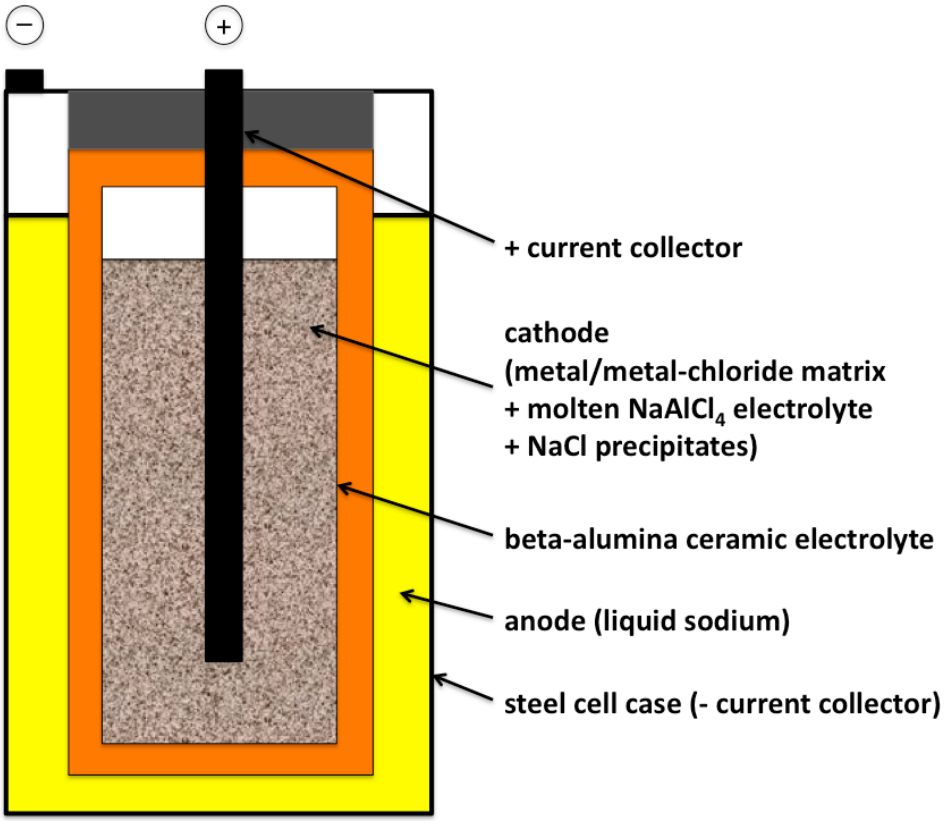

Figure 1.2. Schematic diagram of a sodium-metal chloride cell.

Metal chloride cells are assembled in the discharged state by mixing the metal powder with NaCl in the positive electrode and adding the salt electrolyte as a dry powder to the mixture. After heating the cell to the operating temperature, it is then charged to generate the liquid sodium and metal chloride [42-46, 49]. Iron chloride and

nickel chloride are the most common electrodes used in these cells [38, 40, 41, 49]. In the second part of this dissertation, the iron chloride electrode is considered.

During discharge, sodium ions migrate through the ceramic electrolyte from the negative electrode and then transferred to the positive electrode through the sodium tetrachloroaluminate. Sodium reacts with iron chloride on the electrode to produce sodium chloride and iron. The battery is fully discharged when there is no iron chloride left in the cell [38-49, 52, 53]. The reverse of this process occurs during charging. The overall cell reaction is (1):

$$2Na + FeCl_2 \underset{CHARGING}{\overset{DISCHARGING}{\longleftrightarrow}} 2NaCl + Fe \tag{3}$$

with a thermodynamic cell potential of 2.35 V at 250 ^{0}C [38, 39, 41, 44, 49, 54, 55].

Sodium tetrachloroaluminate is a mixture of two binary molten salts, NaCl and $AlCl_3$, and the apparent concentration ratio of NaCl to $AlCl_3$ determines the solubility of $FeCl_2$ in the electrolyte [56]. NaCl-rich melts are typically used [52, 54, 56], in part because it is desirable to maintain low $FeCl_2$ solubility to minimize redistribution of active material. Nevertheless, the iron chloride is sparingly soluble, and with increased cycling, it does redistribute. The migration of the metal in the cell results in a loss in the performance of the battery, and may be a crucial failure mechanism [46, 49, 54, 57, 58].

1.2.2. Previous Studies on the Modeling of Sodium-Metal Chloride Batteries

In the literature, there are many studies on battery modeling [52, 53, 55, 59-67]. Modeling of the reaction kinetics and transport processes in the cell is critical to predict the change of cell potential with the depth of discharge and to evaluate the outcomes of the changes in design parameters that affect the battery performance [52, 65]. Although

there are many studies on the modeling of secondary lithium batteries [59, 60, 62-64], the modeling of sodium-metal chloride batteries is more limited [52, 53, 55, 65]. Sudoh and Newman [52] discuss a very detailed model of a discharge-charge cycle of a Na/β"-Al_2O_3/$NaAlCl_4$/$FeCl_2$ battery based on the macroscopic theory of porous electrodes [68] and concentrated solution theory [69]. In their model, the precipitation/dissolution rate of NaCl is taken into account. In addition, the mass transfer of the soluble ferrous complex is included in the electrode rate reaction [52], however they do not allow for redistribution within the cell via transport of the iron species through the electrolyte.

Bloom et al. [55] simulated the discharge of sodium-nickel chloride cells with a model that does not include the solubility of $NiCl_2$ and NaCl. Orchard and Weaving [65], also published a model describing the discharge of sodium-iron chloride cells. In this study, the solubility of $FeCl_2$ and NaCl were not considered. Vallance and White [53], modified Sudoh and Newman's model and created a two-dimensional model for a fluted β"-alumina tube.

1.2.3. Scope of Current Work

In sodium-metal chloride batteries, the important battery characteristics such as the battery performance, reliability and cycle life, depend mainly on the porous cathode. Therefore, in order to improve these properties, a better understanding of reaction kinetics and transport processes in the cathode is essential. The degradation mechanisms in the cathode, which cause the battery to fail with increased cycling, also need to be studied. Because of these reasons, electrochemical models of the porous cathode with improved reaction and degradation mechanisms and transport processes are required.

In Chapter 6, a mathematical model of the porous cathode of a Na/β"-Al_2O_3/$NaAlCl_4$/$FeCl_2$ battery during a discharge-charge cycle is presented. The cathode is modeled using the macroscopic theory of porous electrodes [68]. Transport processes are modeled using the Pollard and Newman's [69] concentrated-solution theory for a mixture of two binary molten salts in a porous electrode. Although the previous models [52, 53, 55, 65] are successful in defining the kinetics and transport in the cathode, none of them can predict the redistribution of material in the cathode [46, 49, 54, 57, 58]. An advance offered by the model described in this dissertation is that it accounts for the change in the solubility of $FeCl_2$ within the cell and predicts the relocation of the iron. Therefore, it provides an insight into one of the degradation mechanisms in the metal-chloride batteries.

1.3. References

1. L. Benea, P. L. Bonora, A. Borello, S. Martelli, F. Wenger, P. Ponthiaux and J. Galland, *Journal of the Electrochemical Society*, **148**, C461 (2001).

2. T. Borkar and S. P. Harimkar, *Surface and Coatings Technology*, **205**, 4124 (2011).

3. I. Garcia, J. Fransaer and J. P. Celis, *Surface and Coatings Technology*, **148**, 171 (2001).

4. E. Garcia-Lecina, I. Garcia-Urrutia, J. A. Diez, M. Salvo, F. Smeacetto, G. Gautier, R. Seddon and R. Martin, *Electrochimica Acta*, **54**, 2556 (2009).

5. M. D. Ger, *Materials Chemistry and Physics*, **87**, 67 (2004).

6. K. H. Hou, M. D. Ger, L. M. Wang and S. T. Ke, *Wear*, **253**, 994 (2002).

7. S. K. Kim and H. J. Yoo, *Surface and Coatings Technology*, **108-109**, 564 (1998).

8. G. Maurin and A. Lavanant, *Journal of Applied Electrochemistry*, **25**, 1113 (1995).

9. P. Nowak, R. P. Socha, M. Kaisheva, J. Fransaer, J. P. Celis and Z. Stoinov, *Journal of Applied Electrochemistry*, **30**, 429 (2000).

10. E. A. Pavlatou, M. Stroumbouli, P. Gyftou and N. Spyrellis, *Journal of Applied Electrochemistry*, **36**, 385 (2006).

11. N. K. Shrestha, M. Masuko and T. Saji, *Wear*, **254**, 555 (2003).

12. N. K. Shrestha, I. Miwa and T. Saji, *Journal of the Electrochemical Society*, **148**, C106 (2001).

13. M. Srivastava, V. K. William Grips and K. S. Rajam, *Materials Letters*, **62**, 3487 (2008).

14. S.-C. Wang and W.-C. J. Wei, *Materials Chemistry and Physics*, **78**, 574 (2003).

15. S. H. Yeh and C. C. Wan, *Journal of Applied Electrochemistry*, **24**, 993 (1994).

16. C. T. J. Low, R. G. A. Wills and F. C. Walsh, *Surface and Coatings Technology*, **201**, 371 (2006).

17. R. Orinakova, A. Turonova, D. Kladekova, M. Galova and R. Smith, *Journal of Applied Electrochemistry*, **36**, 957 (2006).

18. M. Schlesinger and M. Paunovic, *Modern Electroplating*, John Wiley & Sons, Inc., New York (2000).

19. A. C. West, *Electrochemistry and Electrochemical Engineering*, Charleston (2012).

20. I. Shao, P. M. Vereecken, C. L. Chien, P. C. Searson and R. C. Cammarata, *Journal of Materials Research*, **17**, 1412 (2002).

21. C. Cai, X. B. Zhu, G. Q. Zheng, Y. N. Yuan, X. Q. Huang, F. H. Cao, J. F. Yang and Z. Zhang, *Surface & Coatings Technology*, **205**, 3448 (2011).

22. C. Zanella, M. Lekka and P. L. Bonora, *Journal of Applied Electrochemistry*, **39**, 31 (2009).

23. L. Chen, L. Wang, Z. Zeng and J. Zhang, *Materials Science and Engineering: A*, **434**, 319 (2006).

24. J. Sun and L. Gao, *Journal of the European Ceramic Society*, **21**, 2447 (2001).

25. S. Baklouti, C. Pagnoux, T. Chartier and J. F. Baumard, *Journal of the European Ceramic Society*, **17**, 1387 (1997).

26. J. X. Zhang, D. L. Jiang, S. H. Tan, L. H. Gui and M. L. Ruan, *Journal of Materials Research*, **17**, 2012 (2002).

27. J. X. Zhang, Q. Xu, F. Ye, Q. L. Lin, D. L. Jiang and M. Iwasa, *Colloids and Surfaces a-Physicochemical and Engineering Aspects*, **276**, 168 (2006).

28. Y. H. Zhang and J. Binner, *Ceramics International*, **34**, 1381 (2008).

29. S. K. Kim, J. E. Bonevich, D. Josell and T. P. Moffat, *Journal of the Electrochemical Society*, **154**, D443 (2007).

30. S. K. Kim, D. Josell and T. P. Moffat, *Journal of the Electrochemical Society*, **153**, C616 (2006).

31. P. Bercot, E. Pena-Munoz and J. Pagetti, *Surface and Coatings Technology*, **157**, 282 (2002).

32. N. Guglielmi, *Journal of the Electrochemical Society*, **119**, 1009 (1972).

33. P. M. Vereecken, I. Shao and P. C. Searson, *Journal of the Electrochemical Society*, **147**, 2572 (2000).

34. J. P. Celis, J. R. Roos and C. Buelens, *Journal of the Electrochemical Society*, **134**, 1402 (1987).

35. J. Fransaer, J. P. Celis and J. R. Roos, *Journal of the Electrochemical Society*, **139**, 413 (1992).

36. B. J. Hwang and C. S. Hwang, *Journal of the Electrochemical Society*, **140**, 979 (1993).

37. I. Shao, P. M. Vereecken, R. C. Cammarata and P. C. Searson, *Journal of the Electrochemical Society*, **149**, C610 (2002).

38. J. Coetzer, *Journal of Power Sources*, **18**, 377 (1986).

39. R. J. Bones, J. Coetzer, R. C. Galloway and D. A. Teagle, *Journal of the Electrochemical Society*, **134**, 2379 (1987).

40. R. C. Galloway, *Journal of the Electrochemical Society*, **134**, 256 (1987).

41. J. L. Sudworth, *Journal of Power Sources*, **51**, 105 (1994).

42. P. A. Nelson, *Journal of Power Sources*, **29**, 565 (1990).

43. B. V. Ratnakumar, A. I. Attia and G. Halpert, *Journal of Power Sources*, **36**, 385 (1991).

44. J. L. Sudworth, *Philosophical Transactions of the Royal Society A: Mathematical, Physical and Engineering Sciences*, **354**, 1595 (1996).

45. A. Van Zyl, *Solid State Ionics*, **86-88**, 883 (1996).

46. J. L. Sudworth, *Journal of Power Sources*, **100**, 149 (2001).

47. C. H. Dustmann, *Journal of Power Sources*, **127**, 85 (2004).

48. T. M. O'Sullivan, C. M. Bingham and R. E. Clark, in *International Symposium on Power Electronics, Electrical Drives, Automation and Motion (SPEEDAM)*, p. 244, Italy (2006).

49. X. Lu, G. Xia, J. P. Lemmon and Z. Yang, *Journal of Power Sources*, **195**, 2431 (2010).

50. J. W. Braithwaite and W. L. Auxer, in *Handbook of Batteries*, 3rd ed., D. Linden and T. B. Reddy Editors, p. 40.1, McGraw-Hill, New York (2002).

51. J. L. Sudworth, *The sodium sulfur battery / J.L. Sudworth and A.R. Tilley*, Chapman & Hall, London ; New York : (1985).

52. M. Sudoh and J. Newman, *Journal of the Electrochemical Society*, **137**, 876 (1990).

53. M. A. Vallance and R. E. White, in *Comsol Conference*, Boston (2008).

54. R. J. Bones, D. A. Teagle, S. D. Brooker, F. L. Cullen and J. Lumsdon, in *2nd Symposium on Electrode Materials and Processes for Energy Conversion and Storage*, p. 537, Philadelphia (1987).

55. I. Bloom, P. A. Nelson, L. Redey, S. K. Orth, C. L. Hammer, R. S. Skocypec, D. W. Dees, M. C. Hash and D. R. Vissers, in *Proc. of 25th Intersoc. Energy Conversion Eng. Confer.*, p. 341, Reno, NV (1990).

56. L. G. Boxall, H. L. Jones and R. A. Osteryoung, *Journal of the Electrochemical Society*, **121**, 212 (1974).

57. R. J. Bones, D. A. Teagle, S. D. Brooker and F. L. Cullen, *Journal of the Electrochemical Society*, **136**, 1274 (1989).

58. J. S. Weaving and S. Walter Orchard, *Journal of Power Sources*, **36**, 537 (1991).

59. G. G. Botte, V. R. Subramanian and R. E. White, *Electrochimica Acta*, **45**, 2595 (2000).

60. M. Doyle, T. Fuller and J. Newman, *Journal of the Electrochemical Society*, **140**, 1526 (1993).

61. V. J. Farozic and G. A. Prentice, *Journal of Applied Electrochemistry*, **21**, 767 (1991).

62. R. E. Garcia, Y. M. Chiang, W. C. Carter, P. Limthongkul and C. M. Bishop, *Journal of the Electrochemical Society*, **152** (2005).

63. K. Li, J. Wu, Y. Jiang, Z. Hassan, Q. Lv, L. Shang and D. Maksimovic, in *Proc. of ISLPED*, p. 277 (2010).

64. G. Ning and B. N. Popov, *Journal of the Electrochemical Society*, **151** (2004).

65. S. W. Orchard and J. S. Weaving, *Journal of Applied Electrochemistry*, **23**, 1214 (1993).

66. B. Paxton and J. Newman, *Journal of the Electrochemical Society*, **144**, 3818 (1997).

67. Y. Y. Wang, M. R. Lin and C. C. Wan, *Journal of Power Sources*, **13**, 65 (1984).

68. J. Newman and W. Tiedemann, *AIChE Journal*, **21**, 25 (1975).

69. R. Pollard and J. Newman, *Journal of the Electrochemical Society*, **126**, 1713 (1979).

CHAPTER 2

EXPERIMENTAL

2.1. Characterization of Watts Nickel Bath Containing SiC and PEI

All experiments were conducted on a platinum rotating disk electrode (RDE) with a diameter of 0.5 cm. Before each experiment, a thin layer of nickel was deposited on the RDE at a current density of -10 mA cm^{-2} for 30s. The cell used in the experiments was a 250 mL jacketed beaker. A nickel rod (99.5%) was used as the counter electrode. The reference electrode was a Ag/AgCl (3M NaCl) electrode. Watts solution (300 g L^{-1} $NiSO_4.6H_2O$, 35 g L^{-1} $NiCl_2.6H_2O$, 40 g L^{-1} H_3BO_3) was used as the plating bath. The pH of the solution was adjusted to 4.4 at room temperature using 1 M NaOH. The temperature was kept constant at 50 ^{0}C during experiments by the use of a circulating water bath. The experiments were conducted with 1 μm SiC particles (Alfa Aesar, beta-phase, 99.8%) at concentrations of 20 or 50 g L^{-1} in the plating bath [1-11].

In order to investigate the effect of PEI on the electrochemical kinetics, a Watts solution with 20 g L^{-1} SiC and two different molecular weights of polyethyleneimine, M_n 60000 (Acros Organics, 50 wt% aqueous soln, branched) and M_n 1200 (Sigma-Aldrich, 50 wt% soln in water) were characterized through linear sweep voltammetry and current efficiency experiments. PEI concentrations of 0-20 g L^{-1} were added to the Watts bath containing SiC particles. The solutions were stirred for 1 h followed by sonication for 12 min prior to each experiment. Linear sweep experiments were conducted between -0.6 V and -1.2 V with a sweep rate of -0.5 mV s^{-1}. The experiments were carried out with a rotation speed of 2500 rpm. Current efficiency was determined from stripping

experiments in 0.2 M HCl solution using Faraday's law by measuring the time to strip the nickel film at a current density of 50 mA cm^{-2} [12].

The zeta potentials of the SiC particles were measured using a Zeta-meter 3.0+ unit. The measurements were done at a pH of 4.4 in 0.01 M NaCl solution for PEI 1200 and PEI 60000 concentrations of 0 and 1000 ppm.

2.2. Co-deposition of Ni/SiC Micro-Composites

Table 2.1 summarizes the experimental parameters used in the co-deposition studies for micro-particles. The electrolyte was stirred for 1 h at 300 rpm and then sonicated for 12 min prior to plating since uniform deposits could not be obtained with less stirring. Before each experiment, a layer of Ni was deposited on the cathode by applying -10 mA cm^{-2} for 30 s. The films were sonicated for 5 min in distilled water after each plating experiment to eliminate any loosely incorporated SiC particles. The composites were characterized by scanning electron microscopy (SEM) with an energy-dispersive X-ray spectroscopy (EDX) system in order to measure the weight percentage of the ceramic particles in the deposits. The measurements were done at 5 different points on the same deposit to get an average SiC wt%.

The effect of preparation of the plating solution was also investigated in the presence of PEI 60000. The plating solution was prepared by the addition of 200 ppm PEI 60000 to a Watts solution containing 50 g L^{-1} SiC and stirred for 1 h and sonicated for 12 min as described above. To test the ability of making solutions in advance, the prepared solution was shelved for a day. On the second day, the plating experiment was conducted after 15 min of stirring. The incorporated SiC amount of this experiment was

11.9 vol% (and was 11.6 vol% from a fresh electrolyte). This result suggests that the solution can be prepared in advance, possibly an important consideration in a manufacturing environment.

Table 2.1. Experimental parameters in Ni/SiC co-deposition studies.

Electrolyte Composition (Watts bath)	
$NiSO_4.6H_2O$	300 g L^{-1}
$NiCl_2.6H_2O$	35 g L^{-1}
H_3BO_3	40 g L^{-1}
SiC powder (1 μm)	20, 50 g L^{-1}
Electrodeposition Conditions	
pH	4.4
Temperature	50 ^{0}C
Substrate	Brass disc (diameter 1 cm)
Anode	Nickel rod (99.5%)
RDE rotation rate	100, 400, 900 rpm
Magnetic stirring rate	200 rpm
Current density	10, 25, 50, 100 mA cm^{-2} (DC)
Duration of plating	50, 20, 10, 5 min
PEI concentration	0, 10, 50, 75, 100, 200, 1000 ppm

In some experiments, the SiC particles were pre-coated with PEI 60000 or PEI 1200 prior to introduction into the plating bath. Here, 20 g L^{-1} SiC was stirred for 1 h and sonicated for 12 min in the presence of 1000 ppm PEI in a Watts bath or 0.1 M Na_2SO_4 solution at room temperature. After the SiC particles are pre-coated with PEI, the solution was centrifuged and the supernatant was removed. Then, fresh Watts solution was added to the PEI-coated SiC particles, pre-coated in Watts bath (W-PEI-coated SiC) or in 0.1 M Na_2SO_4 bath (SS-PEI-coated SiC), to make a 20 or 50 g L^{-1} SiC solution. The solution was then stirred again for 1 h and sonicated 12 min at 50 ^{0}C prior to the plating experiments. Figure 2.1 describes the procedure for this particle-preparation method.

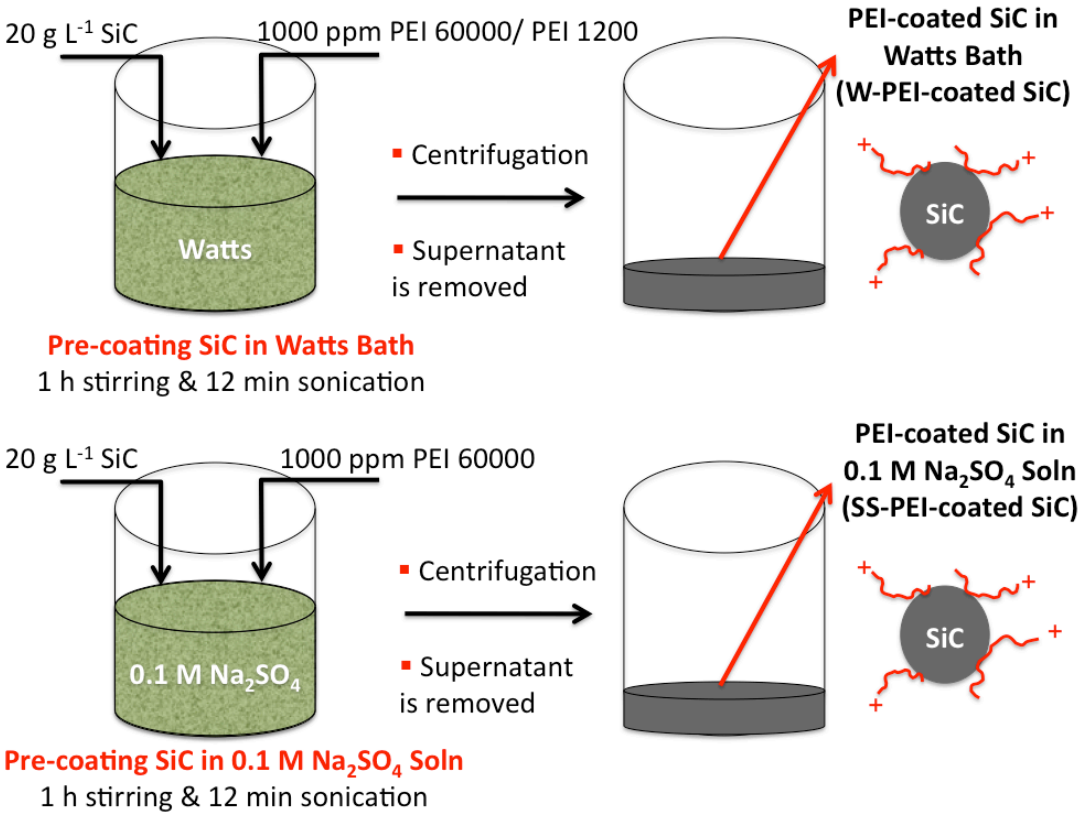

Figure 2.1. Experimental procedure of pre-coating SiC micro-particles with PEI.

In order to test the suitability of pre-coated particles in a manufacturing environment where the electroplating process is not used continuously and caking of the particles would render their use unacceptable, a plating bath containing 50 g L^{-1} W-PEI-coated micro SiC particles was stored for a week. On the second and seventh day, plating and CE measurements were conducted after just 15 min stirring at 300 rpm.

In some of the experiments, coumarin, which is a commonly used leveler in Ni plating, was used in the plating bath [13]. In the first series of studies, 100 ppm of coumarin was added to the plating solution at the same time with 200 ppm PEI and 50 g L^{-1} SiC micro-particles. In the second set, 100 ppm coumarin was added to the plating bath containing pre-coated SiC micro-particles (50 g L^{-1} SS-PEI-coated SiC). The effect of coumarin on SiC incorporation was investigated and compared for the two cases.

2.3. Co-deposition of Ni/SiC Nano-Composites

All plating experiments were performed on a brass rotating disk electrode (RDE) with a diameter of 1 cm. A thin layer of Ni (≈10 nm) was deposited on the brass RDE before each experiment by applying -10 mA cm^{-2} for 30 s. A nickel rod (99.5%) and Ag/AgCl (3 M NaCl) electrode were used as the counter and reference electrodes, respectively. A Watts solution (300 g L^{-1} $NiSO_4.6H_2O$, 35 g L^{-1} $NiCl_2.6H_2O$, 40 g L^{-1} H_3BO_3) was used as the plating bath. The pH of the Watts bath was adjusted to 4.4 at room temperature using 1 M NaOH. The solution temperature was kept constant at 50 ^{0}C during electroplating using a circulating water bath. The experiments were conducted with 45-55 nm SiC particles (Alfa Aesar, beta-phase). Polyethyleneimine of 60000 molecular weight (Acros Organics, 50 wt% aqueous solution, branched) was used as a

dispersant. All plating experiments were conducted at a current density of -50 mA cm^{-2}, a rotation speed of 100 rpm and a magnetic stirring speed of 200 rpm. The thickness of the films was around 10 μm.

Nano-particles were washed with ethanol before each experiment, since the highly hydrophobic surfaces of these particles otherwise caused them to float on the surface of the bath. The effect of PEI on nano-particle incorporation was investigated for two different cases. In the first scenario, PEI was added directly to the plating bath with the nano-particles. The plating was conducted after stirring the electrolyte for 1 h at 500 rpm, followed by sonicating for 30 minutes. In the second approach, nano-particles were pre-coated with PEI prior to plating. The pre-coating procedure that was described for the micro-particles in the previous section was modified for nano-particles. Here, 20 g L^{-1} SiC and 500 ppm PEI were stirred for 1 h at 500 rpm and sonicated for 30 min in either 0.1 or 0.5 M Na_2SO_4 solution or in ethanol at room temperature. After the nano-particles were pre-coated with PEI, the solution was centrifuged and the supernatant was removed. The pre-coated particles (0.1SS-PEI-coated SiC, 0.5SS-PEI-coated SiC and EtOH-PEI-coated SiC) were then added to a fresh Watts solution to make a 50 g L^{-1} SiC solution. The solution was then again stirred for 1 h at 500 rpm and sonicated for 30 min prior to plating. Figure 2.2 is a schematic diagram outlining the pre-coating procedure for the nano-particles.

The SiC fraction in the deposit was measured using energy-dispersive X-ray spectroscopy (EDX) connected to a Hitachi 4700 scanning electron microscope (SEM). The SiC fractions were measured at 5 different points on the same deposit to get an average value. Si mapping of the composite films were also done using the EDX. The

surface roughness of the deposits was measured using an Alpha-Step IQ surface profilometer. To calculate the average roughness R_a, surface roughness measurements were conducted at 3 different points on the same deposit with a scan speed of 20 μm s^{-1} over a scan length of 2 mm. The Vickers hardness of the films was measured using a Leco LM 100 microhardness tester with a load of 25 gf. The average of 10 measurements was taken for the same deposit.

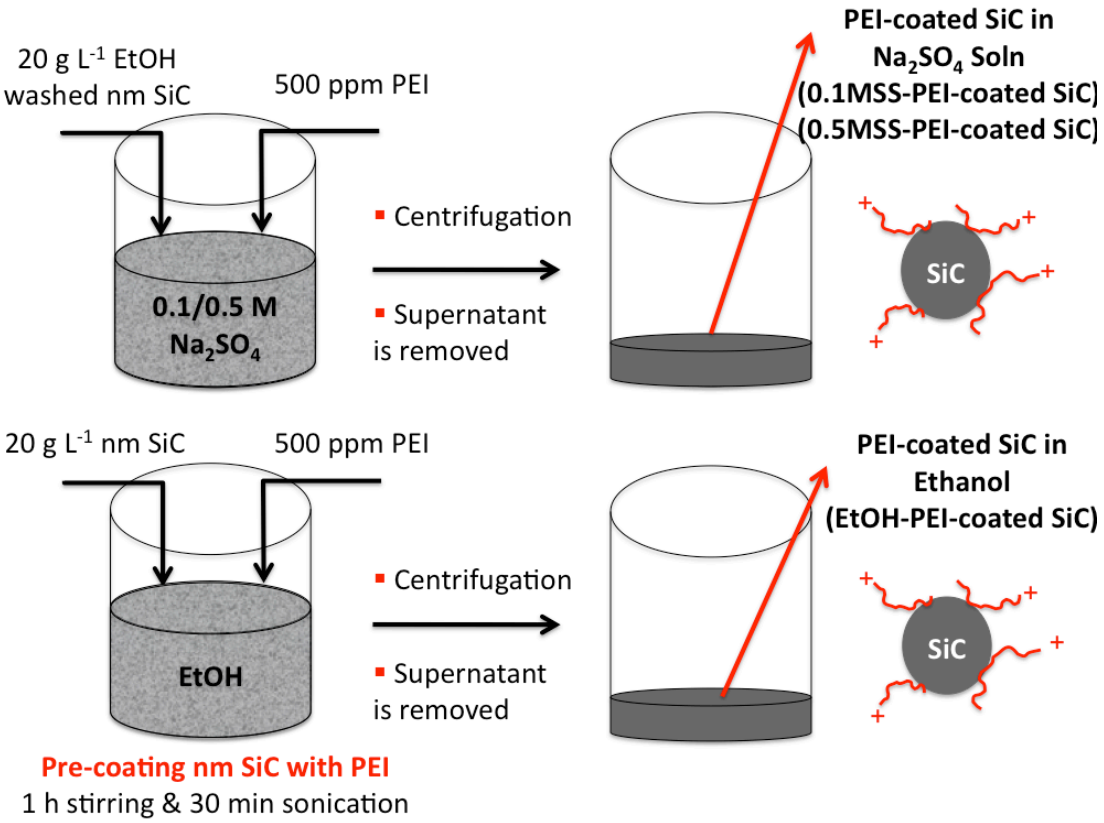

Figure 2.2. Experimental procedure of pre-coating SiC nano-particles with PEI.

2.4. References

1. L. Benea, P. L. Bonora, A. Borello, S. Martelli, F. Wenger, P. Ponthiaux and J. Galland, *Journal of the Electrochemical Society*, **148**, C461 (2001).

2. I. Garcia, J. Fransaer and J. P. Celis, *Surface and Coatings Technology*, **148**, 171 (2001).

3. E. Garcia-Lecina, I. Garcia-Urrutia, J. A. Diez, M. Salvo, F. Smeacetto, G. Gautier, R. Seddon and R. Martin, *Electrochimica Acta*, **54**, 2556 (2009).

4. M. D. Ger, *Materials Chemistry and Physics*, **87**, 67 (2004).

5. K. H. Hou, M. D. Ger, L. M. Wang and S. T. Ke, *Wear*, **253**, 994 (2002).

6. S. K. Kim and H. J. Yoo, *Surface and Coatings Technology*, **108-109**, 564 (1998).

7. G. Maurin and A. Lavanant, *Journal of Applied Electrochemistry*, **25**, 1113 (1995).

8. P. Nowak, R. P. Socha, M. Kaisheva, J. Fransaer, J. P. Celis and Z. Stoinov, *Journal of Applied Electrochemistry*, **30**, 429 (2000).

9. E. A. Pavlatou, M. Stroumbouli, P. Gyftou and N. Spyrellis, *Journal of Applied Electrochemistry*, **36**, 385 (2006).

10. N. K. Shrestha, I. Miwa and T. Saji, *Journal of the Electrochemical Society*, **148**, C106 (2001).

11. M. Srivastava, V. K. William Grips and K. S. Rajam, *Materials Letters*, **62**, 3487 (2008).

12. I. Shao, P. M. Vereecken, C. L. Chien, P. C. Searson and R. C. Cammarata, *Journal of Materials Research*, **17**, 1412 (2002).

13. C. C. Cheng and A. C. West, *Journal of the Electrochemical Society*, **144**, 3050 (1997).

CHAPTER 3*

ELECTRODEPOSITION OF Ni/SiC MICRO-COMPOSITES IN THE PRESENCE OF POLYETHYLENEIMINE

In the first part of this dissertation, Ni/SiC co-deposition, a complex electrochemical system that caries significant importance for industry, is explored. The enhanced mechanical and tribological properties of Ni/SiC composites depend to a great extent on the amount and uniformity of the ceramic particles in the deposit. High and uniform SiC incorporation is a strong function of the stability of the particles in the plating solution. A major challenge in these studies is that the dispersants that are used to stabilize the suspensions can affect the electrodeposition significantly. In this chapter, the effect of PEI on the co-deposition of 1 μm SiC particles with Ni is discussed as a function of SiC and PEI bath concentrations, molecular weight of PEI, current density and rotation speed. Finally, a pre-coating procedure for SiC particles with PEI is described [1].

3.1. Results and Discussion

3.1.1. Effect of PEI 60000

The polarization curves for a Watts bath containing 20 g L^{-1} SiC and varying PEI 60000 concentrations are shown in Figure 3.1. From the figure, it can be seen that the addition of the polymer at low concentrations does not create any significant inhibition of

* D. Eroglu, A. Vilinska, P. Somasundaran and A. C. West, *Journal of the Electrochemical Society*, **160**, D35 (2013).

nickel deposition except at small overpotentials. In contrast, when the polymer is added at concentrations of 1000 ppm or more, there is a significant shift in the potentials presumably due to adsorption of the polymer onto the electrode, effectively reducing the number of available sites where charge transfer can occur. Above this concentration of PEI, the inhibition saturates and remains nearly the same for all PEI concentrations. This suppression of PEI on nickel deposition rate has also been explained in the literature by an ion-pairing interaction between the cathode and the polymer that blocks the electrode surface [2]. Another reason of this inhibition may be the interaction between charged imine groups on PEI and the nickel ions [3].

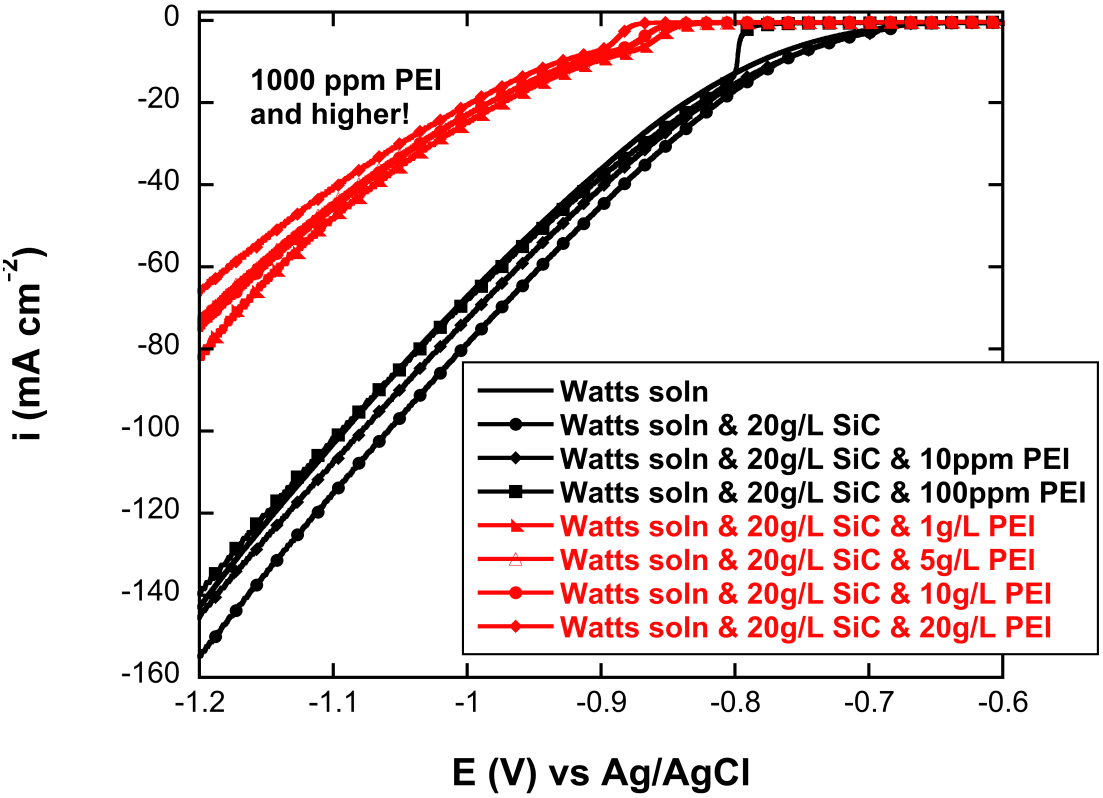

Figure 3.1. Polarization curves for a Watts solution containing 20 g L^{-1} SiC and different PEI 60000 concentrations. In all cases the disk rotation speed was 2500 rpm.

In order to further quantify the inhibition of PEI on nickel deposition, current efficiencies at different current densities were measured, and results are shown in Figure 3.2. It can be observed that for both current densities, for concentrations higher than 200 ppm current efficiency decreases significantly, with the majority of the current resulting in hydrogen evolution instead of nickel deposition. These low current efficiencies are unlikely to result in optimal films especially when implemented on parts with complex geometries, and therefore the polymer should only be added into the plating solution up to 200 ppm without affecting the electrodeposition in a negative manner.

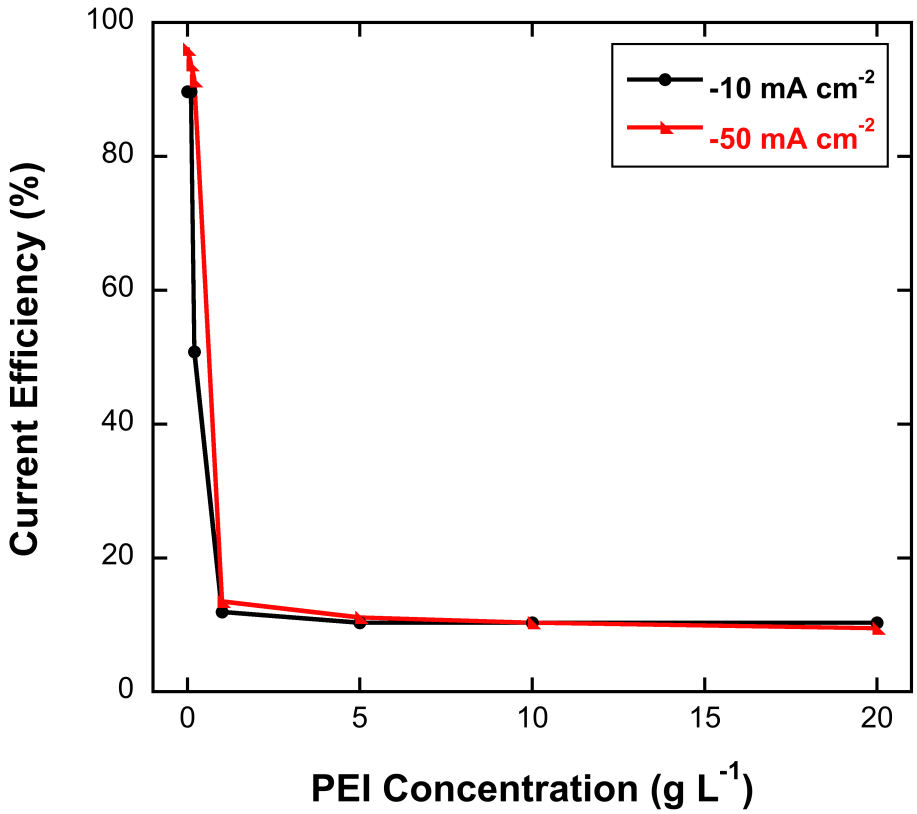

Figure 3.2. Current efficiency as a function of PEI 60000 concentration in a Watts bath containing 20 g L^{-1} SiC for different current densities (Ω = 400 rpm).

Figure 3.3 shows the effect of PEI 60000 concentration in the plating bath on the SiC incorporation for two SiC bath concentrations. Experiments were conducted at a PEI concentration range from 0-200 ppm where the current efficiency remains high. The trends are the same for both SiC bath concentrations: a slight decrease at low concentrations followed by a significant increase at PEI concentrations of 100 and 200 ppm. This increase in the SiC fraction in the deposit at these concentrations may result from an affinity of the SiC particles to the cathode when PEI is adsorbed on the particle surface.

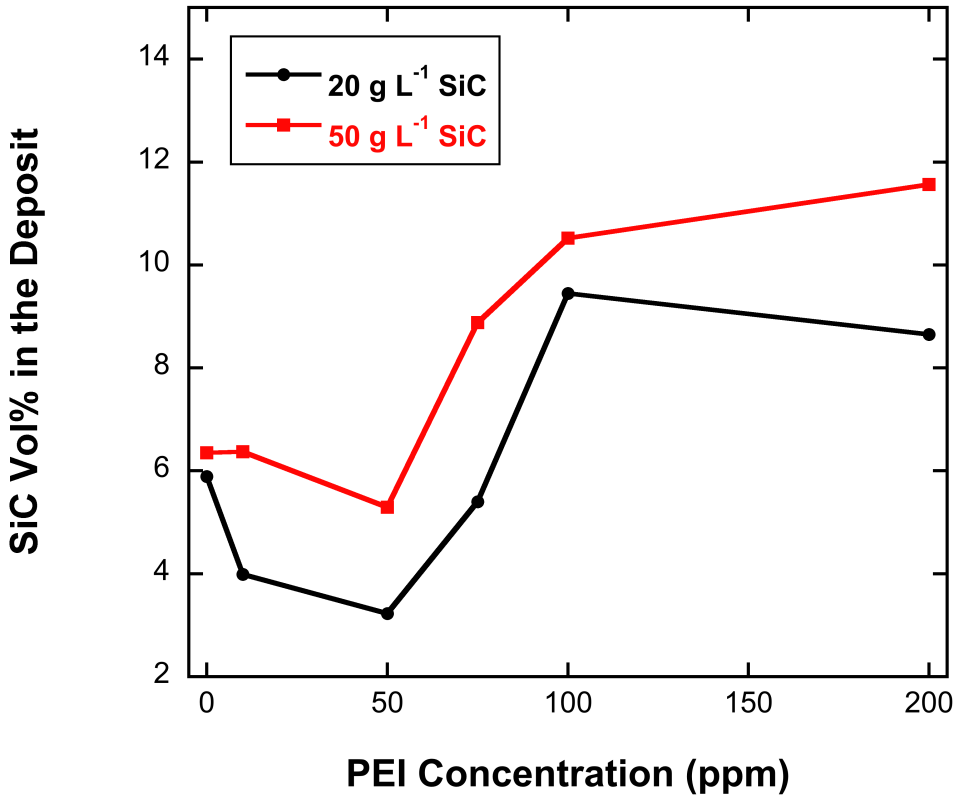

Figure 3.3. SiC fraction in the deposit as a function of PEI 60000 concentration for different SiC bath concentrations at a current density of -50 mA cm^{-2} and rotation speed of 100 rpm.

Increasing the SiC concentration in the plating bath from 20 to 50 g L^{-1} increases the SiC fraction in the deposit, however this increase it not very significant. Previous studies have also shown that SiC fraction in the deposit saturates after a certain SiC bath concentration [4, 5]. Most probably saturation has been reached for these conditions.

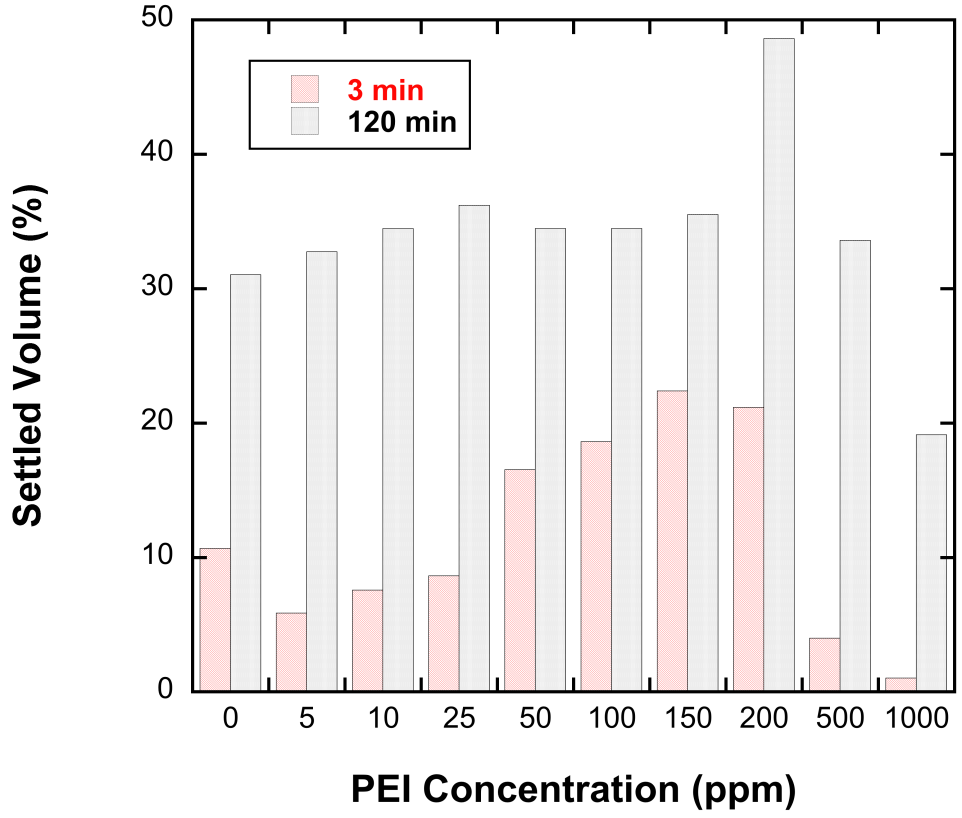

Figure 3.4. The effect of PEI 60000 concentration on the dispersion of SiC particles in the Watts bath containing 20 g L^{-1} SiC after 3 and 120 min.

The effect of PEI 60000 on the dispersion of SiC particles in the plating bath can be seen in Figure 3.4 for different PEI concentrations. The percentage of SiC particles in the suspension that is settled after 3 and 120 min after the solution is prepared was measured. For the 3-min results, there is a slight improvement in dispersion for very low

PEI concentrations (5-25 ppm). However after 50 ppm, the polymer adversely affects dispersion. Increasing the PEI concentration further dramatically improves dispersion, and the best result is obtained for PEI concentration of 1000 ppm. The effect of PEI on dispersion after 120 min is negligible for low concentrations, however addition of 1000 ppm PEI 60000 still contributes to the stability of SiC particles in the plating solution. Therefore it can be concluded that significant improvement in dispersion can only be obtained at high PEI 60000 concentrations such as 1000 ppm. When Figures 3.3 and 3.4 are compared, it can be seen that for the PEI concentrations of 100 and 200 ppm where SiC fraction in the deposit is high, dispersion of SiC particles is at a minimum. This indicates that the increase in SiC fraction is not due to the increased stability of the suspension, and can be contrasted with previous studies. Since the suspensions were stirred by a magnetic stirrer from the bottom of the beaker in addition to the rotation of the disk, the effect of the stability of particles on the incorporation may not be seen directly.

The effect of rotation speed for a Watts bath can be seen in Figure 3.5. A significant increase in SiC vol% is seen with increasing rotation speed for a Watts bath without PEI. However when PEI is present, the resulting SiC fraction in the deposit is not a strong function of rotation speed. It is also apparent from the figure that addition of 200 ppm PEI 60000 results in an increase in SiC vol% for all rotation speeds.

SiC incorporation as a function of current density is shown in Figure 3.6 for a Watts solution. It can be seen that there are two different regimes. At current densities up to 50 mA cm^{-2}, the change in current density does not significantly affect the SiC fraction, implying that SiC incorporation rate is proportional to current density. However,

as the current density is further increased, the SiC fraction in the deposit decreases. Most probably in this second regime, the nickel deposition rate increases more than the rate of SiC incorporation, causing its volume percentage to decrease.

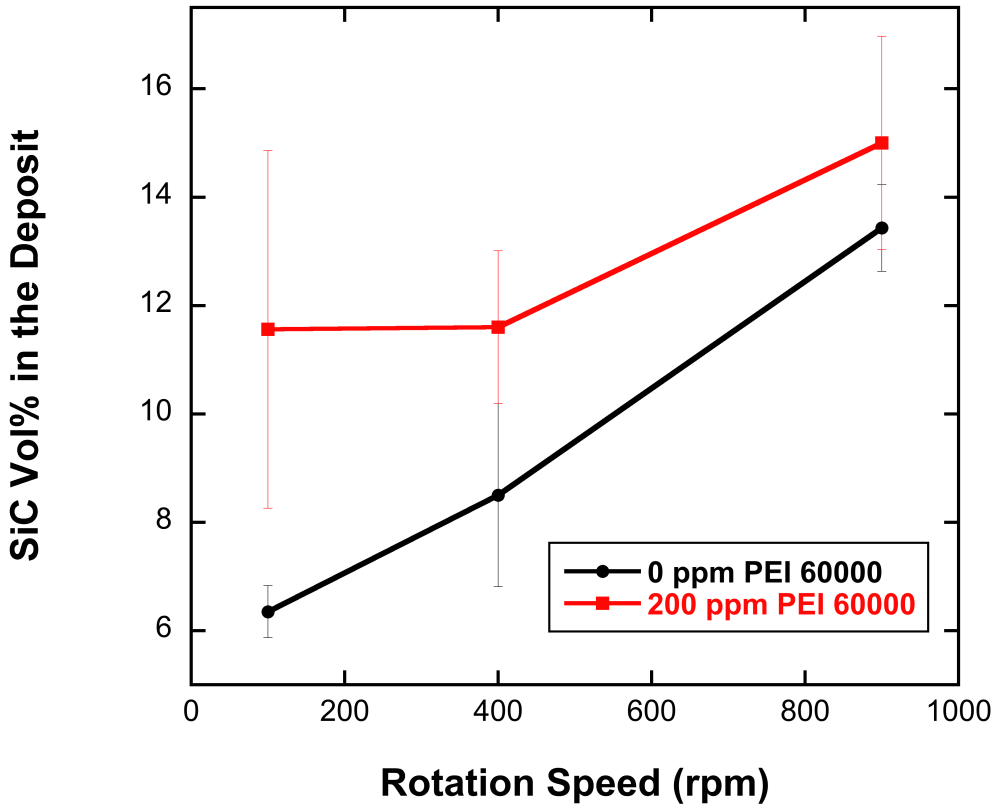

Figure 3.5. SiC fraction in the deposit as a function of rotation speed for a Watts bath containing 50 g L^{-1} SiC at a current density of -50 mA cm^{-2}.

It can also be seen from the figure that the systems containing 200 ppm PEI show higher SiC loadings for all current densities. Therefore, it can be concluded that PEI 60000 at a concentration of 200 ppm increases incorporated SiC volume fraction, apparently independent of other system variables.

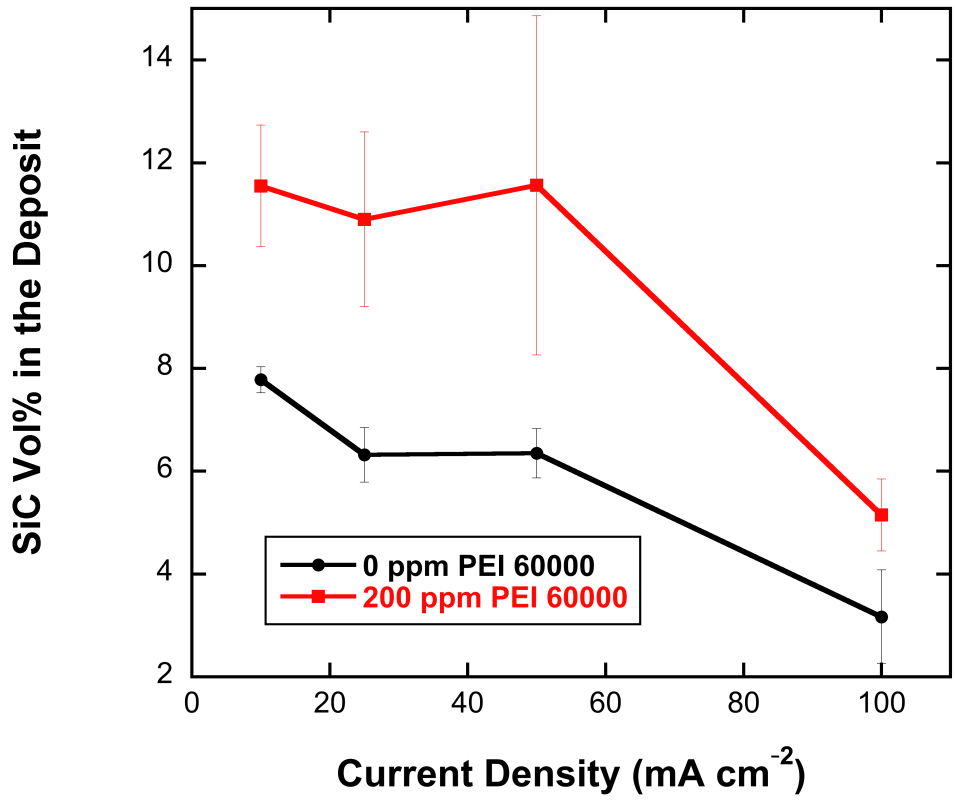

Figure 3.6. SiC fraction in the deposit as a function of current density for a Watts bath containing 50 g L^{-1} SiC at a rotation speed of 100 rpm.

In order to further explore the effect of these system variables on the SiC incorporation rate, the study of Vereecken *et al.* [6] who analyzed the rate of alumina-particle incorporation into Ni by plotting $N_P/\Omega^{1/2}$ (N_P is the particle flux to the surface in mol cm^{-2} s^{-1} and Ω is the rotation speed of RDE in rad s^{-1}) as a function of current density is analyzed. This method allows one to infer whether the incorporation rate is governed by mass transfer of particles to the surface. N_P was calculated for volume fraction data assuming that the ceramic particle fraction in the deposit is proportional to the ratio of particle flux to the total flux of particles and metal ions to the surface.

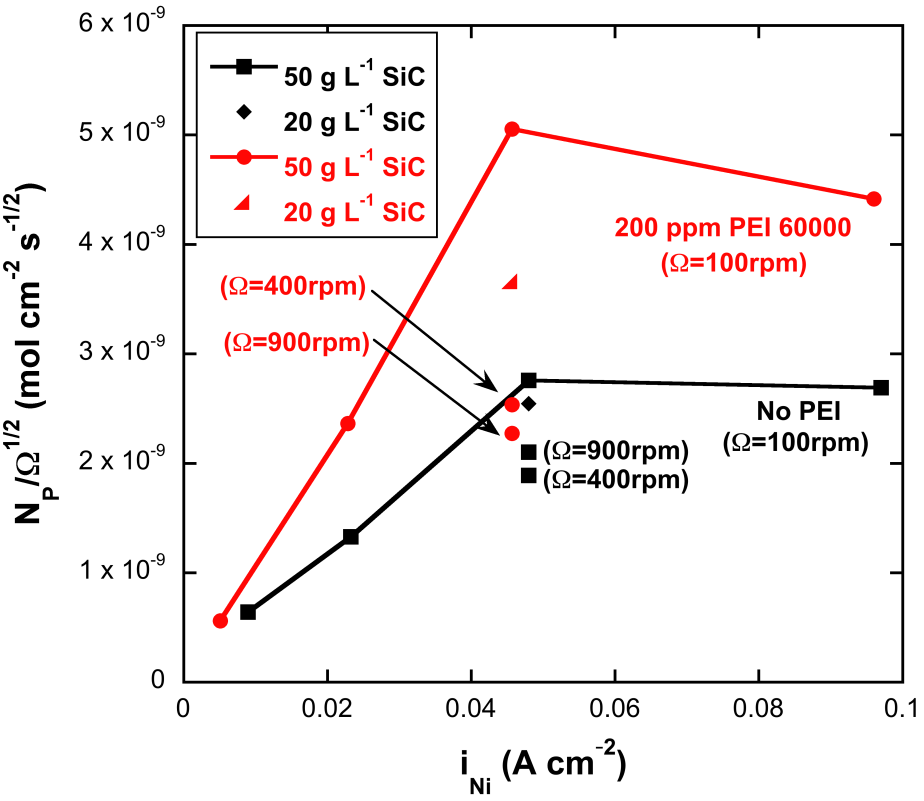

Figure 3.7. The particle flux divided by the square root of rotation speed as a function of current density. $N_P/\Omega^{1/2}$ was calculated from experimental data. Current densities are corrected according to current efficiencies.

Figure 3.7 shows that the measured $N_P/\Omega^{1/2}$ increases with increasing current density until a saturation value is reached. After this point, the rate of particle incorporation is independent of current density. This plateau in the figure corresponding to the maximum value of $N_P/\Omega^{1/2}$ (and may indicate a mass-transfer limitation) can be used to estimate the diffusion coefficient of the particles in the electrolyte. It can be seen that for the data with no PEI, the plateau is reached at a current density of 50 mA cm^{-2}. The diffusion coefficient for the particles predicted by the model is 1.8 x 10^{-9} cm^2 s^{-1}, which is around 5 times smaller than the diffusion coefficient calculated by the Stokes-

Einstein equation. This suggests that a mass transfer limitation may not be the cause of the plateau. When the data with PEI 60000 is used, the effective diffusion coefficient is 4.5 x 10^{-9} cm^2 s^{-1}, in relatively close agreement with the Stokes-Einstein prediction. However, increasing the particle bath concentration from 20 to 50 g L^{-1} does not result in a 2.5 times increase in $N_P/\Omega^{1/2}$. This suggests that also for this case the incorporation plateau is not mass transfer controlled. The data shown in the figure for different rotation speeds at 50 mA cm^{-2} also do not follow the curves. All these suggest that mass transfer limitations are not dominant. A model that takes into account the adsorption of the particles on the electrode [5] will probably be more successful in explaining the co-deposition mechanism.

3.1.2. Effect of Molecular Weight of PEI

Figure 3.8 shows the effect of concentration for two molecular weights of PEI on the measured current efficiency. The lower molecular weight PEI inhibits deposition much more significantly at lower concentrations. For example, PEI 1200 suppresses nickel deposition even at 50 ppm.

Given the large suppression caused by PEI 1200, it was maintained at a low concentration (100 ppm) in the plating studies. Experiments were conducted at -50 mA cm^{-2} and 100 rpm. The lower MW PEI results in SiC amount of 16.6 vol%, which is significantly higher for the same concentration of PEI 60000 (9.45 vol% SiC in the deposit). However it should be kept in mind that, even at 100 ppm, the current efficiency of PEI 1200 is much lower than PEI 60000. In addition to the molecular weight difference there is a difference in the structures of the two polymers: PEI 60000 is

branched whereas PEI 1200 is linear. Therefore there could be a difference in the amount of charge on SiC particles as a result of adsorption of the polymers.

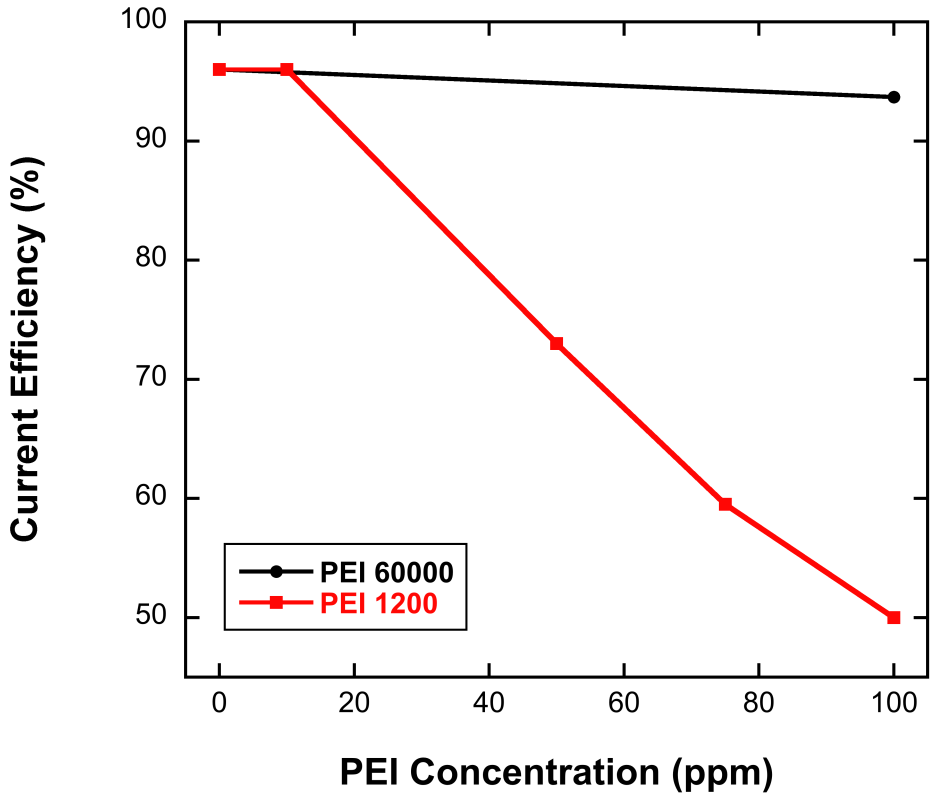

Figure 3.8. The effect of concentration of PEI on the current efficiencies for different molecular weight PEI in a Watts bath containing 20 g L^{-1} SiC at a current density of -50 mA cm^{-2} (Ω = 400 rpm).

The effect of PEI 1200 on the SiC particle stability in the plating bath can be seen in Figure 3.9. The percentage of SiC particles that is settled after 3 min is compared for the two molecular weight polymers in the figure. It can be seen that addition of PEI 1200 does not result in a significant change in dispersion even at very high concentrations. The stability of the suspension even after 1000 ppm PEI 1200 is not sufficient.

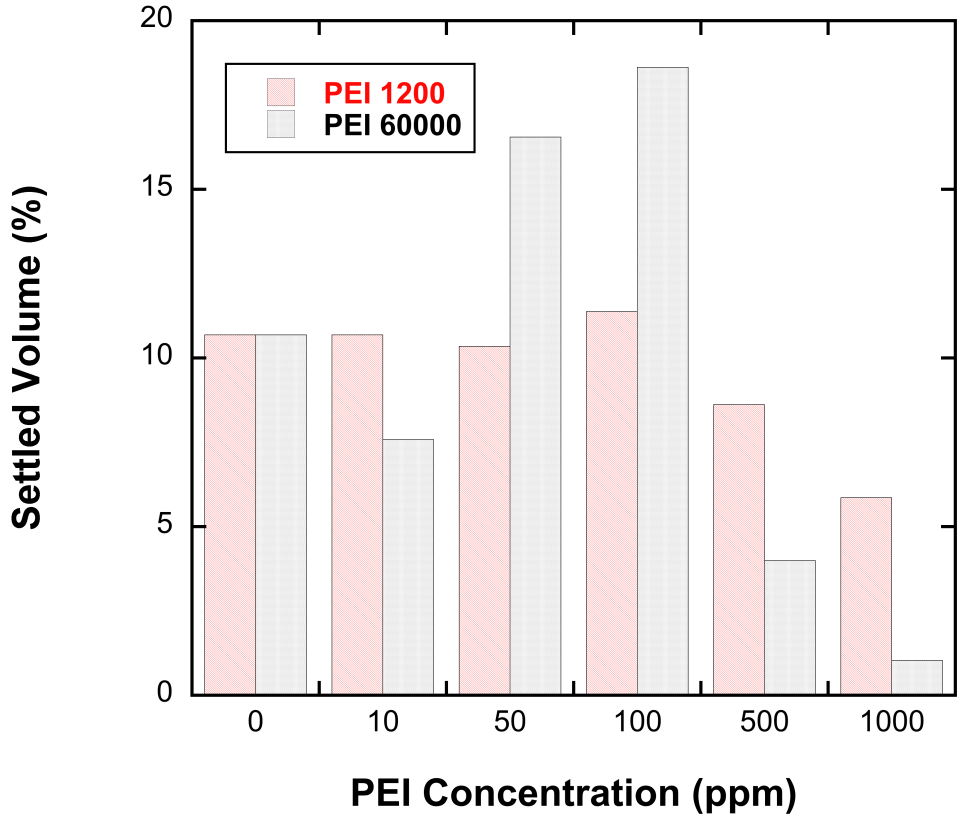

Figure 3.9. The effect of PEI 1200 concentration on the dispersion of SiC particles in the Watts bath containing 20 g L^{-1} SiC after 3 min.

In order to quantify the dispersion characteristics of the two polymers, their zeta potentials are measured and reported in Table 3.1. The zeta potentials are measured in 0.01 M NaCl solution (pH=4.4) instead of Watts solution since at very high ionic strengths, the electrical double layer on the particle surface collapses resulting in very low zeta potentials making the measurements very hard [7]. Therefore, in order to be able to observe the trend of how zeta potential changes with PEI concentration, a lower ionic strength solution is used. The zeta potentials of the particles get more positive with the adsorption of the cationic PEI as expected. It can also be seen that the addition of PEI 60000 results in a higher zeta potential supporting the higher stability of the suspension

with this polymer. The increase in the zeta potential of the particles with the addition of PEI may also be a reason of the increased SiC fraction in the deposit.

Table 3.1. Zeta potentials of SiC particles in 0.01 M NaCl solution at a pH of 4.4.

	Zeta Potential (mV)
0 ppm	6.4
1000 ppm PEI 1200	29.4
1000 ppm PEI 60000	60.7

3.1.3. Effect of Pre-Coating SiC Particles with PEI 60000 Prior to Plating

In the previous sections, PEI 60000 concentration is always kept at 200 ppm or lower to prevent a large shift in overpotential that leads to excess H_2 evolution. However, the dispersion of SiC particles in the Watts bath is the best for the system containing 20 g L^{-1} SiC and 1000 ppm PEI 60000. The importance of dispersion on co-deposition may not be that significant in a beaker in laboratory, however in manufacturing of large complex parts, dispersion may be crucial to obtain uniform and high SiC loadings.

In order to gain the advantage of dispersion without decreasing the current efficiency, a novel means of preparing the particles was designed. In the pre-coating procedure described here, 20 g L^{-1} SiC particles are stirred with 1000 ppm PEI 60000 or PEI 1200 for 1 h and sonicated for 12 min in either a Watts bath or 0.1 M Na_2SO_4 solution. Various other pre-coating recipes were considered as documented in reference 9, but these electrolytes were the most successful. The solution is then centrifuged and

the supernatant containing the excess PEI is removed. Fresh Watts solution is added to the PEI-coated SiC particles to make a 20 or 50 g L^{-1} SiC solution. The fresh Watts solution containing the PEI-coated particles are then stirred for 1 h and sonicated 12 min prior to plating. The details of this procedure are described in Chapter 2.2.

Dispersion studies show that PEI60000-coated SiC particles are still highly dispersed in a Watts bath after the pre-coating procedure. Zeta potential of SS-PEI60000-coated SiC particles is measured to be 45.3 mV in 0.01M NaCl solution at a pH of 4.4. This result shows that SiC particles are still highly positively charged after the pre-coating procedure.

The effect of pre-coated SiC on the polarization curves can be seen in Figure 3.10. When the two polarization curves for the samples containing PEI-coated SiC particles are compared with the additive-free Watts solution in the figure, it can be seen that except at very low current densities, the shift in potentials obtained under normal bath formulations (Figure 3.1) can be eliminated by the pre-coating procedure.

The current efficiency results also support this conclusion. Current efficiency of 13.5% that is measured for the plating solution containing 20 g L^{-1} SiC and 1000 ppm PEI 60000, is 93.7% when pre-coated SiC particles (W-PEI60000-coated SiC) are used. The pre-coating procedure with PEI 1200 also results in high efficiencies as 92.1%. The addition of 200 ppm PEI 60000 to the plating bath after particle preparation decreases the current efficiency to 47.6%, however this decrease may still be in the acceptable range [8]. The current efficiencies of the samples that contain 50 g L^{-1} PEI-coated SiC in the plating bath are also similar to these results.

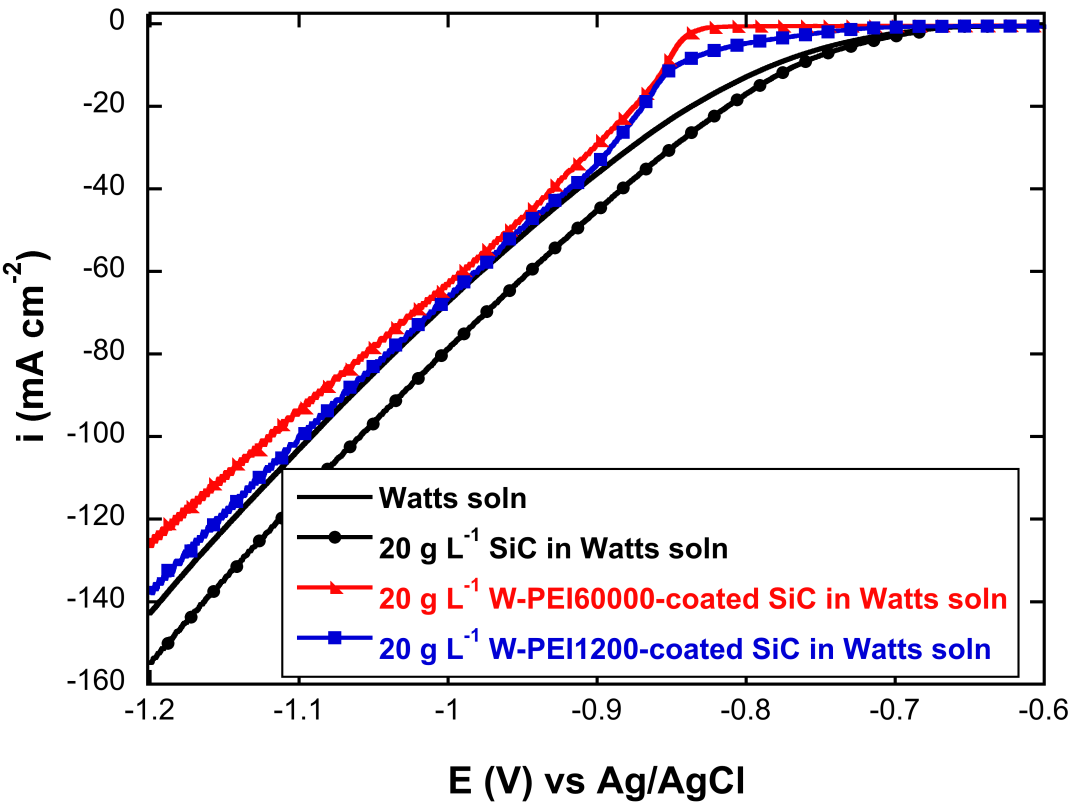

Figure 3.10. The effect of pre-coating SiC particles with PEI on the polarization curves for a Watts bath containing 20 g L^{-1} SiC (Ω=2500 rpm).

The fraction of SiC in the deposit for the plating solutions containing 50 g L^{-1} PEI-coated SiC is shown in Figure 3.11. It can be observed that all samples have high SiC loadings. When the results for PEI 60000 and PEI 1200 are compared in Column 1 in Figure 3.11, it can be seen that the resulting SiC fractions in the deposit are nearly the same. The polarization curves and current efficiency results also show no difference as mentioned above. However as discussed in the previous section, the dispersion with the lower MW polymer is much worse than PEI 60000. Therefore, PEI 60000 may be beneficial when attempting to implement on a larger scale, where intense mixing may not be feasible.

Another significant result is that the addition of PEI 60000 to the plating solution after pre-coating does not result in an increase in the SiC fractions. Therefore, the best results are obtained for solutions containing 50 g L^{-1} W-PEI60000-coated or SS-PEI60000-coated SiC without any additional PEI (Columns 1 and 3 in Figure 3.11). These systems have high current efficiencies and SiC loadings higher than 13% in addition to high ceramic particle stability in the plating solution.

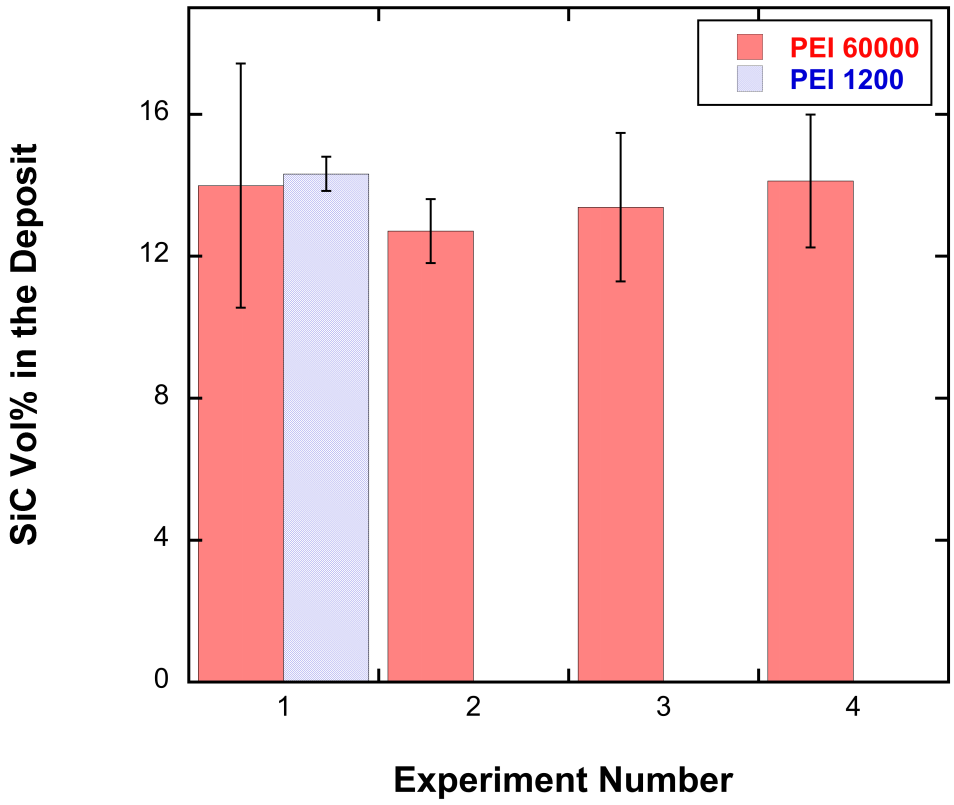

Figure 3.11. SiC fraction in the deposit for different pre-coating and plating conditions. Plating conditions - Experiment 1: 50 g L^{-1} W-PEI-coated SiC in Watts bath, Experiment 2: 50 g L^{-1} W-PEI-coated SiC and 200 ppm PEI 60000 in Watts bath, Experiment 3: 50 g L^{-1} SS-PEI-coated SiC in Watts bath, Experiment 4: 50 g L^{-1} SS-PEI-coated SiC and 200 ppm PEI 60000 in Watts bath.

3.1.4. Long Term Bath Efficacy

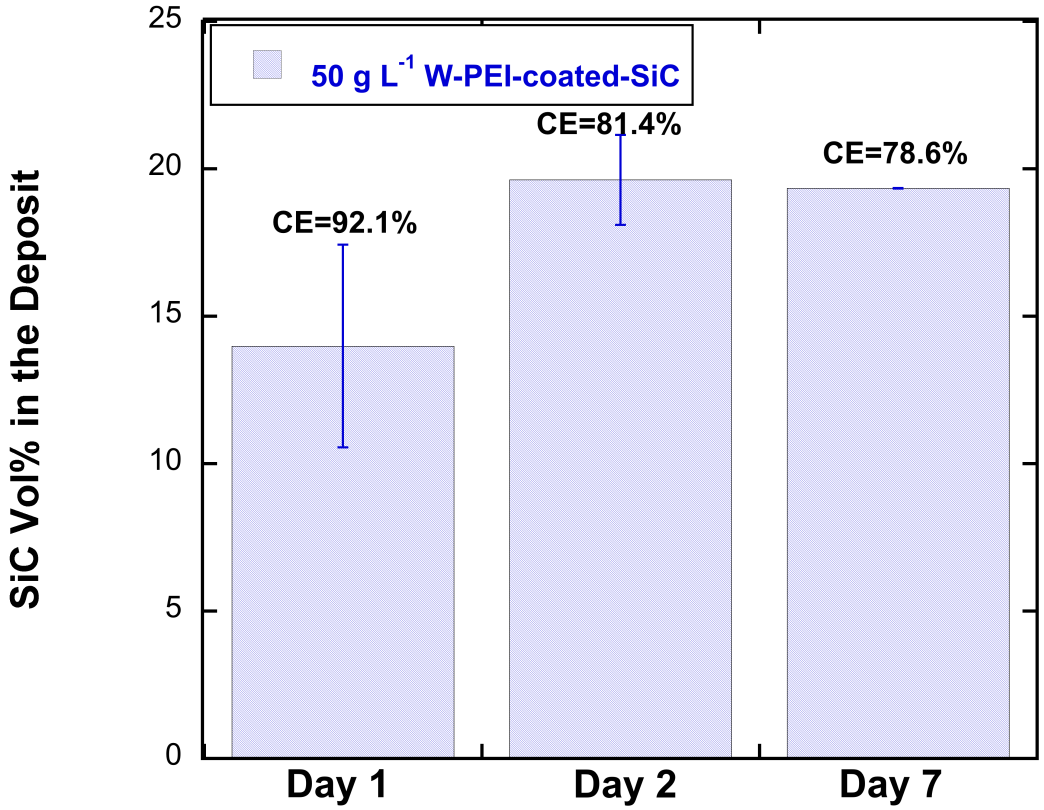

Figure 3.12. The effect of aging is shown through results obtained on 1st, 2nd and 7th day the particle-laden electrolyte is prepared. All micro-particles were pre-coated in Watts bath.

The pre-coating process is effective in part if the PEI does not desorb from the SiC after immersion into the Watts bath. It is possible that desorption times are much longer than in a typical lab experiment, where the pre-coated SiC is added on the same day. Thus, the long-term efficacy of this approach requires studies on longer time scales. In addition, settling of the particles in an unstirred electrolyte may result in caking, severely limiting the utility of the approach. In order to evaluate these possible issues, a

plating bath prepared with 50 g L^{-1} W-PEI-coated micro-particles was stored for a week. On the second and seventh day, the plating and current efficiency measurements were performed after 15 min of stirring. The results can be seen in Figure 3.12. It is apparent from the figure that the SiC incorporation rate is not affected; SiC vol% is still very high after a week. The current efficiency decreases to 81% on the second day, however there is no further decrease seen with increasing time. It is speculated that the shorter polymer chains desorb, increasing the free PEI concentration in the plating bath in a short period of time. It can be concluded that the pre-coating procedure is still effective after a week, since SiC incorporation rate is not reduced and the decrease in the current efficiency is not significant.

3.1.5. Effect of a Leveling Agent in the Presence of PEI

Figure 3.13 shows the effect of coumarin on the SiC vol% in the deposit for two different cases. When coumarin is added into the plating bath at the same time as the PEI, the SiC incorporation decreases significantly. However when coumarin is added with the pre-coated SiC particles, there is no change in the SiC fraction. This may suggest that when coumarin and PEI are introduced to the particles at the same time, coumarin is more quickly adsorbed on the SiC surface, hindering the adsorption of PEI. Therefore the effect of the cationic dispersant is not realized. However when pre-coated particles are used in the solution, the SiC surface is already covered with PEI, therefore the incorporation rate is not affected. This result has importance in providing a framework on the use of pre-coated particles in the presence of other plating additives.

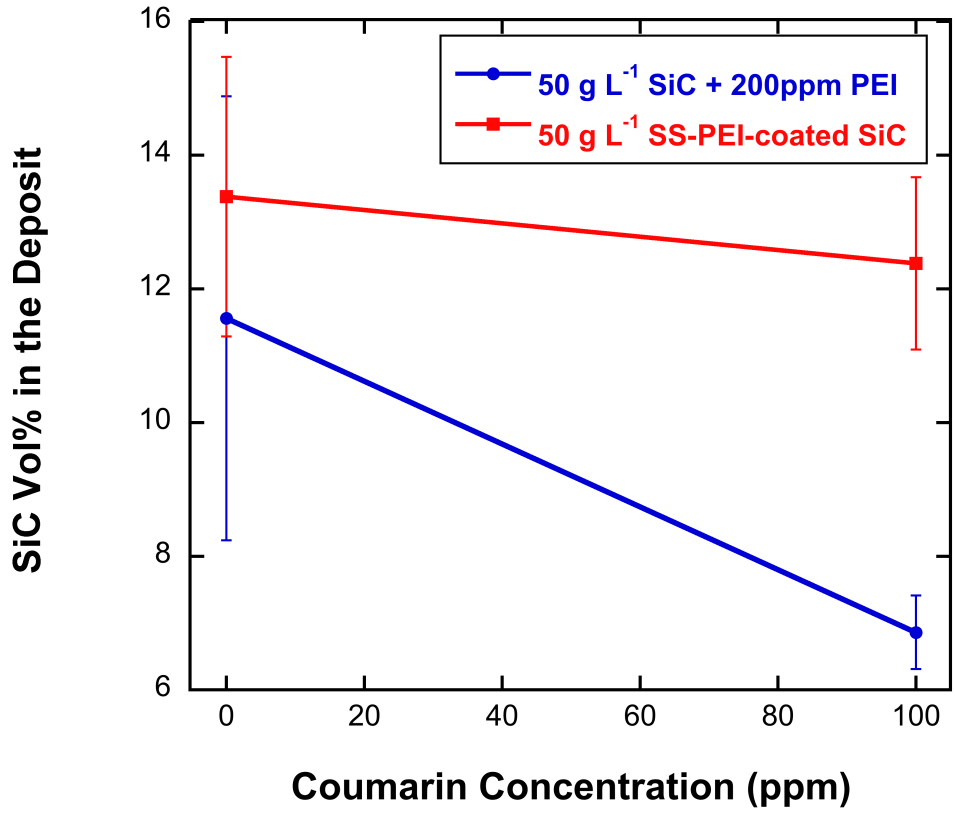

Figure 3.13. Effect of a leveling agent on SiC fraction in the deposit for micro-composites for two different cases: (a) 100 ppm coumarin is added into the plating bath with 50 g L^{-1} SiC and 200 ppm PEI and (b) 100 ppm coumarin is added into the plating bath with 50 g L^{-1} SS-PEI-coated SiC.

3.2. Summary

It is concluded that the addition of PEI of 60000 molecular weight at a concentration of 200 ppm increases the SiC vol% in the deposit significantly without decreasing the current efficiency. SiC incorporation increases with rotation speed for a Watts solution without any PEI whereas it is less dependent on mixing when PEI is present in the system. SiC fraction decreases at high current densities. PEI 1200 suppresses nickel deposition even at 50 ppm however the SiC incorporation is

significantly higher for the lower MW polymer. Importantly, it was seen that by pre-coating SiC particles with 1000 ppm PEI 60000 in either Watts bath or 0.1 M Na_2SO_4, the suppression of PEI on electrodeposition is eliminated while high dispersion is achieved. In addition, high SiC incorporation is obtained for all of the samples containing 50 g L^{-1} PEI60000-coated SiC. Pre-coating SiC particles with PEI 1200 also yields high SiC incorporation without decreasing the current efficiency however the dispersion of the particles in the solution is not improved with the addition of the lower MW PEI unlike PEI 60000. It has seen that using pre-coated particles in the presence of a leveling agent is favorable since the plating additives can alter the effect of dispersants when they are introduced to the particles at the same time. Finally, the life of a plating bath with pre-coated particles is at least one week without obvious caking and deterioration in composite properties. As a conclusion, the SiC pre-coating procedure described in this work is of significance.

3.3. References

1. D. Eroglu, A. Vilinska, P. Somasundaran and A. C. West, *Journal of the Electrochemical Society*, **160**, D35 (2013).

2. S. K. Kim, J. E. Bonevich, D. Josell and T. P. Moffat, *Journal of the Electrochemical Society*, **154**, D443 (2007).

3. S. K. Kim, D. Josell and T. P. Moffat, *Journal of the Electrochemical Society*, **153**, C616 (2006).

4. E. Garcia-Lecina, I. Garcia-Urrutia, J. A. Diez, M. Salvo, F. Smeacetto, G. Gautier, R. Seddon and R. Martin, *Electrochimica Acta*, **54**, 2556 (2009).

5. N. Guglielmi, *Journal of the Electrochemical Society*, **119**, 1009 (1972).

6. P. M. Vereecken, I. Shao and P. C. Searson, *Journal of the Electrochemical Society*, **147**, 2572 (2000).

7. M. Elimelech, J. Gregory, X. Jia and R. Williams, *Particle Deposition and Aggregation: Measurement, Modelling and Simulation*, Butterworth-Heinemann (1998).

8. M. Schlesinger and M. Paunovic, *Modern Electroplating*, John Wiley & Sons, Inc., New York (2000).

9. A. Vilinska, D. Eroglu, A. C. West, P. Somasundaran, in preparation.

CHAPTER 4*

ELECTRODEPOSITION OF Ni/SiC NANO-COMPOSITES IN THE PRESENCE OF POLYETHYLENEIMINE

The effect of PEI on the co-deposition of SiC with Ni is presented in Chapter 3 for micro-particles, and the incorporation of 45-55 nm SiC particles into Ni in the presence of the dispersant is discussed in this chapter. The pre-coating procedure that is developed for micro-particles in the previous chapter is extended to nano-particle incorporation. The surface morphology and roughness are also discussed and compared for micro- and nano-composites [4].

4.1. Results and Discussion

4.1.1. Effect of PEI on Nano-Particles

SiC vol% and current efficiency as a function of PEI concentration in the plating bath can be seen in Figure 4.1 for the nano-composite films. When there is no PEI in the electrolyte, the SiC fraction is very low (1.7 vol%). Under otherwise identical conditions, micro-particle incorporation results in a 5.9 vol% film. With increasing PEI concentration, the SiC vol% in the deposit increases significantly. It can also be seen that the current efficiencies are not affected until a PEI concentration of 500 ppm. Further increase in the PEI concentration causes a significant decrease in the current efficiency.

* D. Eroglu , A. Vilinska, P. Somasundaran, A.C. West, *Electrochim. Acta.* (submitted).

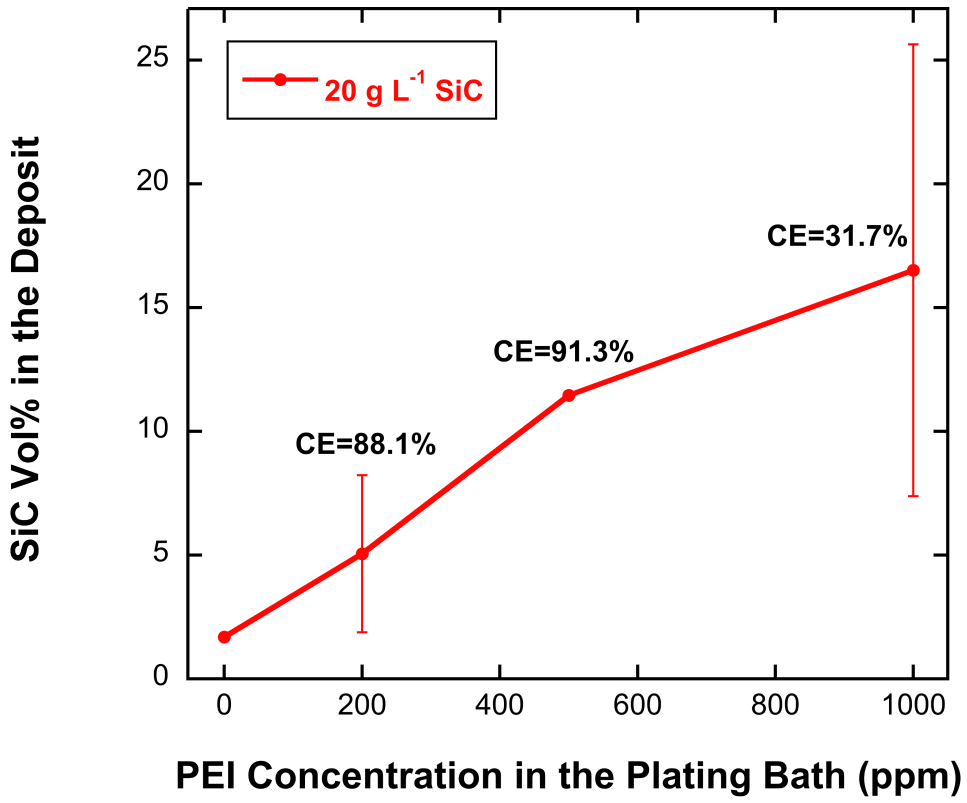

Figure 4.1. SiC fraction in the deposit and current efficiency as a function of PEI concentration in the plating bath for nano-composites. In all experiments, SiC bulk concentration was 20 g L^{-1}.

The pre-coating procedure developed for the micro-particles (discussed in Chapter 3) was successful in both increasing the SiC vol% in the deposit and in enhanced particle stability in the electrolyte without decreasing the current efficiency. In the micro-particle study, pre-coating the particles with 1000 ppm PEI did not cause any significant decrease in the current efficiency during plating. However the current efficiency for the nano-particles pre-coated with 1000 ppm of PEI is around 30%. This may be because the PEI that is adsorbed on the nano-particles during pre-coating desorbs more easily causing a high free polymer concentration in the plating bath. Or the PEI may substantially

increase overpotential even while remaining attached to the nano-particle. Regardless, 500 ppm PEI was used in the pre-coating procedure of the nano-particles as it provided stability without impacting current efficiency.

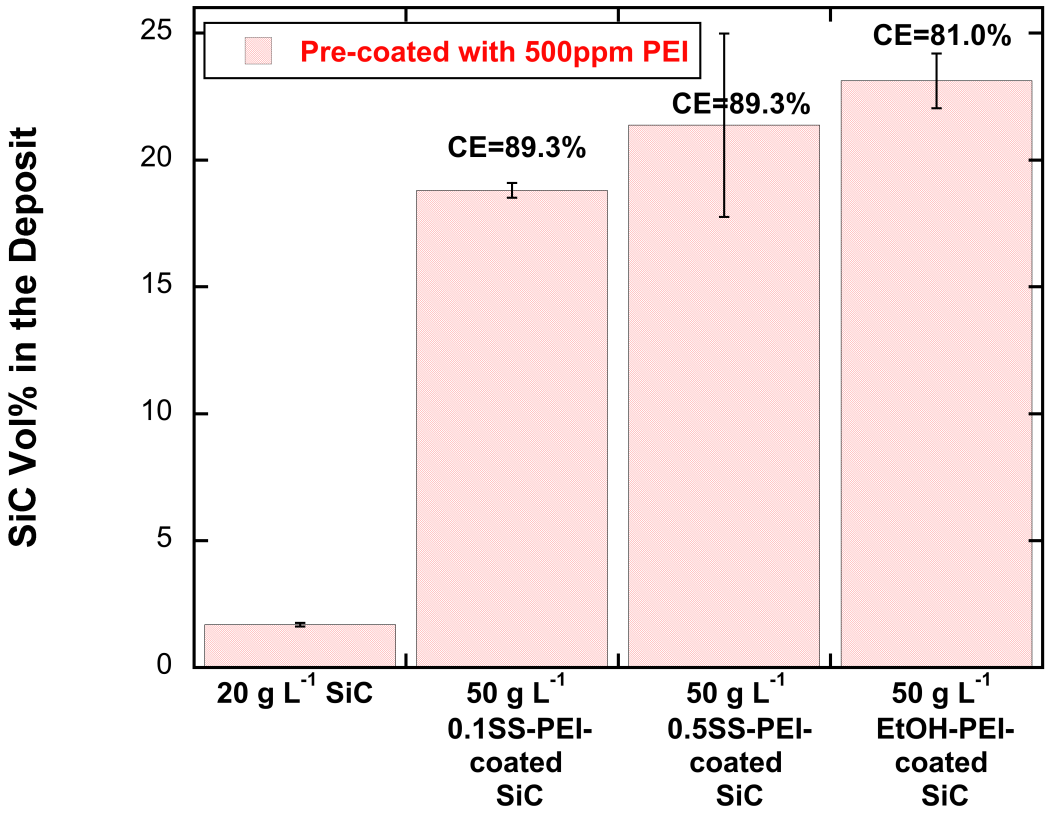

Figure 4.2. SiC fraction in the deposit for different pre-coating conditions for the nano-composites. SiC particles pre-coated with 500 ppm PEI in 0.1 M Na_2SO_4 (0.1SS-PEI-coated SiC) or in 0.5 M Na_2SO_4 (0.5SS-PEI-coated SiC) or in ethanol (EtOH-PEI-coated SiC) are compared with nonprecoated particles.

The SiC fraction in the deposit for different pre-coating baths can be seen in Figure 4.2. It is apparent that the pre-coating process results (columns 2-4) in a remarkable increase in the SiC incorporation. A SiC vol% as high as 23% is obtained.

This enhanced particle-incorporation rate is even greater than the increase seen for micro-composites. The current efficiencies are also indicated in the figure; there is no significant decrease for any of the pre-coating procedures shown here.

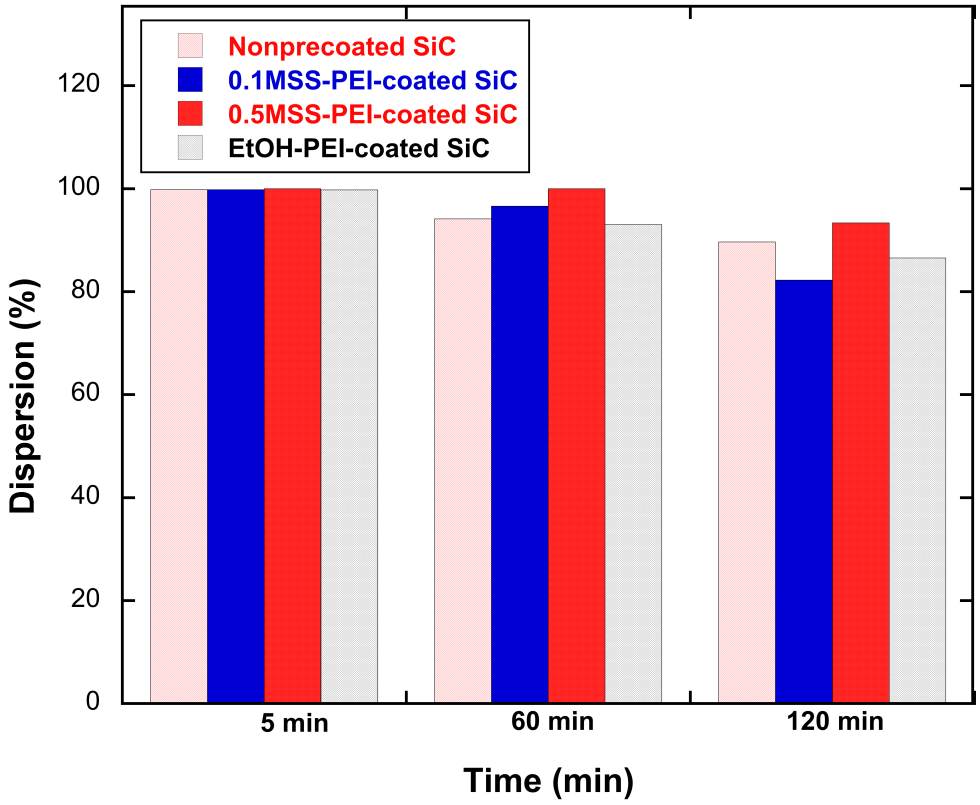

Figure 4.3. The dispersion of the nano-particles in the plating bath after 5, 60 and 120 min for different pre-coating procedures. In all experiments, SiC bulk concentration was 20 g L^{-1}.

The effect of pre-coating on the dispersion of nano-particles in the electrolyte can be seen from Figure 4.3. The dispersion of the suspensions is calculated by the evaluation of the settled volume after the solutions are prepared. The nano-particle suspensions are more stable compared to micro-particle suspensions (Chapter 3) when there is no PEI

present in the electrolyte with dispersion around 90% after 120 min. Although the settling results do not show significant differences, the sulfate pre-coated nano-particle (0.1SS-PEI-coated SiC and 0.5SS-PEI-coated SiC) dispersions are finely dispersed when observed under optical microscope compared to the heavily aggregated and entangled nano-particles without any PEI or the dispersions of EtOH-PEI-coated SiC particles. Therefore even though it is not apparent from the dispersion results, the agglomeration of nano-particles can be reduced with the pre-coating procedure.

Prevention of the agglomeration of the particles in the electrolyte may not be the only reason for the enhanced particle incorporation. In Chapter 6, it is proposed that particle incorporation rate depends on the residence time of an individual particle on the electrode. According to one interpretation of the mechanism, the residence time of nano-particles increases due to the pre-coating procedure because the PEI helps tether the particles to the electrode, resulting in high SiC loadings in the deposits.

In conclusion, with the pre-coating procedure described, good dispersion and very high incorporation rates can be achieved for the nano-particles without affecting the current efficiency.

4.1.2. Surface Morphology and Roughness of Micro- and Nano- Particles

SEM micrographs of micro-composites are presented in Figure 4.4. The pure Ni deposit shows pyramidal morphology as seen in Figure 4.4a. The addition of micro-particles alters the morphology; micro-composites have a rough and nodular surface (Figure 4.4b) perhaps because the Ni grains surround the SiC particles by forming globular aggregates [1]. It has been discussed that the introduction of the ceramic

particles disturbs the grain formation and decreases the grain size [1-3]. The introduction of 200 ppm PEI into the plating bath did not cause any significant change in the morphology of the composite films (Figure 4.4c). However from Figure 4.4d it is apparent that the pre-coated particles modify the surface morphology remarkably. The nodular surface structure is not observed, and the surface looks much smoother.

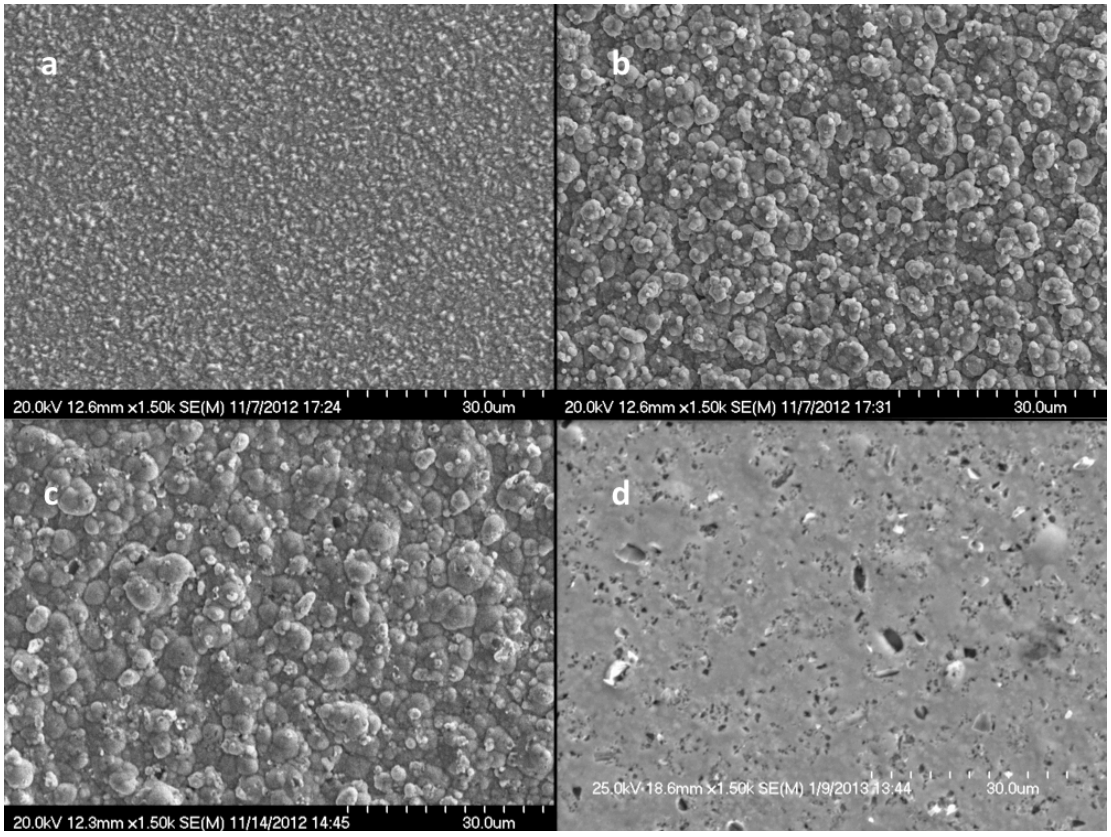

Figure 4.4. SEM micrographs of micro-composites at a magnification of 1500 for (a) Pure Ni deposit, (b) 50 g L^{-1} SiC in the plating bath (6.4 vol% SiC in the deposit), (c) 50 g L^{-1} SiC and 200 ppm PEI in the plating bath (11.6 vol% SiC in the deposit) and (d) 50 g L^{-1} W-PEI-coated SiC in the plating bath (14.0 vol% SiC in the deposit).

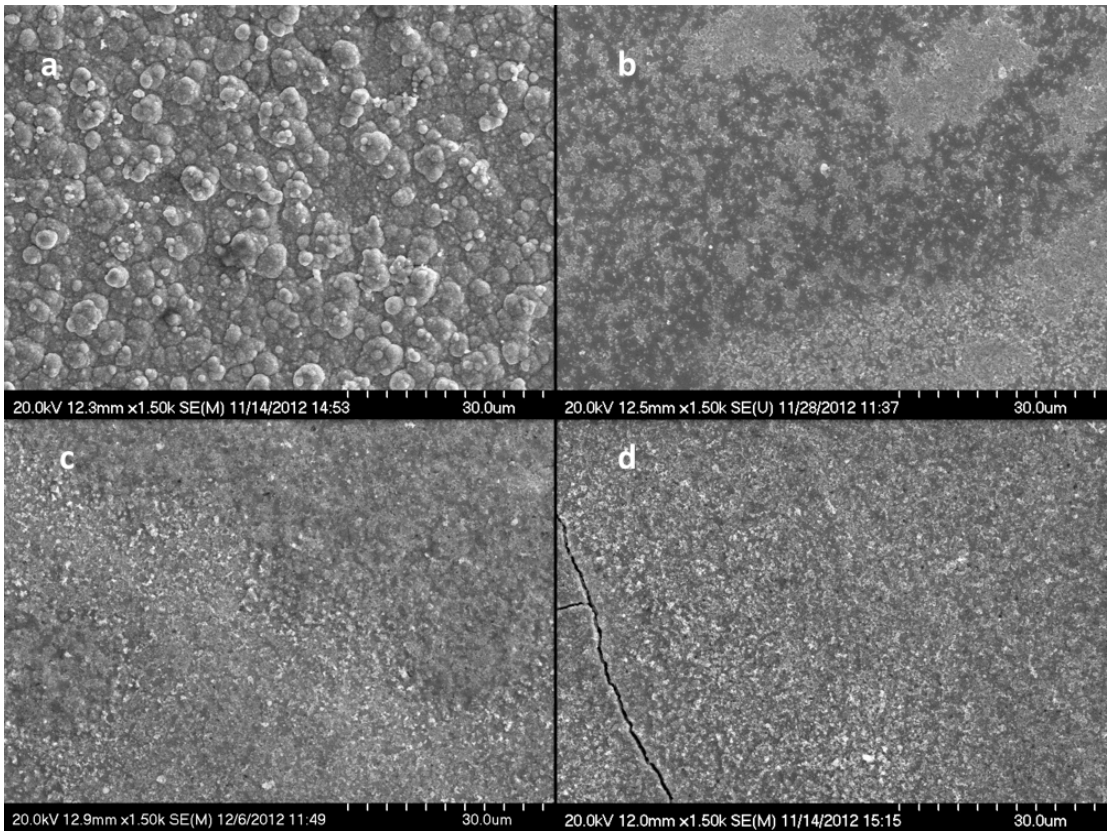

Figure 4.5. SEM micrographs of nano-composites at a magnification of 1500 for (a) 20 g L^{-1} SiC in the plating bath (1.7 vol% SiC in the deposit), (b) 50 g L^{-1} 0.1MSS-PEI-coated SiC in the plating bath (18.8 vol% SiC in the deposit), (c) 50 g L^{-1} 0.5MSS-PEI-coated SiC in the plating bath (21.4 vol% SiC in the deposit) and (d) 50 g L^{-1} EtOH-PEI-coated SiC in the plating bath (23.1 vol% SiC in the deposit). Microscopic cracks were seen when ethanol was used for pre-coating.

Figure 4.5 shows the effect of nano-particles on the surface morphology. The nano-composites (Figure 4.5a) show similar morphology to micro-composites in the absence of PEI. In addition, the SEM micrographs for the pre-coated nano-particles are very similar to each other showing a less rough surface. However, for the nano-composite films obtained from EtOH-PEI-coated SiC, cracks are observed on the surface (Figure

4.5d). These cracks may result from internal stresses due to high SiC loadings or because of residual ethanol on the pre-coated particles.

The nano-composite films obtained in the presence of 500 ppm PEI in the plating bath showed major cracks (visible to eye) on the deposit surface. These cracks were different than the ones shown in Figure 4.5d. Thus, even though the addition of 500 ppm PEI directly into the plating bath does not decrease the current efficiency, it resulted in undesired film properties; perhaps excess adsorption of the polymer on the deposit makes it very brittle. This detrimental effect of PEI is eliminated with the pre-coating procedure.

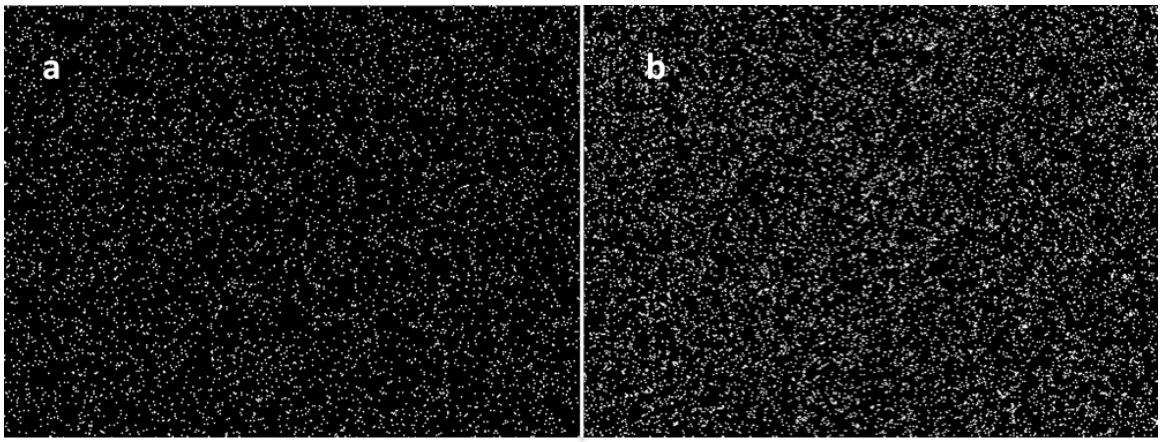

Figure 4.6. Si maps of micro-composites at a magnification of 250 for (a) 50 g L^{-1} SiC and (b) 50 g L^{-1} W-PEI-coated SiC in the plating bath.

Figures 4.6 and 4.7 show Si maps for the micro- and nano-composites with pre-coated SiC particles. For all cases, micro-composites are homogeneously dispersed, showing a uniform Si map (Figure 4.6). Nano-composites containing pre-coated particles (Figure 4.7) show some SiC aggregates although the majority of the films are uniform. Possibly, the agglomeration of the nano-particles in the electrolyte may not be fully

prevented, causing the particles to incorporate as bigger sizes at some positions on the electrode.

The surface roughness of the micro- and nano-composites are presented in Figure 4.8. Consistent with the SEM micrographs, the addition of the SiC particles increases the surface roughness for both the micro- and nano-composites. While the addition of 200 ppm PEI does not change the surface roughness (Figure 4.8a), the pre-coating procedure results in much lower surface roughness for both micro- and nano-composites especially for the nano-composite with EtOH-PEI-coated SiC.

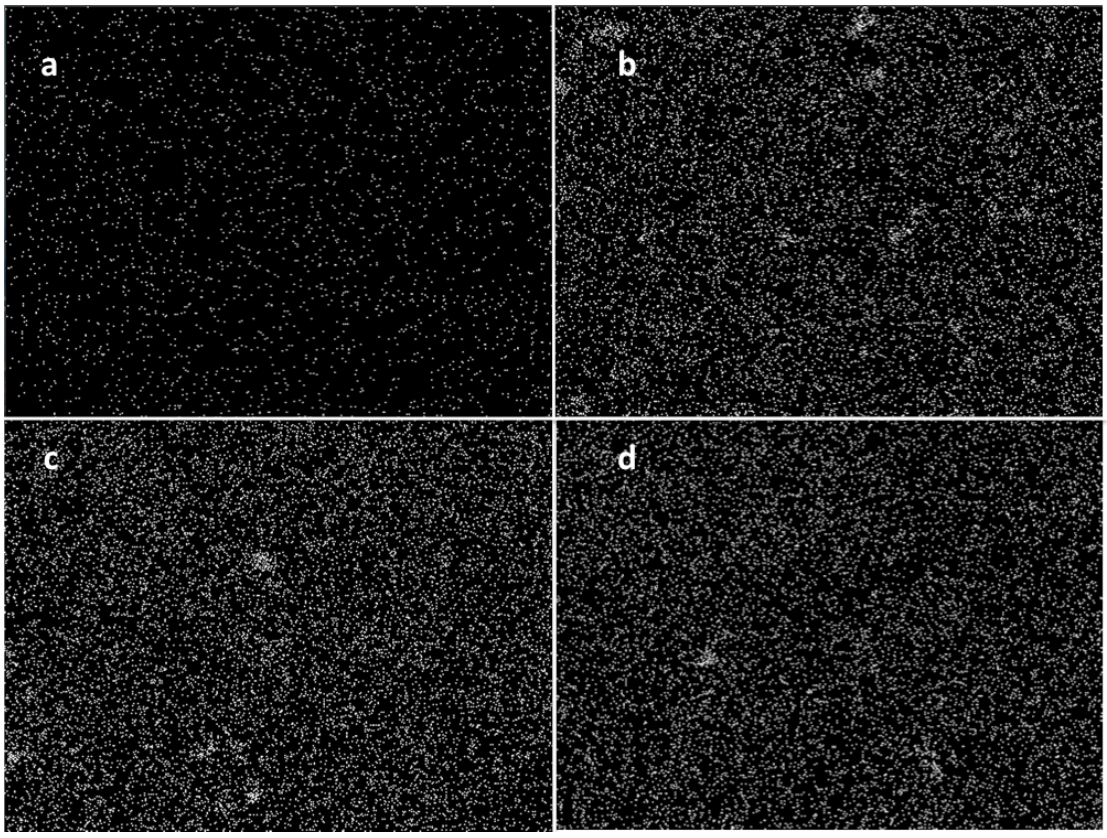

Figure 4.7. Si maps of nano-composites at a magnification of 250 for (a) 20 g L^{-1} SiC, (b) 50 g L^{-1} 0.1SS-PEI-coated SiC, (c) 50 g L^{-1} 0.5SS-PEI-coated SiC and (d) 50 g L^{-1} EtOH-PEI-coated SiC in the plating bath.

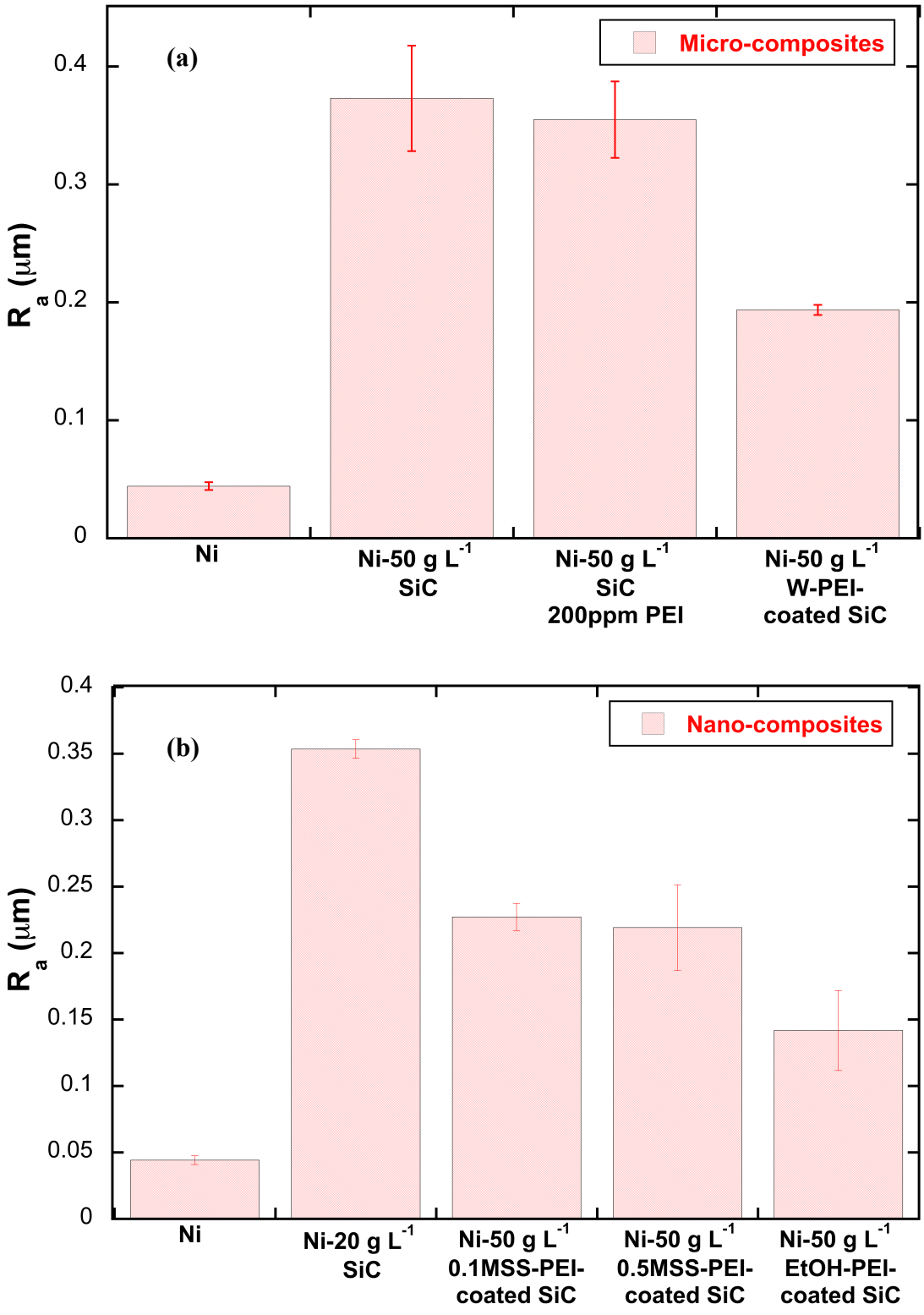

Figure 4.8. Roughness of (a) micro- and (b) nano-composites in the presence of PEI.

Finally, the Vickers hardness measurements show that with the pre-coating procedure hardness of the films increases significantly; incorporation of 14 vol% W-PEI-coated SiC micro-particles (50 g L^{-1} in the plating bath) into Ni film increases the hardness from 280 HV to 503 HV.

4.2. Summary

The addition of 500 ppm PEI into the plating bath increases the SiC fraction in the deposit without affecting the current efficiency. However at this concentration, the mechanical properties of the films are poor showing cracks that are visible to eye. When pre-coated nano-particles are used SiC fractions as high as 23 vol% are obtained in the composites. In addition, the nano-particles are well dispersed in the electrolyte. The pre-coating procedure also leads to smoother and harder deposits.

4.3. References

1. M. Lekka, A. Lanzutti, C. Zanella, G. Zendron, L. Fedrizzi and P. L. Bonora, *Pure and Applied Chemistry*, **83**, 295 (2011).

2. L. Benea, P. L. Bonora, A. Borello, S. Martelli, F. Wenger, P. Ponthiaux and J. Galland, *Journal of the Electrochemical Society*, **148**, C461 (2001).

3. C. Zanella, M. Lekka and P. L. Bonora, *Journal of Applied Electrochemistry*, **39**, 31 (2009).

4. D. Eroglu , A. Vilinska, P. Somasundaran, A.C. West, *Electrochim. Acta.* (submitted).

CHAPTER 5*

MATHEMATICAL MODELING OF Ni/SiC CO-DEPOSITION IN THE PRESENCE OF A CATIONIC DISPERSANT

In Chapters 3 and 4, the effect of a cationic dispersant, PEI on the incorporation of 1 μm or 45-55 nm SiC particles into Ni is discussed as a function of different system variables. In this chapter, a mathematical model of Ni/SiC co-deposition is proposed. The model provides a framework to explain the increase of the SiC incorporation rate due to a cationic dispersant. This is significant since none of the previous mechanisms discuss this effect. The effect of current density, rotation speed, SiC bath concentration and particle size on the incorporation rate is also analyzed according to the model developed [8].

5.1. Model of Particle Co-Deposition

The proposed mechanism describes the incorporation of SiC particles in three steps: (1) mass transfer of the particles to the electrode surface, (2) adsorption of the particles and (3) incorporation of the particles into the film. The proposed mechanism is illustrated schematically in Figure 5.1.

In the first step, the particles in the bulk solution are carried to the electrode surface through the diffusion layer as discussed in the Vereecken model [1]. By inserting the Nernst-diffusion layer approximation and a Levich-diffusion layer thickness for the RDE into Fick's law, the particle flux N_p is assumed to be given by equation 1:

$$N_p = 0.621\upsilon^{-1/6} D_p^{\,2/3}\left(c_{p,\infty} - c_{p,0}\right)\Omega^{1/2} \tag{1}$$

* D. Eroglu and A. C. West, *Journal of the Electrochemical Society*, submitted.

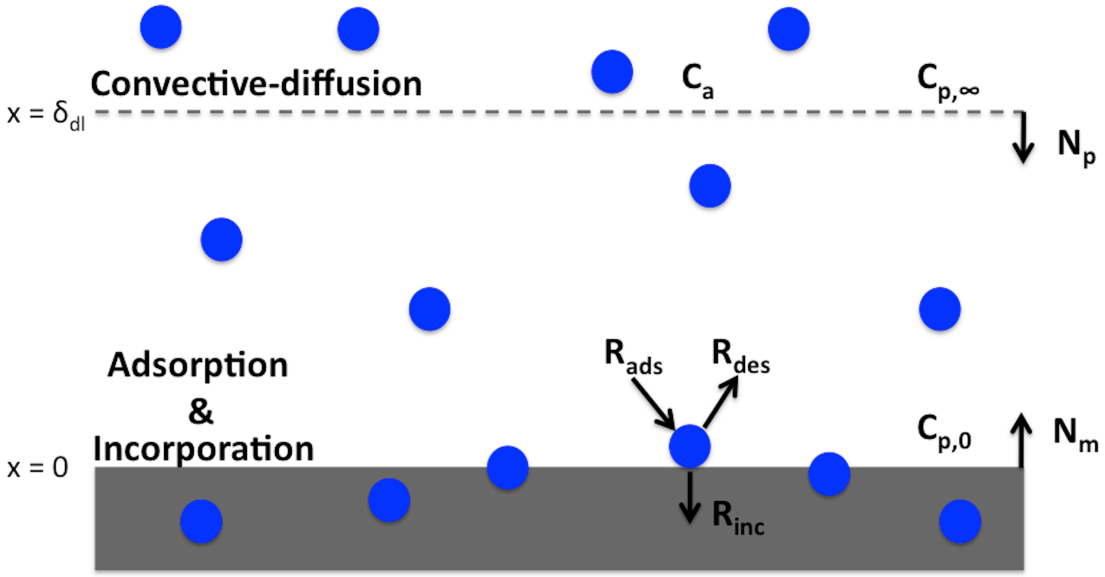

Figure 5.1. Schematic diagram of the diffusion layer. (1) The particles are carried to the electrode surface through the diffusion layer by convective-diffusion. (2) The particles are adsorbed on the electrode; they are in equilibrium with the particles on the surface. (3) If an adsorbed particle stays on the surface long enough, it gets incorporated by being buried into the growing Ni film.

The diffusion coefficient of the particles D_p (which are implicitly assumed to be Brownian) can be estimated according to the Stokes-Einstein equation. A value of 8.7×10^{-9} cm^2 s^{-1} is obtained from an estimate of the particle radius and viscosity of water at 50 ^{0}C. However, a value reduced by a factor of 1.5 allowed for a better agreement with experiment. This slightly lower value may be justified in part because the Watts solution has high ionic strength (2 M) and its viscosity can be higher than the assumed value. For instance, in the literature a 25% increase in viscosity is obtained for a 2 M NaCl solution [2]. In all calculations, the radius is assumed to be 500 nm. This value is based on TEM

images of the particles. However, the actual size of the particles in the Watts solution at high particle concentrations may be on average slightly higher due to agglomeration. This could also be a reason of the lower D_P value. In addition, Stokes-Einstein equation is valid for dilute suspensions, therefore high particle concentrations could be another factor decreasing the diffusion coefficient [3].

Particles near the electrode adsorb onto the electrode surface. The equilibrium surface coverage θ of the particles is assumed to be given by a Langmuir adsorption isotherm, where θ depends on the surface concentration of the particles $c_{p,0}$, which may differ from the bulk because of mass-transfer limitations (*c.f.,* equation 1).

$$\theta = \frac{Kc_{p,0}}{1 + Kc_{p,0}} \tag{2}$$

Equation 2 gives equilibrium coverage of particles, with an understanding that on and off rates are equal and individual particles are continually exchanged between the surface and the electrolyte. The average residence time of any individual particle on the electrode depends on the forward or backward rate. It is hypothesized here that incorporation occurs when the burial rate exceeds the residence time. Therefore the rate of incorporation, R_{inc} (particles cm^{-2} s^{-1}) should be proportional to the residence time τ_{res}, inversely proportional to the burial time τ_{burial} and proportional to the average number of particles on the surface $\theta \times \Gamma$:

$$R_{inc} \propto \tau_{res} \times \frac{1}{\tau_{burial}} \times \theta \times \Gamma \tag{3}$$

The flux of the particles to the surface is equal to the rate of incorporation of the particles into the deposit:

$$N_p = R_{inc} \tag{4}$$

The parameter τ_{burial} can be anticipated to be inversely proportional to the rate of Ni-electrodeposition, which is proportional to the total current through $i_{Ni} = i \times CE$. Additionally τ_{burial} depends on the size of the particle since it takes longer for a bigger particle to be engulfed by the co-depositing metal. Combined, we get:

$$\tau_{burial} \propto \frac{r_p}{|i_{Ni}|} \tag{5}$$

A particle that is adsorbed on the surface can only be incorporated if its residence time is large relative to burial time. Fransaer et al. [4] also implied this concept in their model by suggesting that a particle has to be immobilized on the surface to get incorporated. In their model, as long as the shear force on the particle F_{shear}, is smaller than the normal forces, the particle will get incorporated. A force balance on a particle on the surface shows that adhesion force F_{adh}, which is proportional to this immobilization force, increases with the rotation speed [4]. This effect of immobilization of a particle is incorporated into our model by the residence time, τ_{res}. Therefore, it is proposed that τ_{res} increases linearly with increasing rotation speed as the normal force on the particle increases. In addition, τ_{res} may depend on the current density since high Ni deposition rates can interfere with the particle incorporation because the integration of the reduced Ni into the substrate lattice necessarily requires displacement of other molecules, including possibly "anchors" of the particles. The residence time is thus assumed to be as in equation 6. The parameters that affect the burial and residence times of an individual particle adsorbed on the electrode are summarized schematically in Figure 5.2.

$$\tau_{res} \propto (c_1 - |i_{Ni}|)(\Omega + d_1) \tag{6}$$

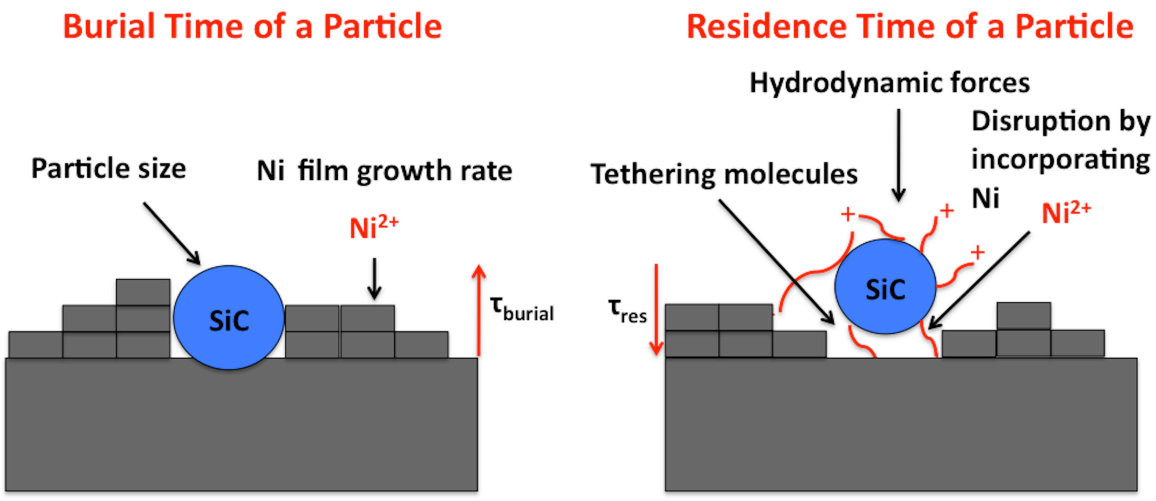

Figure 5.2. The burial and residence times of an individual particle on the surface. Burial time depends on the growth rate of Ni film and the particle size. Residence time is affected by the hydrodynamic forces, the presence of tethering molecules adsorbed on the particle surface and the disruption by incorporating Ni at high current densities.

In addition to the dependence of the burial time on r_p, the number of adsorption sites on the surface Γ also depends on the particle size as in equation 7:

$$\Gamma \propto \frac{1}{r_p^2} \tag{7}$$

Defining the incorporation rate constant k_{inc}, the proportionality in equation 3 can be written as

$$N_p = \frac{k_{inc}}{r_p^3}(c_1 - |i_{Ni}|)(\Omega + d_1)|i_{Ni}|\theta \tag{8}$$

In summary, in the model proposed, the incorporation rate of SiC particles depends on rotation speed Ω, current density i_{Ni}, bulk particle concentration $c_{p,\infty}$ and particle-radius r_p.

5.2. Results and Discussion

Fitting equation 8 to the experimental N_p data, (derived from experimental x_v data in Chapter 3) gives the parameters shown in Table 5.1. The effect of the PEI on these parameters and on the incorporation rate is perhaps the most interesting practical outcome, as discussed below. The diffusion coefficient of the particles was estimated as discussed in the previous section.

Table 5.1. Values of the parameters used in the model.

	$c_{a,b}$ = 0 ppm	$c_{a,b}$ = 200 ppm	Pre-coated SiC
K	10^5	10^5	10^5
c_1	0.16	0.16	0.16
k_{inc}	7.5×10^{-8}	6.3×10^{-8}	9.0×10^{-8}
d_1	54.0	108.0	108.0

The simulated incorporation rate as a function of the current density is shown in Figure 5.3. It can be seen that the model predictions of N_p are in good agreement with the experimental data. The model predicts that the particle incorporation increases with i_{Ni} at lower current densities and passes through a maximum. This nonlinear dependence of incorporation rate on i_{Ni} results because both τ_{res} and τ_{burial} are functions of i_{Ni}. However, the impact of i_{Ni} on burial time is more significant than its impact on residence time, as is evidenced by the fitted value of c_1 = 160 mA cm^{-2}.

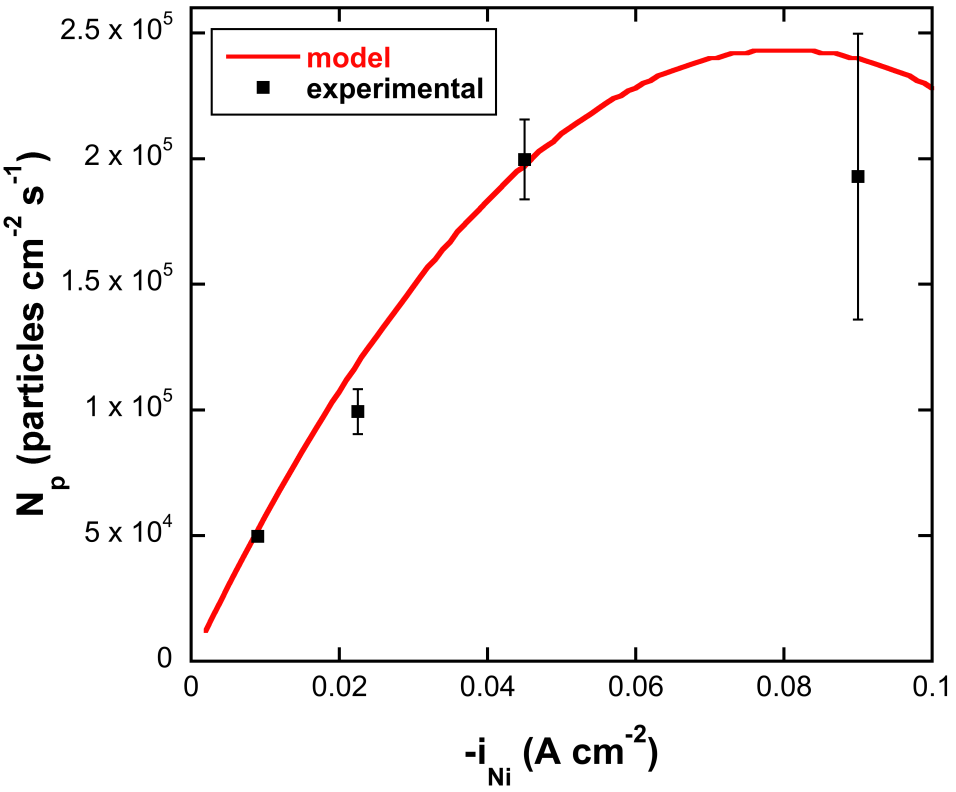

Figure 5.3. The incorporation rate predicted by the model as a function of current density for $c_a = 0$ ppm. SiC bulk concentration is 50 g L^{-1} and rotation speed is 100 rpm for all of the results.

Figure 5.4 shows the simulated effect of rotation speed on the incorporation rate. For these conditions, N_p increases linearly with increasing rotation speed. Increased rotation speed enhances the incorporation rate not only by increasing the SiC surface concentration through convection but also by affecting the residence time. The agreement of the model predictions with the experimental data on Figure 5.4 supports the linear dependence of N_p on the residence time, which is anticipated when the shear force is smaller than the normal forces acting on the particle. At very high rotation speeds, large shear forces can remove the adsorbed particles and therefore decrease the incorporation

rate, as discussed in the Fransaer model [4]. While it is beyond the scope of the present model, studies on particle incorporation rates in shear flow would be interesting.

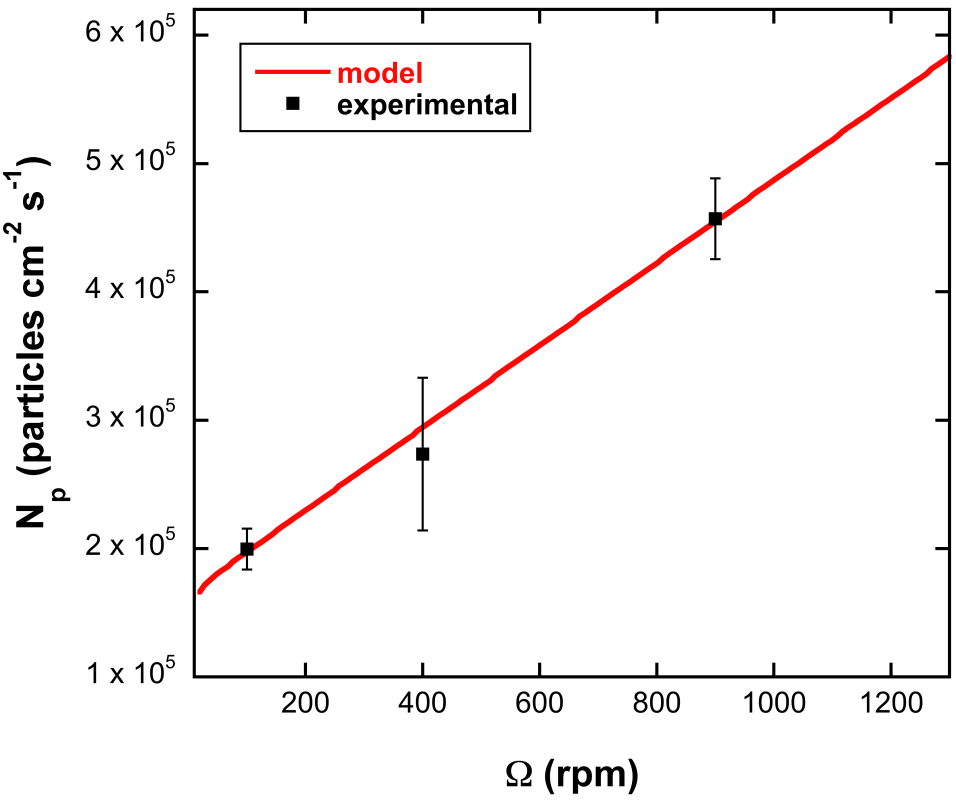

Figure 5.4. The incorporation rate predicted by the model as a function of rotation speed for c_a = 0 ppm. SiC bulk concentration is 50 g L^{-1} and current density is -50 mA cm^{-2} for all of the results.

The predicted incorporation rate as a function of SiC bulk concentration can be seen in Figure 5.5. The model predicts N_p to increase significantly with $c_{p,\infty}$ until a saturation point is reached in particle surface coverage. The experimental data suggest that surface coverage is saturated at 20 g L^{-1}, since the change in N_p for an increase in $c_{p,\infty}$

from 20 to 50 g L^{-1} is insignificant. The model predictions show close agreement to the experimental data.

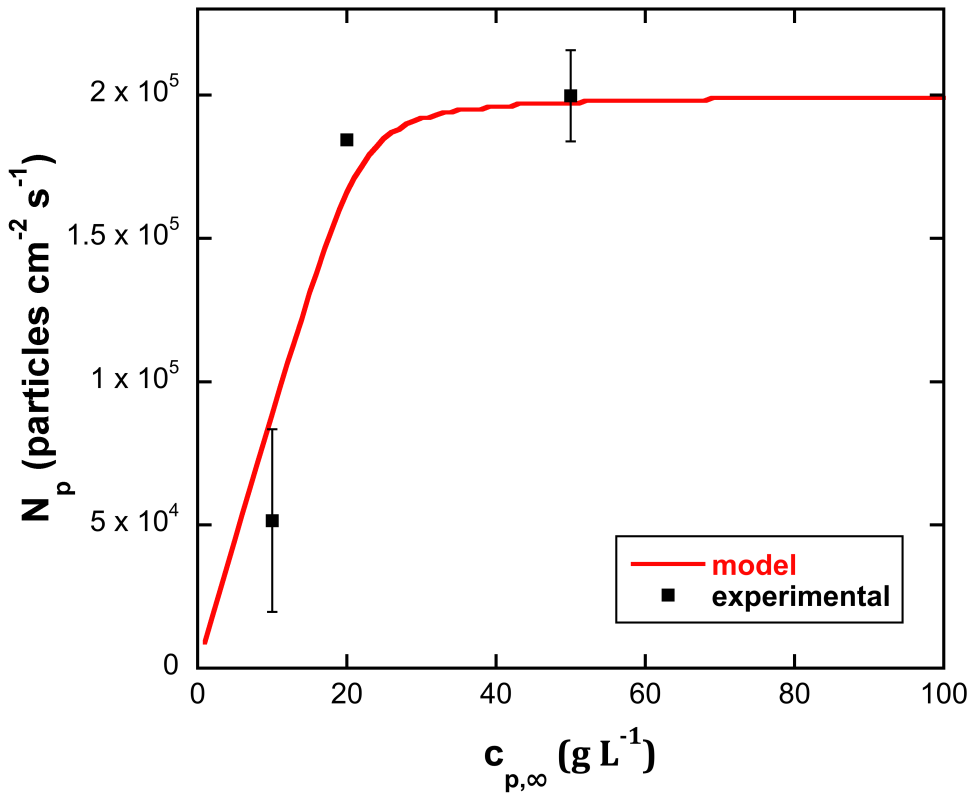

Figure 5.5. The incorporation rate predicted by the model as a function of SiC bulk concentration for c_a = 0 ppm. Current density is -50 mA cm^{-2} and rotation speed is 100 rpm for all of the results.

5.2.1. Effect of PEI on the Mechanism

A cationic dispersant, polyethyleneimine (PEI) stabilizes the particles in the electrolyte as discussed in Chapters 3 and 4. Effective dispersants may prove crucial for implementation of co-deposition processes in manufacturing of complex parts, as they allow for mitigation of sensitivity in film loading to flow. PEI also impacts the SiC

incorporation rate as discussed within the context of the present model. In one means of dispersing particles, 200 ppm PEI was added directly to the plating solution, along with the particles. In the second, more effective approach, SiC particles were pre-coated with 1000 ppm PEI in a different electrolyte and then introduced into the plating bath, without any additional PEI. The details of the pre-coating procedure are given in Chapter 2.2. The pre-coated particles display far superior stability in the electrolyte in terms of settling times. In addition, when these pre-coated particles are used in the plating bath, the SiC fraction in the deposit increases significantly without any decrease in current efficiency. The parameters obtained in the model for c_a = 200 ppm and pre-coated particles are shown in Table 5.1.

In Chapter 3, it was hypothesized that the increase in the incorporation rate with PEI is due to the adsorption of the polymer on the particle resulting in a higher affinity of the particles to the electrode. With the model, this statement can be refined. According to the mechanism, PEI increases the residence time of an individual particle. This can be due to the multiple additional binding sites between the particle and electrode, presumably through a PEI tethering mechanism. We have therefore assumed in fitting the model that only τ_{res} is changed by the PEI. The new values of k_{inc} and d_1 were determined by fitting the experimental N_p *vs* Ω data. It can be seen that the change in k_{inc}, is relatively small however d_1 increases by a factor of two with the addition of PEI. Practically, this implies that the residence time is less sensitive to rotation speed.

The experimental incorporation rates calculated using the experimental volume-fraction data for dispersant (PEI) concentrations of c_a = 0 and 200 ppm and pre-coated SiC particles are tabulated in Table 5.2. It can be seen from the table that N_p increases

with increasing PEI. In the proposed mechanism, this increase in N_p in the presence of the dispersant is explained through the residence time of the particles.

Table 5.2. The effect of PEI on the experimental incorporation rate, N_p for the micro-particles for $c_{p,\infty}$ = 50 g L^{-1}, i = -50 mA cm^{-2} and Ω = 100 rpm (N_p is calculated through the experimental x_v data presented in Chapter 3).

	N_p (particles cm^{-2} s^{-1})
c_a = 0 ppm	2.0×10^5
c_a = 200 ppm	3.8×10^5
Pre-coated SiC particles	4.8×10^5

The model predictions for the effect of disk rotation speed in the presence of PEI is presented in Figure 5.6 for c_a = 200 ppm. At very low rotation speeds Ω, mass-transfer limitations play a significant role and simulations suggest that rotation speed has an effect on θ, resulting in nonlinear Ω dependence. Figure 5.7 shows the model predictions for the incorporation rate as a function of the current density in the presence of PEI for two different cases. The model predictions are in fair agreement with the experimental data for both of the figures.

The model predictions for the effect of bulk particle concentration in the presence of PEI can be seen in Figure 5.8. For the two cases, the incorporation rates are predicted to be the same at low $c_{p,\infty}$. However, with increasing SiC bulk concentration, the use of pre-coated SiC results in higher incorporation rates. The improved stability of SiC

particles in the plating bath by the pre-coating procedure (zeta potentials and settling time results were reported in Chapter 3) suggests that the surface of the SiC particles are much more fully covered with PEI than when particles and PEI are simply introduced as is. This apparently results in a higher increase at the residence time of the particles on the surface. The experimental data shows good agreement with the model predictions.

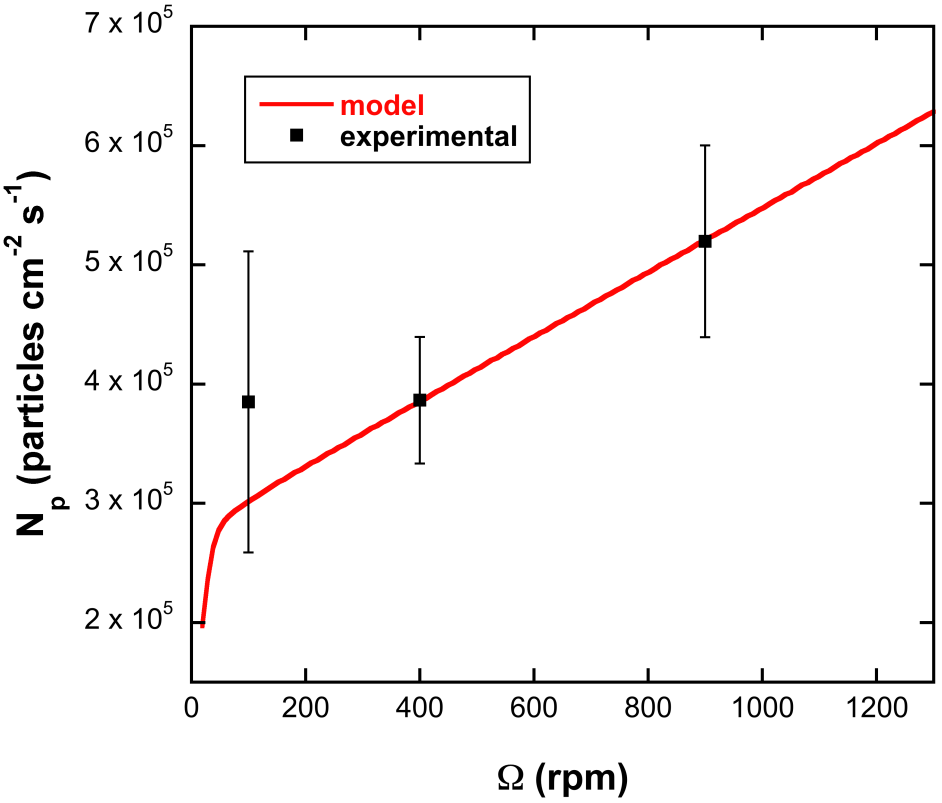

Figure 5.6. The incorporation rate predicted by the model as a function of rotation speed for c_a = 200 ppm. SiC bulk concentration is 50 g L^{-1} and current density is -50 mA cm^{-2} for all of the results.

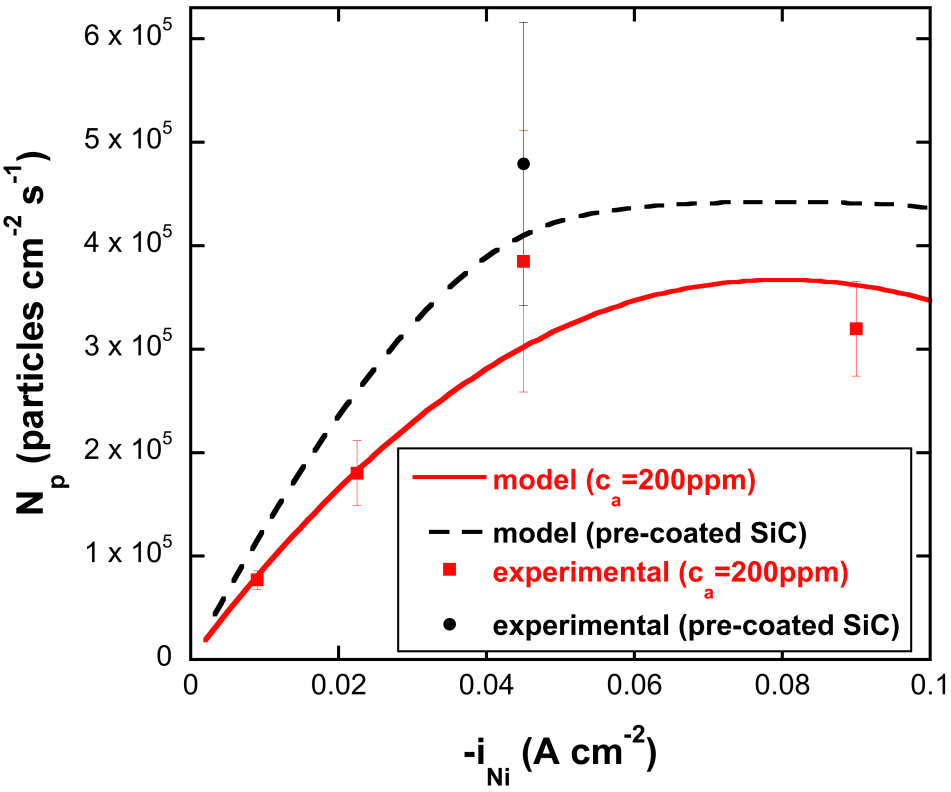

Figure 5.7. The incorporation rates predicted by the model as a function of current density for c_a = 200 ppm and pre-coated SiC particles. SiC bulk concentration is 50 g L^{-1} and rotation speed is 100 rpm for all of the results.

5.2.2. Effect of Particle Size on the Mechanism

Particle size has a significant influence on the incorporation rate, and nano- to micro-particles are compared in this section. It is known that nano-particles tend to agglomerate in the solution and act as bigger sized aggregates during incorporation [6, 7]. The radius of the nano-particles used in the simulations is therefore taken as 75 nm instead of 25 nm estimated from TEM (dynamic light scattering measurements also suggest this increase in the particle size).

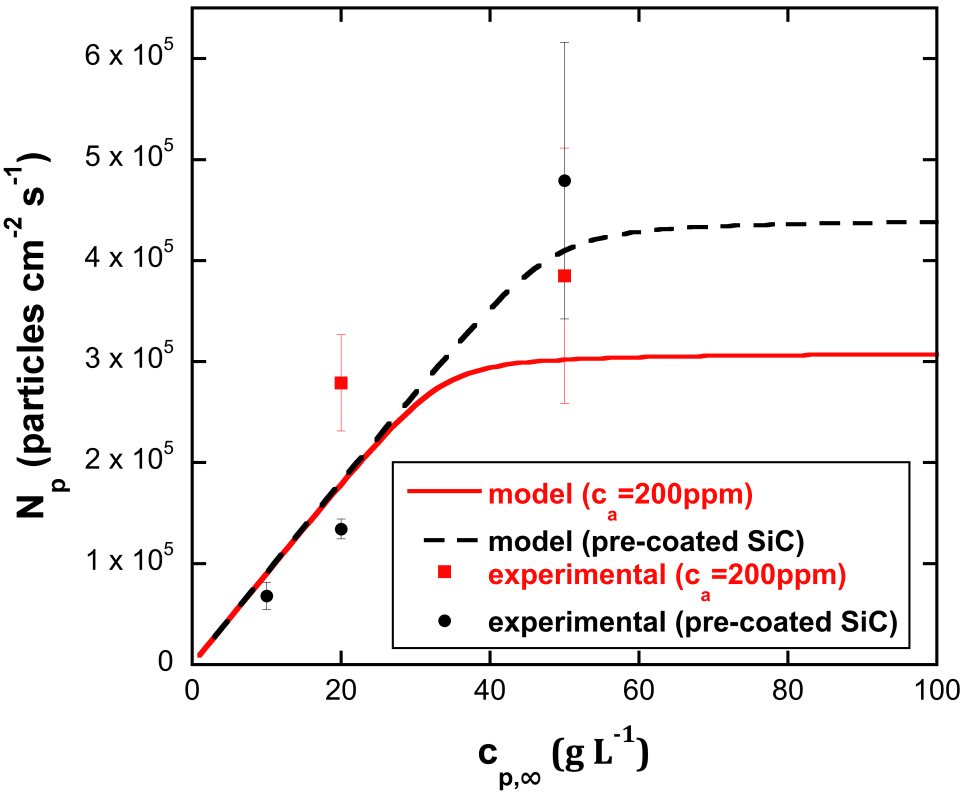

Figure 5.8. The incorporation rate predicted by the model as a function of SiC bulk concentration for c_a = 200 ppm and pre-coated SiC particles. Current density is -50 mA cm^{-2} and rotation speed is 100 rpm for all of the results.

Assuming a particle size of 150 nm, the diffusion-coefficient D_p that is estimated as 5.8×10^{-9} for the micro-particles increases to 3.8×10^{-8} cm^2 s^{-1} for the nano-particles (these values are 1.5 times smaller than D_p calculated by Stokes-Einstein as discussed before). The burial time and Γ are also affected by particle size according to equations 5 and 7, respectively. However the particle size may also change the residence time, and the two constants, k_{inc} and d_1 were fit to N_p vs Ω data to get 4.1×10^{-8} and 20.0, respectively. This suggests that residence time of nano-particles is smaller than micro-particles. This could possibly be explained by the immobilization force acting on a single

particle on the surface being lower for smaller particles [4]. Therefore, the hydrodynamic forces acting on the SiC particle adsorbed on the surface is less significant for the nano-particles.

When the experimental incorporation rates are compared for nano and micro SiC particles (c_a = 0 ppm), it has seen that N_p increases from 1.8×10^5 to 1.5×10^7 particles cm^{-2} s^{-1}; more than 80 times. According to equation 8, N_p is proportional to r_p^{-3} suggesting that the incorporation rate may increase by around 300 times for the nano-particles if all other parameters are unchanged since the ratio of micro- ($r_{p,micro}$ = 500 nm) to nano-particle size ($r_{p,nano}$ = 75 nm) is 6.7 in the model. The smaller increase seen for the experimental data may be partly due to a decrease in τ_{res} of the nano-particles.

To examine the effect of PEI on nano-particle incorporation, experimental N_p values for the two cases with PEI are compared with c_a = 0 ppm. The incorporation rate N_p increases from 1.5×10^7 to 4.7×10^7 particles cm^{-2} s^{-1} with the addition of 200 ppm PEI into the plating bath. The increase in the incorporation rate with the pre-coating procedure is even larger; N_p increases to 1.6×10^8 particles cm^{-2} s^{-1}; a factor of ten. This may indicate that the increase in the residence time with the addition of the polymer is much higher for nano-particles than micro-particles, especially when the pre-coating procedure is used. Another possible explanation for this may be the reduction of agglomeration of the nano-particles in the bulk, in the presence of PEI.

The incorporation rate predicted by the model as a function of rotation speed is compared with the experimental data in Figure 5.9. It can be seen that, although the dependence of τ_{res} on the rotation speed has changed (significantly different d_1), the linear dependence is still a fair approximation for the nano-particles.

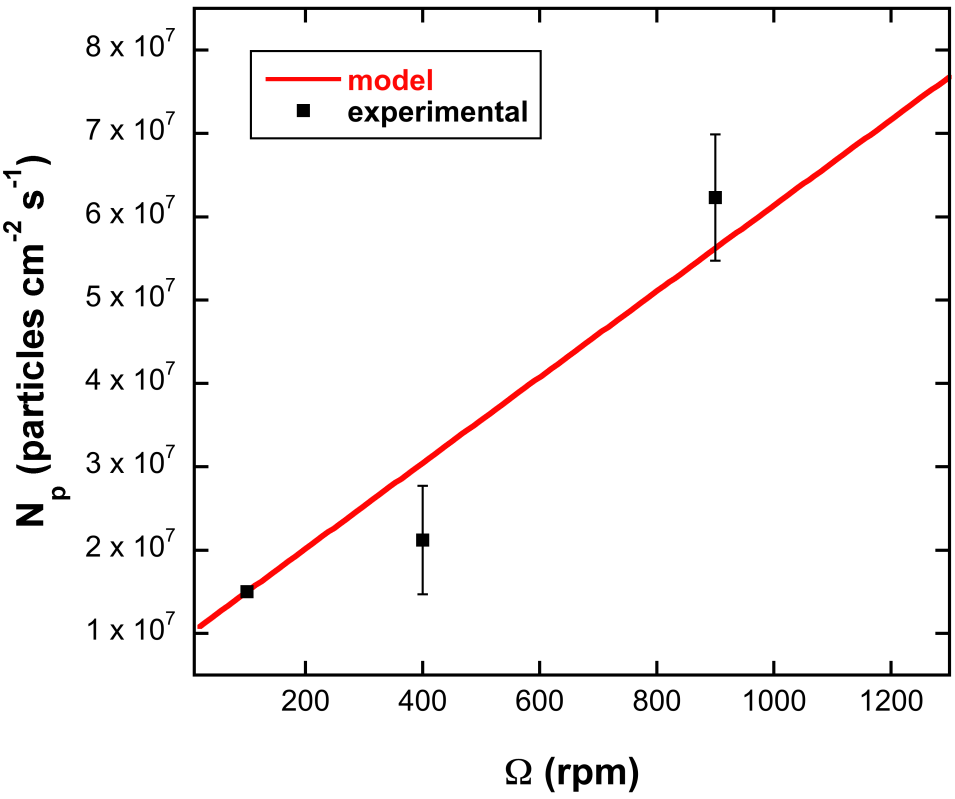

Figure 5.9. The incorporation rate predicted by the model for nano-particles as a function of rotation speed for $c_a = 0$ ppm. SiC bulk concentration is 20 g L^{-1} and current density is -50 mA cm^{-2} for all of the results.

5.2.3. Model Predictions for the SiC Volume Fraction in the Deposit

The volume fraction of the particles in the deposit x_v, which is a parameter that is perhaps the most easily measured, can be calculated from the ratio of the flux of particles to the metal ions according to:

$$\frac{x_v}{1-x_v} = \frac{N_p}{N_m}\left(\frac{MW_p \rho_{Ni}}{MW_{Ni}\rho_p}\right) \tag{9}$$

where the flux of the metal ions into the growing film N_m is calculated by Faraday's law:

$$N_m = \frac{|i_{Ni}|}{2F} \tag{10}$$

In the calculation of the metal flux, the *CE* is assumed to be constant at 90%. This value is close to the experimentally measured current efficiency for all of the data considered here.

Simulations can predict the SiC incorporation rate as a function of operating conditions, i_{Ni}, Ω and $c_{p,\infty}$ as described in the previous sections. In addition, by using equation 9, the volume fraction of SiC in the deposit can be estimated. The volume fraction may be of interest for prediction of film properties. The model predictions for SiC volume fraction as a function of current density and rotation speed for the micro- and nano-particles at different PEI concentrations can be seen in Figures 5.10 and 5.11, respectively. These figures summarize the effects of PEI and particle size on the SiC fraction in the deposit.

It can be seen in Figure 5.10a that the volume fractions are appreciably higher in the presence of PEI. Although the incorporation rate increases with the current density, the volume fraction x_v does not because N_m increases at a higher rate than N_p. It can also be seen that for the pre-coated particles, the change in θ is more significant, resulting in a nonlinear decrease in x_v, unlike the other cases. The conclusions made in Figure 5.10a about the effect of PEI are also valid in Figure 5.10b. The predicted SiC fraction in the deposit for nano-particles as a function of current density and rotation speed can be seen in Figure 5.11. The model predicts that the pre-coated nano-particles to give the highest volume fractions.

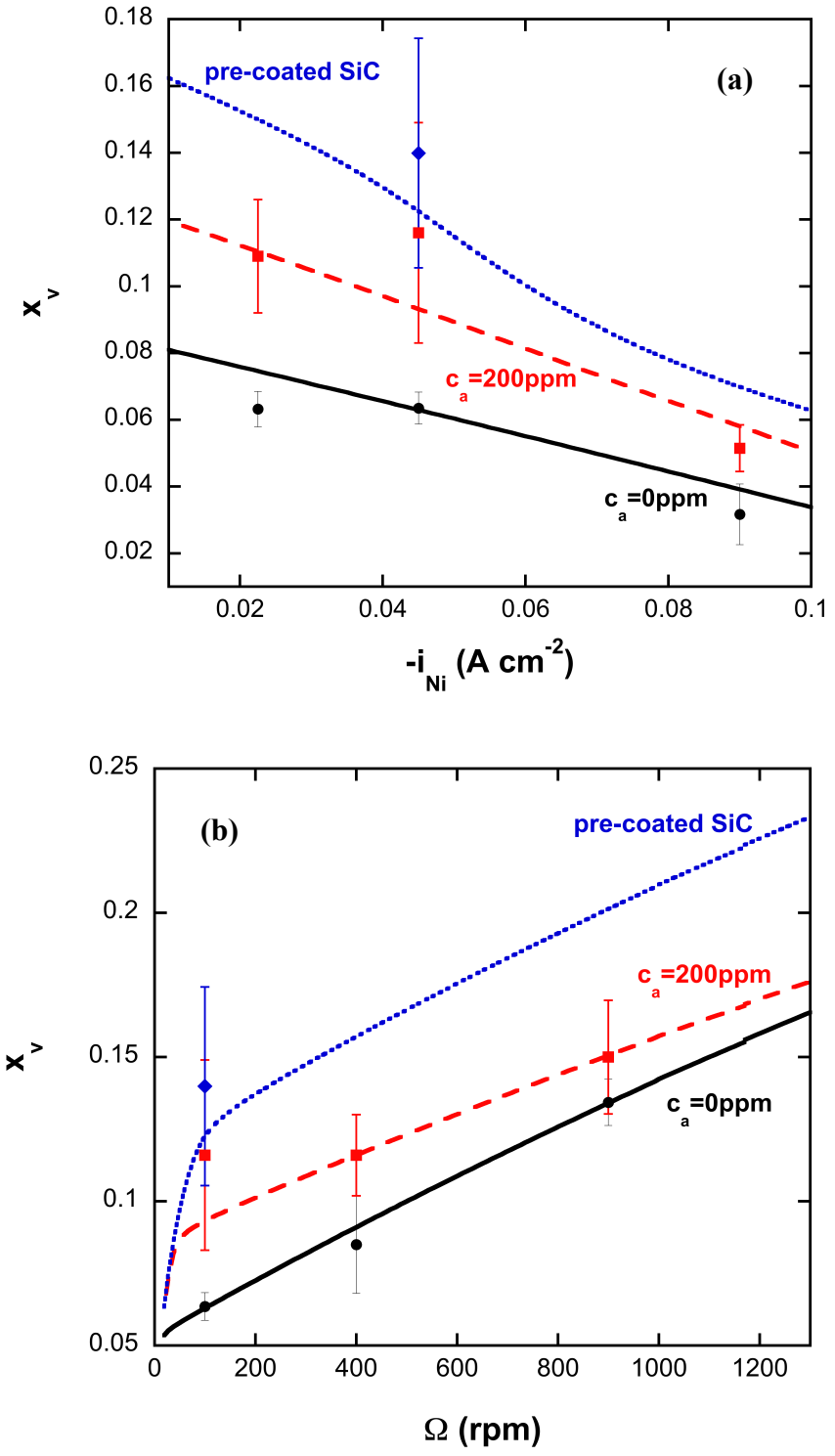

Figure 5.10. The model predictions for SiC volume fraction in the deposit as a function of (a) current density and (b) rotation speed for micro-particles at different PEI concentrations ($c_{p,\infty}$ = 50 g L^{-1} and (a) Ω=100 rpm and (b) i = -50 mA cm^{-2}).

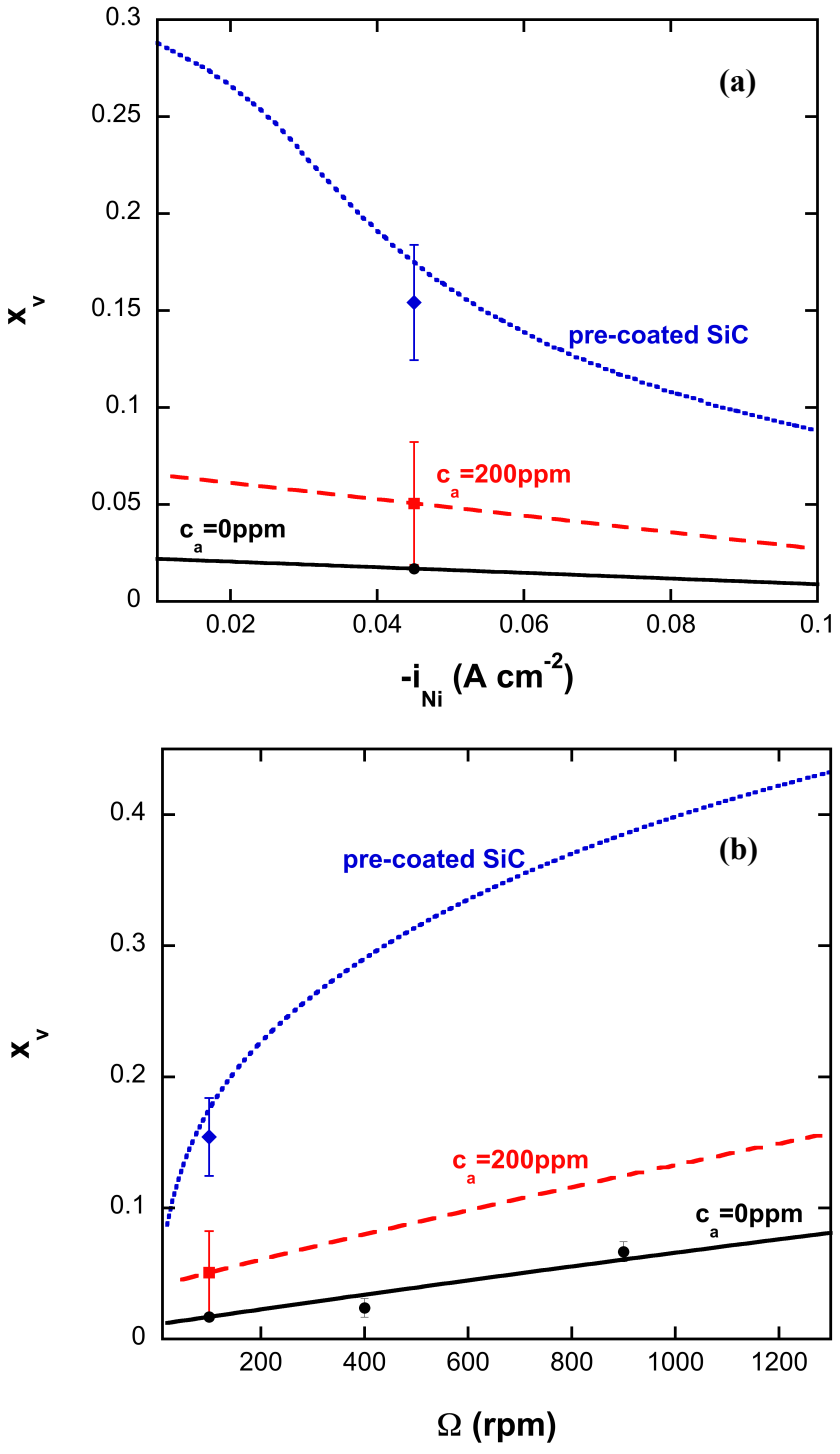

Figure 5.11. The model predictions for SiC volume fraction in the deposit as a function of (a) current density and (b) rotation speed for nano-particles at different PEI concentrations ($c_{p,\infty}$ = 20 g L^{-1} and (a) Ω=100 rpm and (b) i = -50 mA cm^{-2}).

The proposed mechanism provides a framework for explaining the effect of a cationic dispersant on the incorporation rate of ceramic particles. However the present model cannot predict the change of the model parameters with the addition of the dispersant. Thus, further theoretical progress is required to allow for an *a priori* prediction of the impact of dispersant on incorporation rates. Likewise, experimental investigations of the impact of hydrodynamic effects (impingement *vs*. shear flows) will allow for further refinement of the model.

5.3. Summary

In this chapter, incorporation of SiC particles into Ni in the presence of a cationic dispersant PEI is described with a three-step model: (1) mass transfer of the particles to the electrode surface, (2) adsorption and (3) incorporation by burial in the growing Ni film. The incorporation rate depends on the residence and burial times of particles and is proportional to the average number of particles adsorbed on the surface. Current density affects the incorporation rate through both the residence and burial times. The residence time is also dependent on flow conditions as well as the current density. For a rotating disk electrode, increasing the rotation speed enhances the incorporation rate not only by increasing the transport of the particles to the surface but also increasing the residence time of the adsorbed particles. The increased incorporation rate with the addition of PEI is explained through an increase in the residence time due to the adsorbed PEI on the SiC surface. Finally the effect of the particle size on the incorporation rate is discussed. Smaller particles are transported to the surface more readily, adsorb at higher number densities, have smaller burial times, but also decreased average residence times.

5.4. List of Symbols

c_a- bulk concentration of PEI (ppm)

$c_{p,\infty}$ - bulk concentration of the particles (particles cm^{-3})

$c_{p,s}$ - surface concentration of the particles (particles cm^{-3})

CE - current efficiency (%)

c_1 - constant (A cm^{-2})

d_1 - constant (rad s^{-1})

D_p - diffusion coefficient of the particles (cm^2 s^{-1})

F - Faraday's constant (C mol^{-1})

i - current density (A cm^{-2})

i_{Ni} - current density for Ni-deposition (A cm^{-2})

K - Langmuir adsorption constant (cm^3 mol^{-1})

k_{inc} - incorporation rate constant (s^{-1})

MW_p - molecular weight of SiC (g mol^{-1})

MW_{Ni} - molecular weight of Ni (g mol^{-1})

N_m - metal ion flux (mol cm^{-2} s^{-1})

N_p - particle flux (particles cm^{-2} s^{-1})

n - number of electrons transferred per ion

r_p - particle radius (cm)

R_{inc} - rate of incorporation (particles cm^{-2} s^{-1})

x_v - volume fraction of particles in the deposit

Greek letters

υ - kinematic viscosity of the electrolyte ($cm^2\ s^{-1}$)

Ω - rotation speed (rad s^{-1})

θ - surface coverage

Γ - total number of particles on the surface per area (particles cm^{-2})

τ_{res} - residence time (s)

τ_{burial} - burial time (s)

ρ_p - density of SiC (g cm^{-3})

ρ_{Ni} - density of Ni (g cm^{-3})

5.5. References

1. P. M. Vereecken, I. Shao and P. C. Searson, *Journal of the Electrochemical Society*, **147**, 2572 (2000).

2. J. Kestin, H. E. Khalifa and R. J. Correia, *Journal of Physical and Chemical Reference Data*, **10**, 71 (1981).

3. P. C. Hiemenz and R. Rajagopalan, *Principles of colloid and surface chemistry*, Marcel Dekker, Inc., New York (1997).

4. J. Fransaer, J. P. Celis and J. R. Roos, *Journal of the Electrochemical Society*, **139**, 413 (1992).

5. D. Eroglu, A. Vilinska, P. Somasundaran and A. C. West, *Journal of the Electrochemical Society*, **160**, D35 (2013).

6. C. Cai, X. B. Zhu, G. Q. Zheng, Y. N. Yuan, X. Q. Huang, F. H. Cao, J. F. Yang and Z. Zhang, *Surface & Coatings Technology*, **205**, 3448 (2011).

7. C. T. J. Low, R. G. A. Wills and F. C. Walsh, *Surface and Coatings Technology*, **201**, 371 (2006).

8. D. Eroglu and A. C. West, *Journal of the Electrochemical Society*, submitted.

CHAPTER 6*

MATHEMATICAL MODELING OF REACTION KINETICS AND TRANSPORT IN THE POSITIVE POROUS ELECTRODE IN A SODIUM-IRON CHLORIDE BATTERY

In the second part of this dissertation, a sodium-metal chloride battery, which is another important electrochemical system, is studied. In this chapter, a one-dimensional mathematical model of the porous cathode of a sodium-iron chloride battery for an isothermal, constant-current discharge-charge cycle is presented. In sodium-iron chloride batteries, it is desirable to maintain low $FeCl_2$ solubility to minimize redistribution of active material in the cell. However, the iron chloride is sparingly soluble, and with increased cycling, it does redistribute. None of the previous models can predict this movement of the metal that takes place in the cell with increased cycling that can cause the failure of the cell. An advance offered by the model presented in this chapter is that it accounts for the change in the solubility of $FeCl_2$ within the cell and predicts the relocation of the iron [1].

6.1. Model of Reaction Kinetics and Transport in the Cathode

The isothermal, constant current discharge-charge of a Na-$FeCl_2$ battery is represented using a one-dimensional, cylindrical model. As seen in Figure 6.1, the cell is composed of six parts: the cathode current collector ($r<r_0$), the positive porous Fe/$FeCl_2$ electrode (between r_0 and r_L), the sodium tetrachloroaluminate reservoir (between r_L and

* D. Eroglu and A. C. West, *Journal of Power Sources*, **203**, 211 (2012).

r_S), the β"-alumina solid electrolyte (between r_S and r_A), the negative liquid sodium electrode (between r_A and r_C) and the anode current collector [2]. In this study, only the positive porous electrode is modeled.

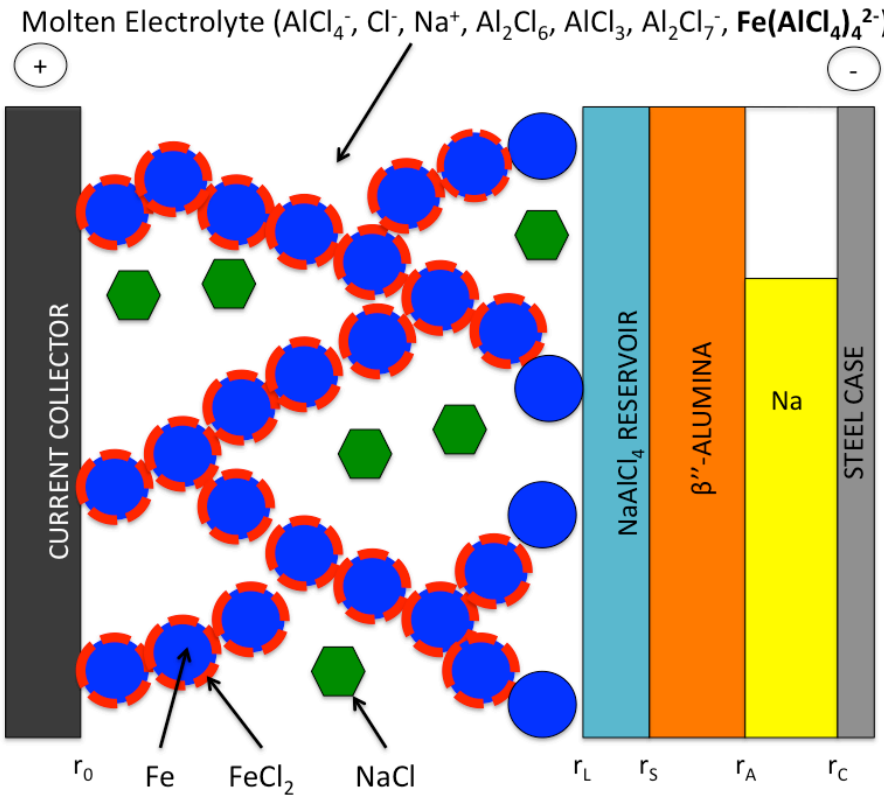

Figure 6.1. Schematic diagram of the sodium-metal chloride cell in the model.

The positive porous electrode (between r_0 and r_L) is composed of a matrix, which consists of NaCl crystals and porous iron particles partially coated with $FeCl_2$, and a molten electrolyte, a mixture of $AlCl_3$ and NaCl. Transport equations are derived from Pollard and Newman's [3] study for a mixture of two binary molten salts with a common ion in a porous electrode. As in their study, A and B are used for $NaAlCl_4$ and NaCl salts and 1, 2 and 3 are used for $AlCl_4^-$, Cl^- and Na^+ ions, respectively.

The electrolyte is a concentrated solution of $AlCl_4^-$, Cl^- and Na^+ [3]. From solvent-equilibria studies of $AlCl_3$-NaCl melts, it is known that the electrolyte also contains Al_2Cl_6, $AlCl_3$ and $Al_2Cl_7^-$ ions at low concentrations [4]. In addition to these ions, there is the soluble ferrous complex, most probably in the form of $Fe(AlCl_4)_4^{2-}$ [2, 5]. The concentrations of this ferrous complex on $FeCl_2$ and Fe surfaces and in the bulk may not be the same depending on the interfacial reaction rates. The schematic diagram of the Fe/$FeCl_2$ electrode defining the equilibrium, bulk and surface concentrations of the soluble ferrous complex can be seen in Figure 6.2.

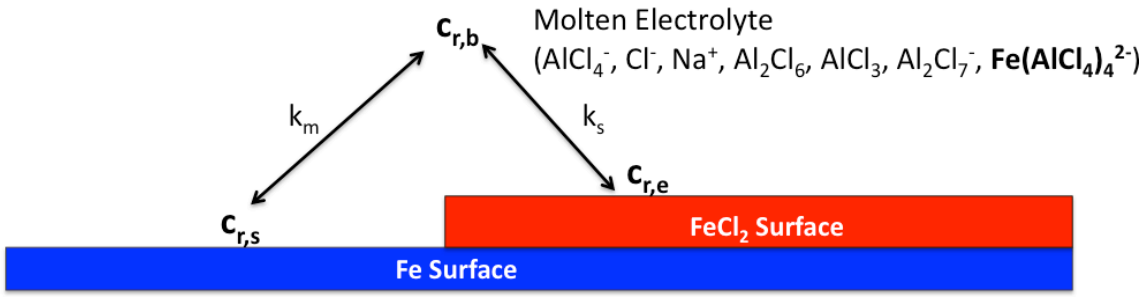

Figure 6.2. Schematic diagram of the Fe/$FeCl_2$ electrode showing the equilibrium, bulk and surface concentrations of the soluble ferrous complex, $Fe(AlCl_4)_4^{2-}$.

6.1.1. Solubility of $FeCl_2$

The equilibrium concentration of the complex on the $FeCl_2$ surface is dictated by the solubility of $FeCl_2$. In the previous models [2, 6], it was assumed that the solubility concentration of iron chloride, $c_{r,e}$, is constant within the cell. In this model, it is allowed to change within the cell as a function of radial position and time.

In a previous study [4], the solvent equilibrium of $AlCl_3$-NaCl melts is described, and three mole fraction equilibrium constants, K_0, K_2, and K_M were found. In this study, another equilibrium constant, $K_{sp,FeCl}$, is defined for the solubility of $FeCl_2$. Therefore, the equilibrium is now defined with the reactions 1, 2, 3 and 4:

$$2AlCl_{3(l)} \leftrightarrow Al_2Cl_{6(l)} \qquad K_0 \qquad (1)$$

$$AlCl_4^- + AlCl_3 \leftrightarrow Al_2Cl_7^- \qquad K_2 \qquad (2)$$

$$2AlCl_4^- \leftrightarrow Al_2Cl_7^- + Cl^- \qquad K_M \qquad (3)$$

$$FeCl_{2(s)} + 2Al_2Cl_7^- \leftrightarrow Fe(AlCl_4)_4^{2-} \qquad K_{sp,FeCl} \qquad (4)$$

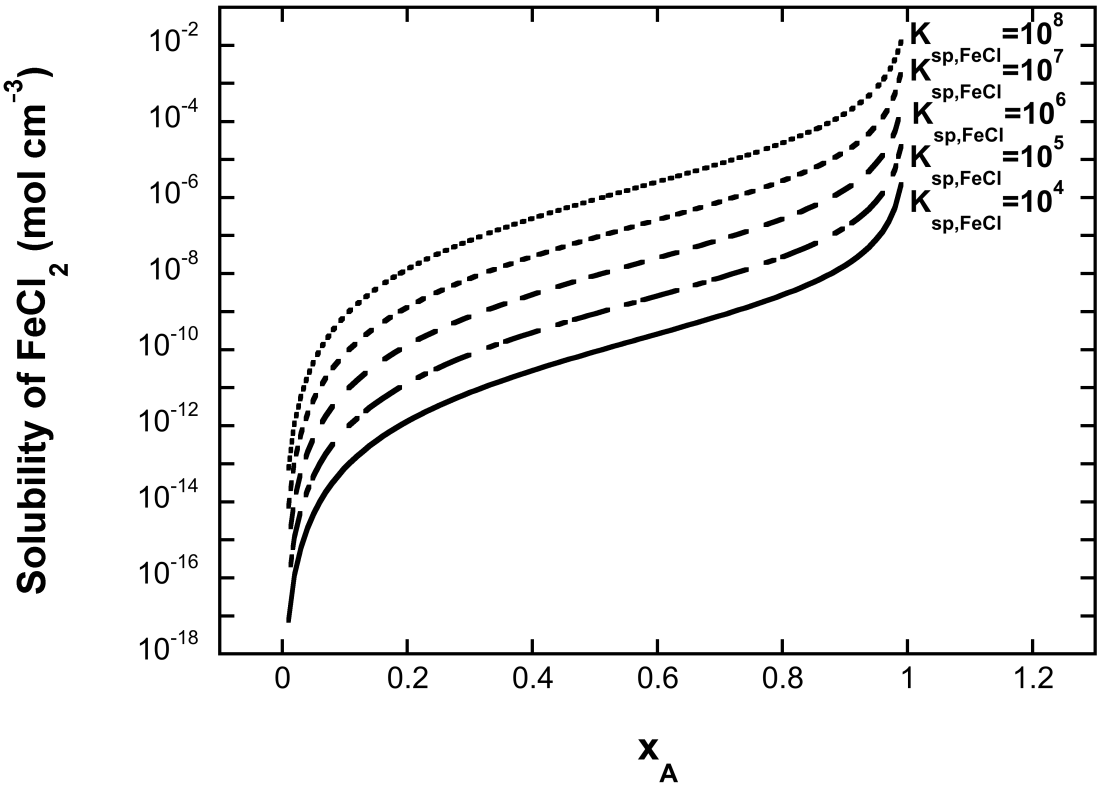

Figure 6.3. Solubility of $FeCl_2$, $c_{r,e}$ as a function of $NaAlCl_4$ mole fraction, x_A for different values of $K_{sp,FeCl}$ in a semi-log plot.

The solubility of $FeCl_2$, $c_{r,e}$, which is determined by these four equilibrium reactions, is only a function of the $NaAlCl_4$ mole fraction, x_A, and the assumed solubility constant, $K_{sp,FeCl}$. In Figure 6.3, the solubility as a function of x_A is shown for $K_{sp,FeCl}$ values between 10^4 and 10^8. It can be seen that, as $K_{sp,FeCl}$ increases, the solubility of $FeCl_2$ also increases. The model predicts a significant change in the solubility, especially for x_A values between 0.6 and 0.9. The assumed relationships for $c_{r,e}$ are given in the Appendix.

6.1.2. Concentration of the Soluble Ferrous Complex in the Electrolyte

The redistribution of iron in the cell as a result of cycling indicates there is a movement of the soluble ferrous complex within the cell. For this reason, the flux of $Fe(AlCl_4)_4^{2-}$ was included in the model. The electrolyte is a concentrated solution composed of $AlCl_4^-$, Cl^-, Na^+, Al_2Cl_6, $AlCl_3$, $Al_2Cl_7^-$ and $Fe(AlCl_4)_4^{2-}$ ions. Since the concentration of the species 1, 2 and 3 are very high compared to the other ions, in the derivation of the flux equation for the ferrous complex, the presence of Al_2Cl_6, $AlCl_3$ and $Al_2Cl_7^-$ ions were neglected. Thus the multicomponent diffusion equation [7] for the ferrous complex, equation 5, only contains species 1, 2, 3 and the ferrous complex, denoted with the subscript *r*:

$$c_{r,b}\nabla\mu_r = \frac{RT}{c_T}\left(\frac{c_{r,b}c_1}{D_{r1}}\left(v_1 - v_r\right) + \frac{c_{r,b}c_2}{D_{r2}}\left(v_2 - v_r\right) + \frac{c_{r,b}c_3}{D_{r3}}\left(v_3 - v_r\right)\right) \tag{5}$$

where μ_r is the electrochemical potential of the ferrous complex, c_T is the total concentration, $c_{r,b}$, c_1, c_2 and c_3 are the concentrations of the species and v_r, v_1, v_2 and v_3 are the velocities of the species.

Since we do not have independent measurement of the diffusion coefficients of the species, D_{ri}, we assume $D_{r1} = D_{r2} = D_{r3} = D_e$. Also since $c_{r,b} << c_1$, c_2 and c_3, we assume:

$$c_T \approx c_1 + c_2 + c_3 \tag{6}$$

and

$$c_T v^* \approx N_1 + N_2 + N_3 \tag{7}$$

where v^* is the molar-average velocity and N_1, N_2 and N_3 are the fluxes of the species.

With these assumptions, equation 5 is rewritten to give the flux of ferrous complex, N_r:

$$N_r = c_{r,b} v_r = -\frac{D_e}{RT} c_{r,b} \nabla \mu_r + c_{r,b} v^* \tag{8}$$

Inserting the Gibbs-Duhem equation, using the definition of the effective diffusion coefficient of the electrolyte, $D_e = D\varepsilon^{1.5}$, and neglecting electrical migration since the transference number of the iron species is essentially zero, equation 9 is obtained:

$$N_r = -D\varepsilon^{1.5} \nabla c_{r,b} + c_{r,b} v^* \tag{9}$$

A material balance of the soluble ferrous complex in the electrolyte enables calculation of the bulk concentration of $Fe(AlCl_4)_4^{2-}$, $c_{r,b}$. When the quasi steady-state assumption is applied, the mass transfer rate of ferrous complex from the $FeCl_2$ surface to the bulk is equal to the flux of ferrous complex in the electrolyte and the electrochemical reaction rate. The material balance for $c_{r,b}$ is shown in equation 10:

$$0 = -\nabla \cdot N_r + \frac{j}{2F} + k_s a_s (c_{r,e} - c_{r,b}) \tag{10}$$

where j is the local transfer current, k_s is the mass transfer coefficient of ferrous complex between $FeCl_2$ and bulk and a_s is the specific surface area of $FeCl_2$.

6.1.3. Concentration of the Soluble Ferrous Complex on the Fe Surface

The surface concentration, $c_{r,s}$, is calculated by equating the mass transfer rate of ferrous complex from the bulk to the Fe surface to the electrochemical reaction rate as given in equation 11:

$$\frac{j}{2F} = -k_m a_m (c_{r,b} - c_{r,s}) \tag{11}$$

where k_m is the mass transfer coefficient of ferrous complex between Fe and bulk and a_m is the specific surface area of Fe.

6.1.4. Reduction/Oxidation Reaction Rate

The reaction that takes place at the cathode is shown in equation 12:

$$FeCl_{2(s)} + 2e^- \leftrightarrow Fe_{(s)} + 2Cl^- \tag{12}$$

The reaction rate accounts for the mass transfer of ferrous complex from the bulk to the Fe surface as described in equation 13. This rate expression is a modification of the equation 13 in reference [2], with the appropriate changes for estimation of $c_{r,e}$ and $c_{r,b}$. All the other mass transfer rates and areas are the same with the previous studies [2, 6].

$$j = \frac{\exp\left(\frac{\alpha_a F}{RT}\eta\right) - \frac{c_{r,b}}{c_{r,e}}\exp\left(-\frac{\alpha_c F}{RT}\eta\right)}{\frac{1}{i_0 a_m} + \frac{1}{2Fc_{r,e}}\left(\frac{1}{k_m a_m}\right)\exp\left(-\frac{\alpha_c F}{RT}\eta\right)} \tag{13}$$

where the total overpotential, η, is given by:

$$\eta = \phi_1 - \phi_2 \tag{14}$$

At any point in the cell where the volume fraction of iron chloride is zero during the discharge, the transfer current is set to zero.

6.1.5. Precipitation Rate of NaCl

The second reaction taking place inside the porous cathode is the precipitation/dissolution reaction of NaCl, which is given by equation 15. The rate of this reaction is shown in equation 16 [2]. When x_A is equal to its saturation value, the rate is equal to zero. When it is lower than the saturation value, R_{NaClp} is positive indicating there is precipitation of NaCl in the cell.

$$Na^+ + Cl^- \leftrightarrow NaCl_{(s)} \tag{15}$$

$$R_{NaClp} = k_p\left(\frac{1 - x_A}{\bar{V}_e{}^2} - K_{sp,NaCl}\right) \tag{16}$$

where the average molar volume of the electrolyte, V_e:

$$\bar{V}_e = \left(\bar{V}_A - \bar{V}_B\right)x_A + \bar{V}_B \tag{17}$$

6.1.6. Precipitation Rate of $FeCl_2$

The precipitation rate of iron chloride is given by:

$$R_{FeCl_2p} = -k_s a_s (c_{r,e} - c_{r,b}) \tag{18}$$

The precipitation/dissolution rate is zero when the equilibrium and bulk concentrations of the ferrous complex are equal to each other. The rate is positive showing there is precipitation of $FeCl_2$ when the bulk concentration of the ferrous complex is higher than its equilibrium concentration.

6.1.7. Material Balances on Iron, Iron Chloride and Sodium Chloride

The equations used for the calculation of the volume fractions of iron, iron chloride and sodium chloride are shown in equations 19, 20 and 21, respectively. The

total solids porosity, ε, given in equation 22 is calculated based on the fact that the summation of the porosity and the volume fraction of the matrix is equal to 1.

$$\frac{\partial \varepsilon_{Fe}}{\partial t} = -\frac{\bar{V}_{Fe}}{2F} j \tag{19}$$

$$\frac{\partial \varepsilon_{FeCl_2}}{\partial t} = \bar{V}_{FeCl_2} R_{FeCl_2 p} \tag{20}$$

$$\frac{\partial \varepsilon_{NaCl}}{\partial t} = \bar{V}_{NaCl} R_{NaClp} \tag{21}$$

$$\frac{\partial \varepsilon}{\partial t} = \frac{\bar{V}_{Fe}}{2F} j - \bar{V}_{NaCl} k_p \left(\frac{1 - x_A}{\bar{V}_e{}^2} - K_{sp,NaCl} \right) + \bar{V}_{FeCl_2} k_s a_s (c_{r,e} - c_{r,b}) \tag{22}$$

6.1.8. Material Balance on Electrolyte

The mole fraction of $NaAlCl_4$, x_A, is the variable in the model used to set the composition of the electrolyte. A material balance is the same as given in reference [6]:

$$\varepsilon \frac{\partial x_A}{\partial t} = \bar{V}_e x_A R_{NaClp} + \bar{V}_e x_A \frac{j}{F} - v^* \nabla x_A + \nabla \cdot \left(D \varepsilon^{1.5} \nabla x_A \right) - D \varepsilon^{1.5} \frac{\left(\bar{V}_A - \bar{V}_B \right)}{\bar{V}_e} \left(\nabla x_A \right)^2 + \frac{\bar{V}_e i_2}{2F} \nabla x_A \tag{23}$$

6.1.9. Current Densities in Electrolyte and Matrix Phases

Ohm's law is used to define the current densities in the matrix and electrolyte phases, i_1 and i_2, that are shown in equations 24 and 25, respectively [2, 3, 6]. The summation of these two variables is equal to the apparent current density, I (measured at r_S) at any point in the cathode [2]. Effective conductivities of the metal and electrolyte are defined as $\sigma_e = \sigma \varepsilon^{1.5}$ and $\kappa_e = \kappa \varepsilon^{1.5}$ [2, 6]. In the derivations, the transference number of

sodium ion, t_3^* is assumed to be 0.5 since the sodium-ion concentration is half of the total concentration, and t_1^c and t_2^c are taken as x_A and x_B, respectively [2].

$$i_1 = -\sigma_e \nabla \phi_1 \tag{24}$$

$$i_2 = \frac{\sigma_e \kappa_e}{(\sigma_e + \kappa_e)} \left\{ \nabla \eta + \frac{r_S I}{\sigma_e r} + \frac{RTt_1^c}{F(1 - x_A)x_A} \left(1 + \frac{d \ln \gamma_A}{d \ln x_A} \right) \nabla x_A \right\} \tag{25}$$

$$i_1 + i_2 = \frac{I r_S}{r} \tag{26}$$

where ϕ_1 is the potential in the matrix phase and γ_A is the activity coefficient.

6.1.10. Local Transfer Current

The definition of the local transfer current is [2, 6]:

$$j = \nabla \cdot i_2 \tag{27}$$

6.1.11. Molar Average Velocity

The change in the porosity with time and position creates a velocity field inside the cell, which is given in equation 28 [2, 6]. This velocity within the cell results in the convective mass transfer of the species, therefore it must be considered in the model.

$$\begin{aligned} \nabla \cdot v^* = & -\frac{(\bar{V}_{Fe} + 2\bar{V}_B)}{2F} j + (\bar{V}_{NaCl} - \bar{V}_B) R_{NaClp} + (\bar{V}_A - \bar{V}_B) \nabla \cdot \left[D\varepsilon^{1.5} (c_A + c_B) \nabla x_A \right] \\ & + \frac{\bar{V}_A}{F} \nabla \cdot (t_1^* i_2) - \frac{\bar{V}_B}{F} \nabla \cdot (t_2^* i_2) - \bar{V}_{FeCl_2} k_s a_s (c_{r,e} - c_{r,b}) \end{aligned} \tag{28}$$

6.1.12. Total Iron Amount

In order to describe the movement of the iron in the cell, a parameter for the total iron amount is used to show iron redistribution within the battery:

$$Total_{Iron} = \frac{\varepsilon_{Fe}}{\bar{V}_{Fe}} + \frac{\varepsilon_{FeCl_2}}{\bar{V}_{FeCl_2}} + c_{r,b} \tag{29}$$

6.1.13. Cell Potential

One of the most important features of battery modeling is the prediction of the external cell potential. Reference [2] discusses the calculation of the terminal voltage in detail. In this study, a simplified version of their equation is used under the assumptions of constant reservoir and ceramic electrolyte resistances and constant negative electrode overpotential. With these assumptions, the change in potential with time can simply be calculated using:

$$V = V_{OC} + (\phi_1)_{r=r_0} - (\phi_2)_{r=r_L} + \left(\frac{RT}{F} \ln \frac{(1 - x_{Asat})}{(1 - x_A)} \right)_{r=r_L} \tag{30}$$

where V_{OC} is the open-circuit cell potential and ϕ_1 and ϕ_2 are the potentials in the matrix and electrolyte phases, respectively.

6.1.14. Initial Conditions

Since the cell is fully charged before the first discharge, the initial conditions for ε, ε_{Fe}, ε_{FeCl} and ε_{NaCl}, are 0.546, 0.184, 0.26 and 0.01, respectively [2, 6]. For the mole fraction of A, x_A, the saturation value of 0.8972 [6] is used. It is assumed that j is constant throughout the cell initially, and the initial conditions for the other 5 variables, Φ_1, Φ_2, i_1, i_2 and η, are calculated using this assumption. Finally, equation 31, which is derived using the fluxes of species 1, 2 and 3, is used for the initial condition of v^* [2].

$$v^* = \frac{\bar{V}_e - 2\bar{V}_B - \bar{V}_{Fe} + \bar{V}_{FeCl_2}}{2F} i_2 \tag{31}$$

6.1.15. Boundary Conditions

The boundary conditions at r_0 are given in equations 32-38:

$$i_2 = 0 \tag{32}$$

$$i_1 = \frac{Ir_s}{r_0} \tag{33}$$

$$\nabla\Phi_2 = 0 \tag{34}$$

$$\nabla\eta = -\frac{r_s I}{\sigma_e r_0} \tag{35}$$

$$\nabla x_A = 0 \tag{36}$$

$$v^* = 0 \tag{37}$$

$$\nabla c_{r,b} = 0 \tag{38}$$

The boundary conditions at r_L are:

$$i_2 = \frac{Ir_s}{r_L} \tag{39}$$

$$i_1 = 0 \tag{40}$$

$$\Phi_1 = 0 \tag{41}$$

$$\nabla x_A = 0 \tag{42}$$

$$v^* = \frac{\bar{V}_e - 2\bar{V}_B - \bar{V}_{Fe} + \bar{V}_{FeCl_2}}{2F} i_2 \tag{43}$$

$$\nabla c_{r,b} = 0 \tag{44}$$

The 14 variables in the model, Φ_1, Φ_2, i_1, i_2, j, η, x_A, ε, ε_{Fe}, ε_{FeCl}, ε_{NaCl}, v^*, $c_{r,e}$ and $c_{r,b}$, are calculated solving the equations 10, 13, 14, 19-28 and A6 using a block tri-diagonal matrix algorithm in FORTRAN [7]. The simulations were carried out with 501 node points and time-step sizes of 20.61 s during discharge and 9 s during charge. For

continuous cycling, time-step sizes of 6 s and 9 s are used for discharge and charge, respectively. In order to test the convergence, time-step size was halved, resulting in negligible changes in the results. In a similar manner, doubling of node points did not change the results to any appreciable extent.

6.2. Results and Discussion

Results are discussed assuming an operating temperature of 300 ^{0}C. The values of parameters used in the simulations are shown in Table 6.1. Most of these values are taken from previous work for sodium-iron chloride battery modeling [2, 4, 6]. For the electrical conductivity and activity coefficient equations, the equations in the Appendix of reference [2] were used. The full discharge time is calculated as 46040 s (12.8 h) with -30 mA cm^{-2} constant current discharging and the depth of discharge (DOD) is computed as the ratio of the actual discharge time to the full discharge time. The charge time is taken as 18000 s (5 h) in the simulations. In all of the results given for the model, $K_{sp,FeCl}$ is taken as 10^6, unless otherwise stated.

6.2.1. Solubility of $FeCl_2$ and Bulk Concentration of the Ferrous Complex

The change in iron chloride volume fraction, $NaAlCl_4$ mole fraction and solubility of $FeCl_2$ within the cell during discharge can be seen in Figures 6.4, 6.5 and 6.6, respectively. Initially (DOD=0), the solubility is constant along the cell since x_A is equal to its saturation value at every point in the cell. With increasing time (DOD=0.2), the solubility begins to decrease at the electrode-reservoir interface, r_L. This is expected since x_A has the same trend at DOD=0.2 (Figure 6.5) with the minimum value at r_L.

Table 6.1. Parameters in the model.

r_0	0.25 cm
r_L	2.5 cm
r_{Middle}	1.3705 cm
r_S	2.8 cm
H	30 cm
T	573 K
I	-30 mA cm^{-2} discharge/10 mA cm^{-2} charge
$\bar{V}_{Fe}$	7.1 cm^3 mol^{-1}
$\bar{V}_{FeCl_2}$	40.1 cm^3 mol^{-1}
$\bar{V}_{NaCl}$	27.0 cm^3 mol^{-1}
$\bar{V}_A$	121.6 cm^3 mol^{-1}
$\bar{V}_B$	37.06 cm^3 mol^{-1}
k_p	0.1 cm^3 mol^{-1} s^{-1}
$K_{sp,NaCl}$	8.06 x 10^{-6} mol^2 cm^{-6}
$\alpha_a=\alpha_c$	1
D	5.135 x 10^{-6} cm^2 s^{-1}
σ	3.5 x 10^4 S cm^{-1}
K_0	3.85 x 10^5
K_2	10^3
K_M	2.37 x 10^{-6}
V_{OC}	2.32 V

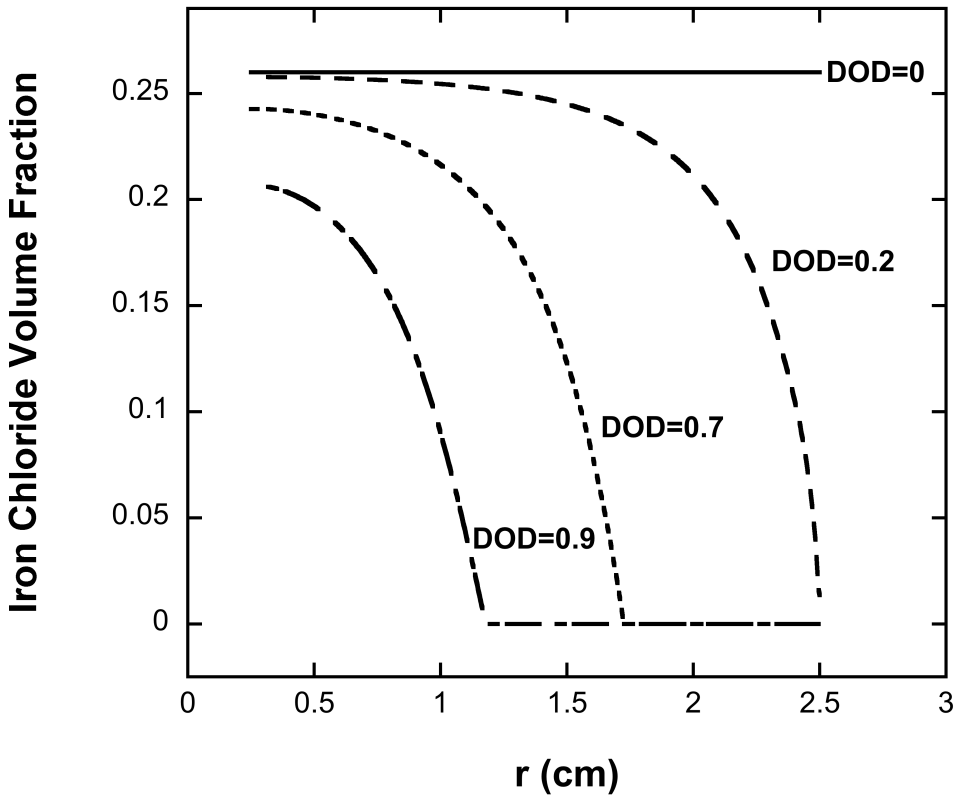

Figure 6.4. The change of iron chloride volume fraction, ε_{FeCl}, with radial position at different DODs during discharge ($K_{sp,FeCl}=10^6$).

For larger discharge times (DOD=0.7 and 0.9), the minimum value of x_A shifts inward to r_0 (Figure 6.5) and the solubility decreases throughout the cell with the same trend (Figure 6.6).

The bulk concentration of the ferrous complex with respect to position and time is shown in Figure 6.7. As it can be seen in the figure, at low discharge times (DOD=0.2) the bulk concentration follows the equilibrium concentration; it decreases with increasing *r*. As discharge time increases (DOD=0.7), although iron chloride is depleted near the electrode-reservoir interface (Figure 6.4), the concentration of the soluble ferrous complex in the electrolyte is not zero. This result shows that the flux of the ferrous

complex becomes more significant with increasing depth of discharge in part because $FeCl_{2(s)}$ is no longer present to buffer variations in the bulk iron concentration. As the discharge time increases further (DOD=0.9), the electrolyte concentration of iron approaches zero near the r_L boundary. At this high depth of discharge, iron chloride is depleted in the majority of the cell (Figure 6.4), and the electrolyte concentration of the ferrous complex is very low, even near r_0. Therefore, the flux of the ferrous complex is negligibly small; it is not enough to create nonzero bulk concentrations near r_L.

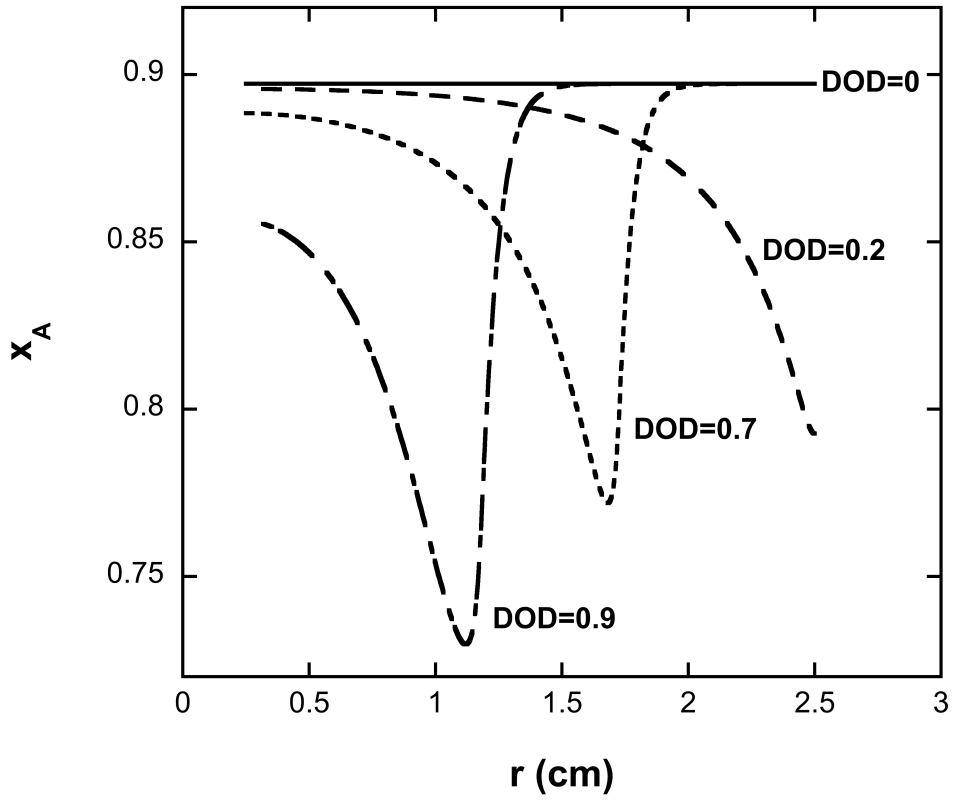

Figure 6.5. The change of $NaAlCl_4$ mole fraction, x_A, with radial position at different DODs during discharge ($K_{sp,FeCl}=10^6$).

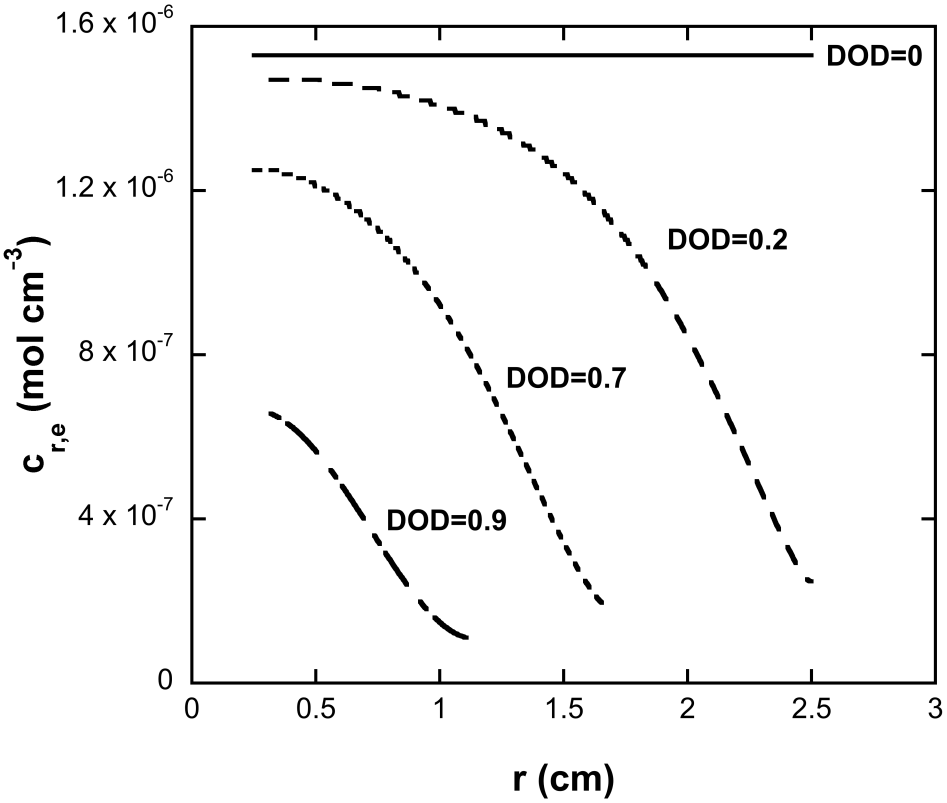

Figure 6.6. The change of solubility of $FeCl_2$, $c_{r,e}$, with radial position at different DODs during discharge ($K_{sp,FeCl}=10^6$).

The discontinuities seen in Figure 6.7 (DOD=0.7 and 0.9) occur at the points where the iron chloride phase is calculated to disappear. It is confirmed that the discontinuities do not propagate numerical errors.

6.2.2. Relocation of Iron Within the Cell

The change in the total iron amount at r_0, r_{Middle} and r_L during a discharge-charge cycle is shown in Figure 6.8. In the figure, it can be seen that there is a sudden increase in the total iron amount at r_L during the early stages of discharge. This increase in total iron amount can be explained by a sharp increase in Fe concentration. This sharp increase

shows that there is a significant flux of the ferrous complex present towards r_L during the early stages of the discharge. After this initial increase, the total iron content does not change at r_L until the end of discharge. As the iron chloride is depleted near r_L, the reaction front migrates inward towards r_0, and the increase in Fe concentration also ends. This suggests that unlike the initial stages, the flux of the ferrous complex is not enough to create a change in Fe concentration or total iron amount. As discharge proceeds, $c_{r,b}$ also goes to zero and the total iron amount reflects only the Fe concentration at r_L. At r_{Middle} and r_0, the iron amount decreases slightly during discharge. These results show that there is a net flux of ferrous complex from r_0 to r_L.

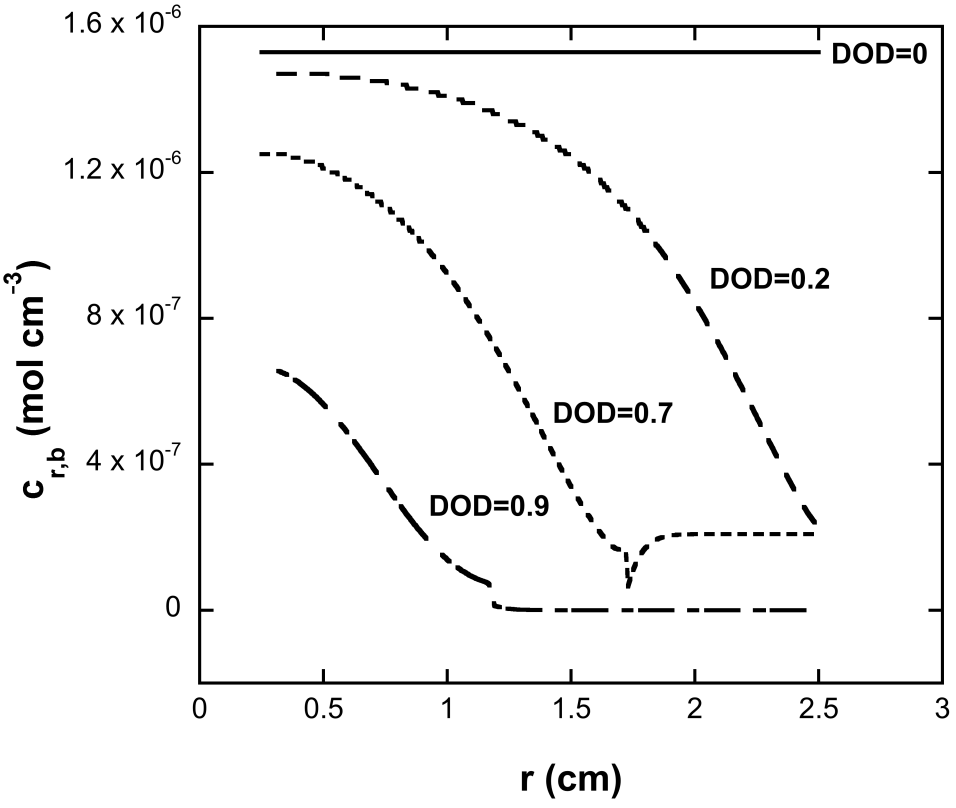

Figure 6.7. The change of bulk concentration of ferrous complex, $c_{r,b}$, with radial position at different DODs during discharge ($K_{sp,FeCl}$=10^6).

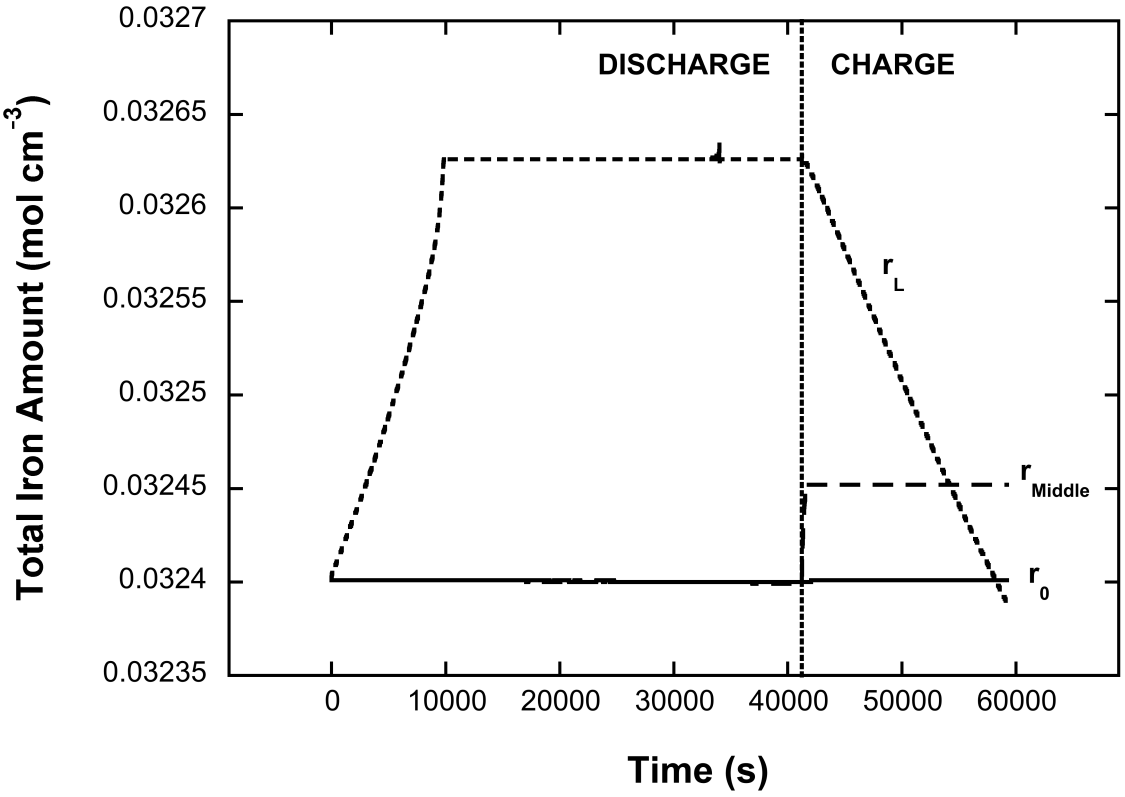

Figure 6.8. The change of total iron amount with time at different radial positions ($K_{sp,FeCl}$=10^6).

The flux of the ferrous complex is reversed during charging of the cell, causing the total iron amount to decrease at r_L and increase at r_{Middle} and r_0. As a result of a discharge-charge cycle, the total amount of iron is reduced slightly at r_L. This small change in the total iron amount as a result of one cycle may become significant after several dozen cycles.

6.2.3. Significance of Solubility of $FeCl_2$ Variation and Flux of the Ferrous Complex in the Model

In order to examine the role of the iron chloride solubility change and ferrous complex flux in the prediction of iron redistribution inside the cell, four model predictions are compared. In the first model, the solubility of iron chloride is constant throughout the cell at its saturation value. In addition, the flux of the ferrous complex is not included in the material balance of the ferrous complex in the bulk. This first model is essentially identical to Sudoh and Newman's model [2, 6]. In the second model, the solubility of iron chloride is constant throughout the cell, but the flux of the ferrous complex is included. In the third model, the variation in $FeCl_2$ solubility is taken into account, but the flux is not included. Finally, the fourth model is the one described in this chapter; counting for both the solubility change and ferrous complex flux inside the cell. In order to compare these four models, the bulk concentration profile at DOD=0.7 is chosen as shown in Figure 6.9.

When the models with no flux (models 1 and 3) are compared with the models accounting for the flux of the ferrous complex (models 2 and 4) in Figure 6.9, it can be seen that the presence of the flux in the model resulted in prediction of higher bulk concentrations near the r_L boundary. For instance, the bulk concentration is non-zero for model 4 near the r_L boundary although it is zero for model 3. From these results it can be concluded that the effect of the flux of the ferrous complex is significant at moderate DODs near r_L, where iron chloride is depleted.

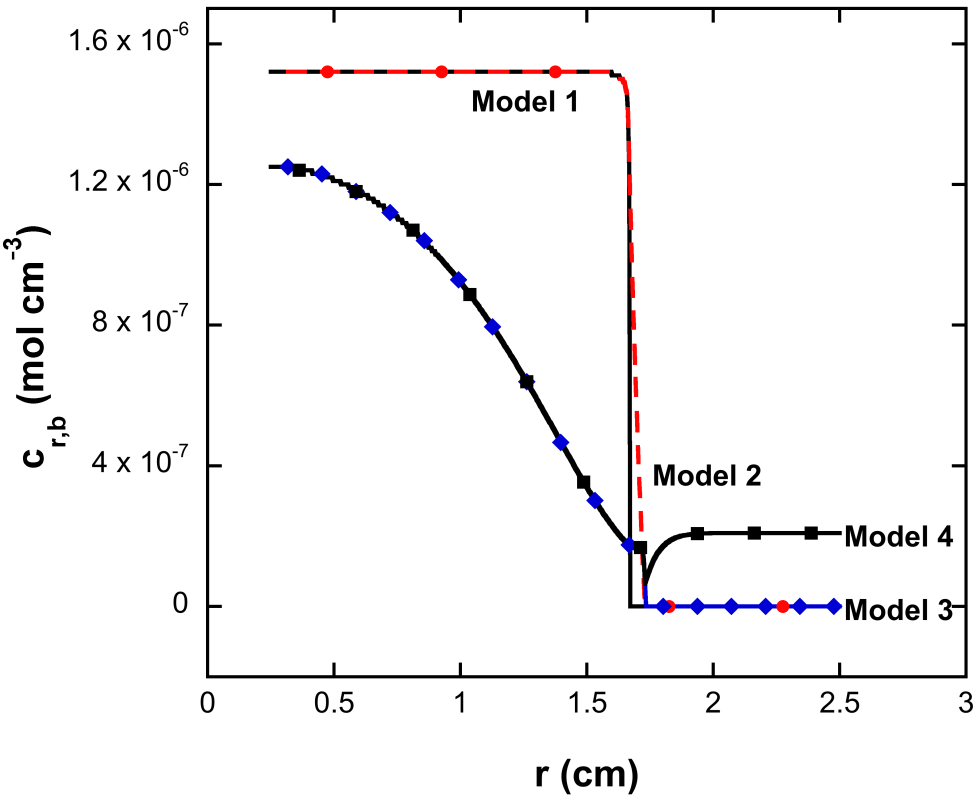

Figure 6.9. Comparison of bulk concentration results for the complete model (model 4 - flux, variable solubility) and different simplifications (model 1 - no flux, constant solubility, model 2 - flux, constant solubility, model 3 - no flux, variable solubility). For all cases DOD=0.7 and $K_{sp,FeCl}=10^6$.

The effect of variation of $FeCl_2$ solubility on the electrolyte concentration is also apparent in Figure 6.9, especially near r_0, where solid iron chloride is still present. Electrolyte concentration does not change near r_0 for the models with constant solubility (models 1 and 2) whereas it decreases with radial distance for models with variable solubility (models 3 and 4). The variation in $c_{r,e}$ results in lower electrolyte concentrations near this boundary.

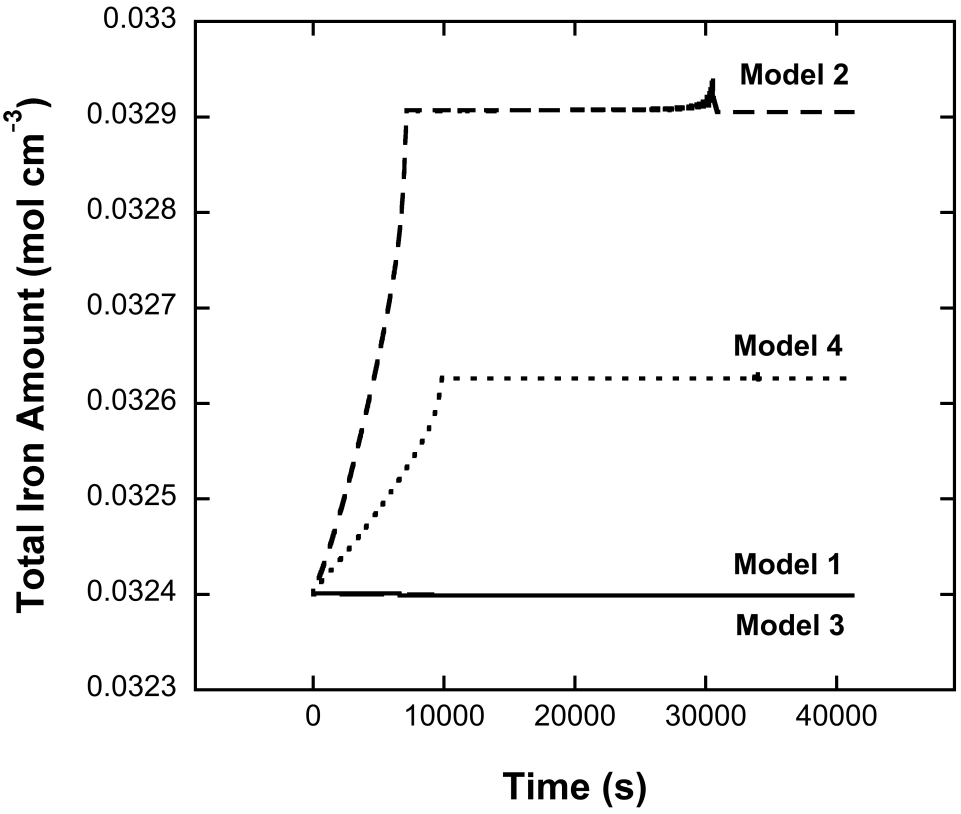

Figure 6.10. Comparison of total iron amount results for the complete model (model 4 - flux, variable solubility) and different simplifications (model 1 - no flux, constant solubility, model 2 - flux, constant solubility, model 3 - no flux, variable solubility). For all cases DOD=0.7 and $K_{sp,FeCl}=10^6$.

In Figure 6.10, the total iron amount at r_L as a function of discharge time for these four models are compared. This figure clearly displays the importance of the flux of the ferrous complex in the redistribution of the iron inside the cell since models 2 and 4 exhibit a significant change in the total iron amount. The increase in total iron amount predicted by model 2 is higher than model 4 since in model 2, solubility of $FeCl_2$ is constant at its maximum value. It can be concluded that although the variation in the

$FeCl_2$ solubility is important, the addition of the flux of the ferrous complex into the model has a more important effect on the results.

6.2.4. Effect of $K_{sp,FeCl}$ on the Discharge-Charge Cycle of the Cell

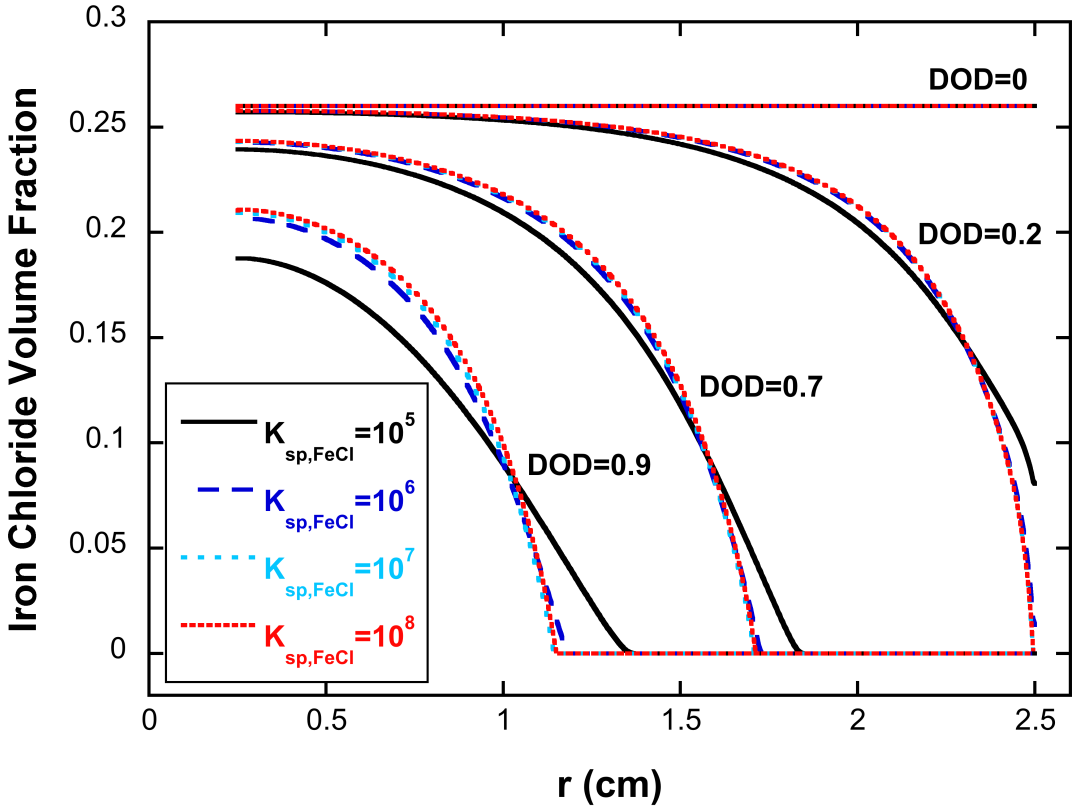

Figure 6.11. Comparison of iron chloride volume fraction profiles for different $K_{sp,FeCl}$ values during discharge.

The solubility product, $K_{sp,FeCl}$, has not been previously reported in the literature. Sudoh and Newman [2] assumed a constant equilibrium ferrous complex concentration of 4.1 x 10^{-8} mol cm^{-3} in their study. This value of $c_{r,e}$ corresponds to $K_{sp,FeCl}$ of 2.7 x 10^4 calculated at the saturation value of x_A according to our model. We have carried out

simulations for assumed values of 10^4, 10^5, 10^6, 10^7 and 10^8. When $K_{sp,FeCl} < 10^5$, model predictions are not in accord with the previous results reported, most probably because $c_{r,e}$ is too low in the system, seriously affecting the kinetics. The results show consistent behavior for all $K_{sp,FeCl}$ values only when it is equal or higher than 10^5. $K_{sp,FeCl}$ values higher than 10^8 are not considered since the main assumption in our model is that iron chloride is sparingly soluble in the electrolyte and this range leads to too high of a concentration.

Iron chloride volume fractions with respect to position and time for $K_{sp,FeCl}$ values of 10^5, 10^6, 10^7 and 10^8 are shown in Figures 6.11 and 6.12, for discharge and charge, respectively. During discharge, for all $K_{sp,FeCl}$ values, the same trend is seen; ε_{FeCl} decreases with time throughout the battery and it becomes depleted for positions approaching r_L at high DODs since the reaction front migrates inwards towards the positive current collector [8]. When the curves for different solubility products are compared, it can be seen that there is a significant difference in the results only when $K_{sp,FeCl}$ is equal to 10^5 (Figure 6.11). The results for the other three $K_{sp,FeCl}$ values are very similar. The difference between the 10^5 curve and the others increases with increasing DOD. For $K_{sp,FeCl}$ values of 10^6 and higher, iron chloride is depleted faster than $K_{sp,FeCl} = 10^5$ near the r_L boundary due to higher reaction rates. When comparing curves with the same DOD, a higher local transfer current at r_L must result in a lower local transfer current at r_0. Therefore the iron chloride volume fraction is lower at r_0 for $K_{sp,FeCl} = 10^5$ relative to the higher $K_{sp,FeCl}$ values.

In contrast, during charge, the value of $K_{sp,FeCl}$ appears to affect behavior near the r_L boundary. As it can be seen in Figure 6.12, there is a sudden decrease for ε_{FeCl} at r_L for

10^8. This result suggests that the equilibrium value of the ferrous complex has a significant effect on ε_{FeCl} at the r_L boundary when $K_{sp,FeCl}$ is higher than 10^7. This effect is not seen during discharge at the r_L boundary because $FeCl_{2(s)}$ is depleted for any value of the solubility product.

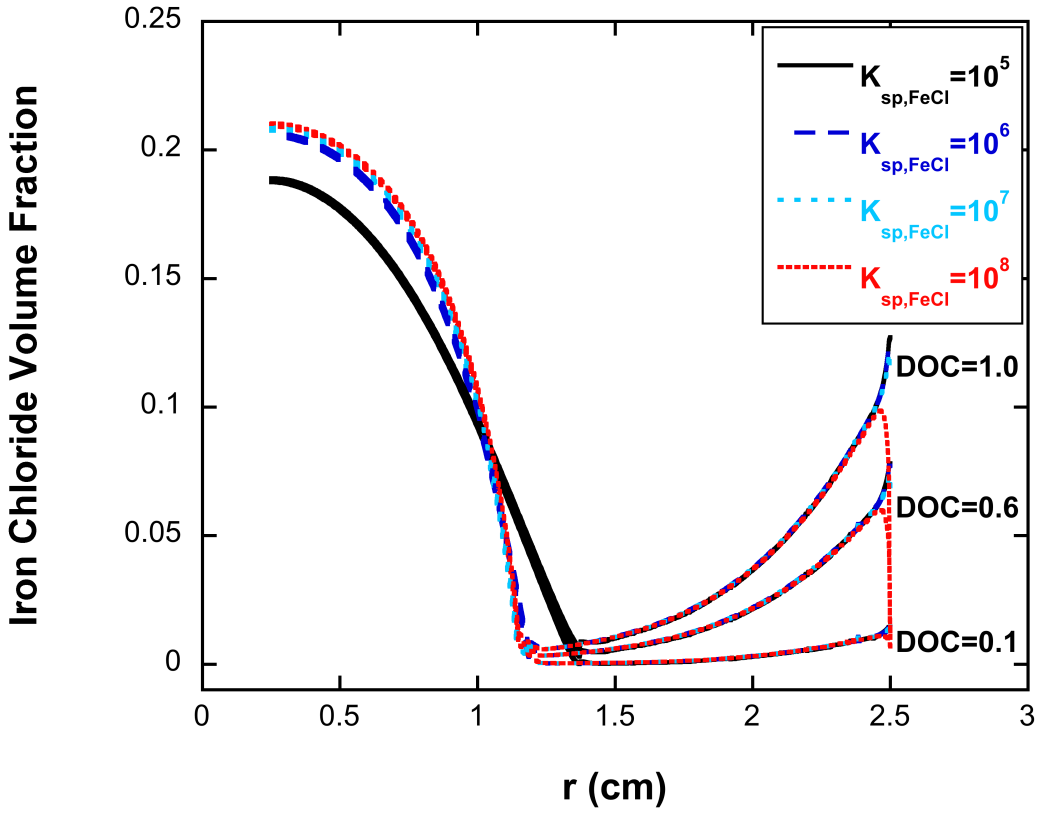

Figure 6.12. Comparison of iron chloride volume fraction profiles for different $K_{sp,FeCl}$ values during charge.

The change in the cell potential with time during discharge for different values of $K_{sp,FeCl}$ can be seen in Figure 6.13. The trend for all of the curves is the same; it starts with a slight decrease in the cell potential at small DODs, then a significant continuous decrease is observed, and finally at very high DODs, a very steep decrease occurs. All

four curves are the same until 35000 s. After this point there is a clear difference among the curves; they have the steep potential decrease at different times. As for the previous results, $K_{sp,FeCl} = 10^5$ has the most significant distinction from the others. The reason why the steep potential decrease is seen earlier for lower $K_{sp,FeCl}$ values can be explained by the slower kinetics at the reaction front in these systems due to the low electrolyte concentration of ferrous complex. The reaction rate at the reaction front is significantly lower for lower $K_{sp,FeCl}$ values, especially for $K_{sp,FeCl} = 10^5$.

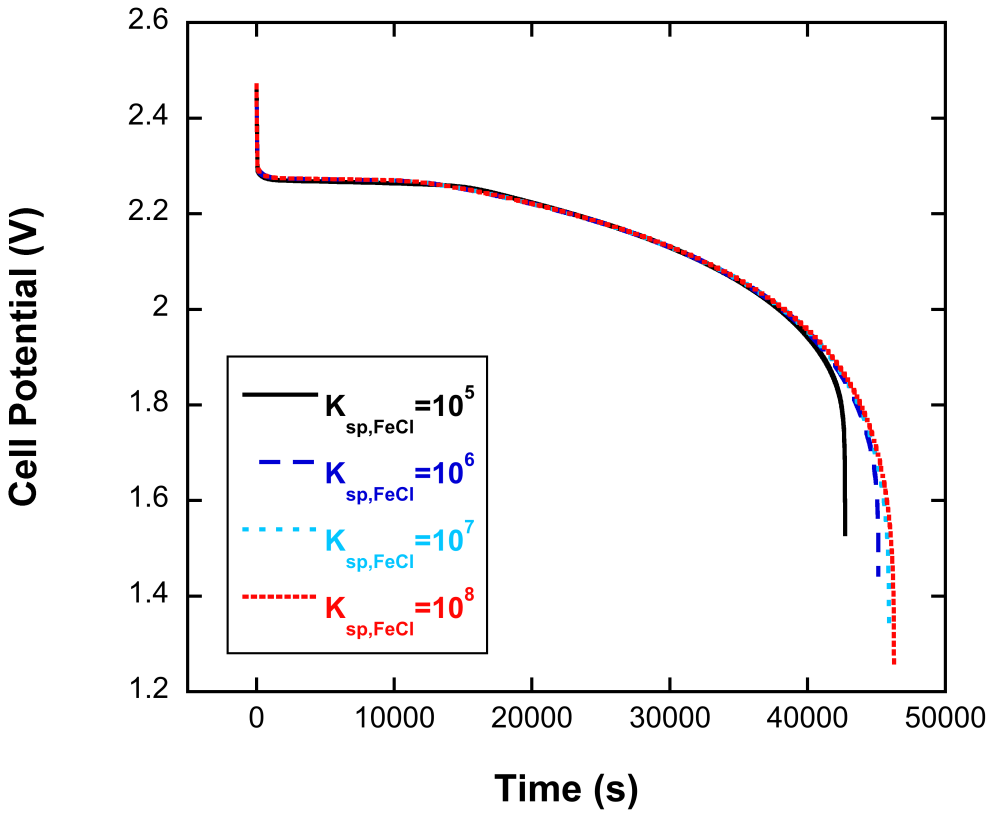

Figure 6.13. Comparison of cell potentials for different $K_{sp,FeCl}$ values during discharge.

The effect of $K_{sp,FeCl}$ on the cell potential is observed only at very high DODs, suggesting that the sharp potential decrease occurs when reaction rates at the reaction

front decreases to very low values. In terms of the cell potential, increasing the solubility product higher than 10^7 does not have a great impact on the simulated cell potential except near the end of discharge.

6.2.5. Effect of Continuous Cycling

Continuous cycling simulations were conducted to study whether iron redistribution continued beyond the first cycle. Here, the cycling conditions are taken as discharge for 12000 s at -30 mA cm^{-2} and charge for 18000 s at 10 mA cm^{-2}. The effect of continuous cycling was investigated for five cycles.

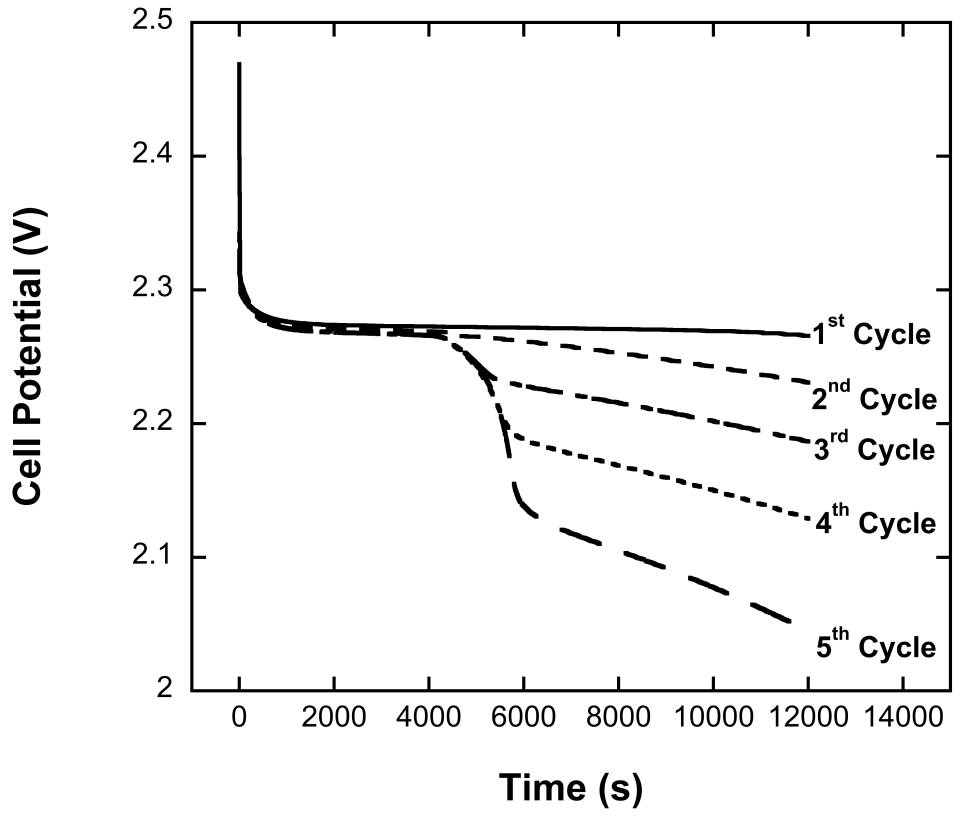

Figure 6.14. The change of discharge cell potential with time for each cycle during continuous cycling ($K_{sp,FeCl}$=10^6).

In Figure 6.14, the change of cell potential with time during discharge is given for each cycle. It can be seen that under these cycling conditions, the cell potential is predicted to decrease even after 5 cycles. In addition, with cycling the trend of the potential curve also changes; there is a steep decrease in the potential at first followed by a slighter continuous decrease. This sudden potential decrease starts to occur around the same DOD at each cycle. As a result of the simulation, it has been calculated that after the 5th discharge, the cell potential decreases by nearly 10%. The change in the discharge potential curve and decline in discharge potential with continuous cycling has been reported previously [9]. The redistribution of iron inside the cathode with continuous cycling plays an important role in this potential loss. It should be kept in mind that the discharge/charge current densities and simulation times also have a great impact on the calculated potential loss. Therefore, this extreme of potential decrease may not be seen with different cycling conditions. In addition, it has seen that cell design has a critical effect on the calculated potential loss. For instance, simulations suggest that the initial volume fraction ratio of iron to iron-chloride creates a significant difference in the calculated potential loss.

The change in total iron amount at r_0, r_{Middle} and r_L with continuous cycling can be seen in Figure 6.15. In the previous section, a single discharge-charge cycle was investigated and, as a result of the simulations, it was seen that iron amount increases at r_L during discharge and decreases during charge. The same trends can be seen for each individual cycle in Figure 6.15. As explained in the previous section, the initial increase is mainly due to the sharp increase in iron volume fraction because of the significant flux of the ferrous complex. After iron chloride is depleted, the increase in the total iron

amount ends and the curve stabilizes. During charging, the ferrous complex diffuses away from r_L, causing the Fe concentration to decrease more than the $FeCl_2$ amount and the bulk concentration to increase. The figure also shows that with increased cycling, the iron depletion at r_L at the end of charging becomes more and more significant. For instance, as a result of the simulation, the total iron amount decreases by ~1% at r_L at the end of the fifth cycle. This result suggests that iron may be depleted at r_L around the end of 500th cycle causing perhaps the failure of the cell. The change in the iron amount at r_0 and r_{Middle} with continuous cycling is not as significant as the change in r_L.

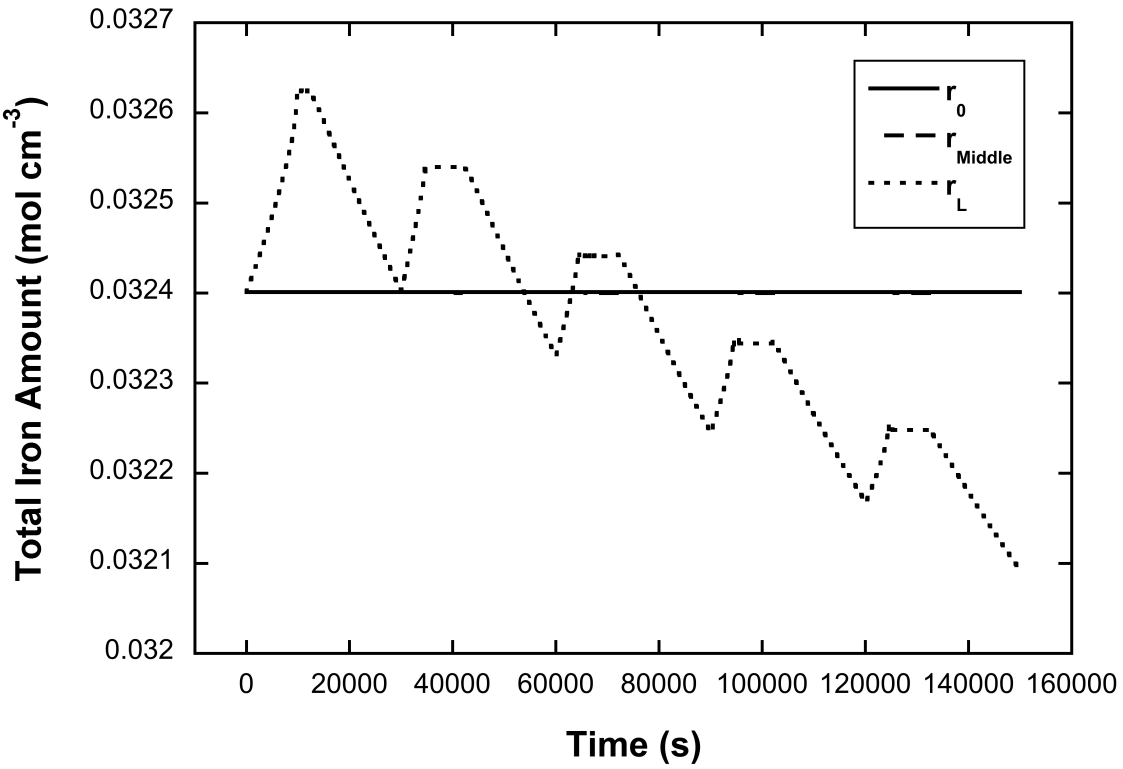

Figure 6.15. The change of total iron amount with time at different radial positions during continuous cycling ($K_{sp,FeCl}$=10^6).

Since the molar average velocity at r_L is not zero, there is a net flux of the soluble ferrous complex into the sodium tetrachloroaluminate reservoir as a result of continuous cycling. However it was calculated that the amount of iron that is lost into the reservoir due to this flux is negligible compared to the total decrease in the iron amount at this boundary. Therefore, the redistribution of iron within the electrode must be the main reason of the iron loss at r_L.

Minimizing the transport and redistribution of iron inside the cathode should be considered in the cell design in order to prevent the power loss seen as a result of continuous cycling. The model proposed in this study is able to predict the iron redistribution inside the cell as a function of design parameters. For instance, it has been seen that one of the design parameters in Zebra cells, the initial ratio of iron to iron-chloride volume fraction, has a significant effect on iron redistribution inside the cell. Simulations suggest that increasing the initial ratio of iron to iron-chloride volume fraction decreases the amount of iron depleted at r_L.

The results reported in this chapter show that incorporation of the variation of iron chloride solubility and the flux of the ferrous complex into the model of the porous cathode is important to predict the redistribution of the metal inside the cell. For future work, the iron chloride solubility as a function of x_A would be valuable to measure directly. Furthermore the metal distribution inside the cathode at different positions at different DODs would allow for direct testing of model predictions. In addition, extending the model proposed to a $Na/NiCl_2$ cell would be of value since it is known that $Na/NiCl_2$ batteries have some superior properties over $Na/FeCl_2$ batteries, such as higher open-circuit potential [8, 10].

6.3. Summary

In this chapter, a mathematical model for the positive cathode in a sodium-iron chloride cell with β"-alumina ceramic and molten $NaAlCl_4$/NaCl electrolyte was extended by accounting for variable solubility of $FeCl_2$. In addition to the solubility of iron chloride, this model also predicts the movement of iron inside the cell with time. It has seen that during discharge the solubility of $FeCl_2$ decreases near r_L as x_A decreases. The flux of the soluble ferrous complex becomes significant at moderate DODs leading to a non-zero electrolyte concentration of the complex although solid iron chloride is depleted near r_L. When the relocation of iron is considered, it was concluded that the net movement of iron is from r_0 to r_L during discharge, whereas the reverse happens during charge. The effect of solubility constant $K_{sp,FeCl}$ was also studied, and effects increase with increasing solubility, until 10^6. Finally, the effect of continuous cycling was examined. It was predicted that there is a deficiency of iron at r_L. As a result of the 5th cycle, there is nearly a 1% decrease in the total iron amount at the electrode-reservoir boundary.

6.4. Appendix - Calculation of the Equilibrium Concentration of the Ferrous Complex

The equilibrium concentration of the ferrous complex is calculated using the equations A1 through A6. The concentrations of $AlCl_4^-$, Cl^- and Na^+ are all expressed in terms of x_A.

$$x_{AlCl_3} = \frac{K_M x_A}{K_2\left(1 - x_A\right)} \tag{A1}$$

$$x_{Al_2Cl_6} = K_0 x_{AlCl_3}^2 \tag{A2}$$

$$x_{Al_2Cl_7^-} = \frac{K_M x_A^2}{c_T\left(1 - x_A\right)\bar{V}_e} \tag{A3}$$

$$x_{Fe(AlCl_4)_4^{2-}} = K_{sp,FeCl} x_{Al_2Cl_7^-}^2 \tag{A4}$$

$$c_T = \frac{2}{\bar{V}_e\left(1 - x_{Al_2Cl_6} - x_{AlCl_3} - x_{Al_2Cl_7^-} - x_{Fe(AlCl_4)_4^{2-}}\right)} \tag{A5}$$

$$c_{r,e} = c_T x_{Fe(AlCl_4)_4^{2-}} \tag{A6}$$

6.5. List of Symbols

a_m specific surface area of Fe, cm^{-1}

a_s specific surface area of $FeCl_2$, cm^{-1}

c_A concentration of $NaAlCl_4$, mol cm^{-3}

c_B concentration of NaCl, mol cm^{-3}

$c_{r,b}$ bulk concentration of ferrous complex, mol cm^{-3}

$c_{r,e}$ equilibrium concentration of ferrous complex, mol cm^{-3}

$c_{r,bsat}$ saturation bulk concentration of ferrous complex, mol cm^{-3}

$c_{r,esat}$ saturation equilibrium concentration of ferrous complex, mol cm^{-3}

$c_{r,s}$ surface concentration of ferrous complex, mol cm^{-3}

c_T total concentration, mol cm^{-3}

D diffusion coefficient of electrolyte, $cm^2\ s^{-1}$

D_e effective diffusion coefficient of electrolyte, $cm^2\ s^{-1}$

F Faraday's constant, C mol^{-1}

H height of the cell, cm

I apparent current density at separator, A cm^{-2}

i_0 exchange current density, A cm^{-2}

i_1 superficial current density in matrix phase, A cm^{-2}

i_2 superficial current density in electrolyte phase, A cm^{-2}

j local transfer current, A cm^{-3}

$K_{sp,FeCl}$ mole fraction equilibrium constant for the solubility of $FeCl_2$

$K_{sp,NaCl}$ solubility product of NaCl, mol^2 cm^{-6}

K_0, K_2, K_M mole fraction equilibrium constants for $AlCl_3$-NaCl solvent equilibrium

k_m mass transfer coefficient of ferrous complex between Fe and bulk, cm s^{-1}

k_s mass transfer coefficient of ferrous complex between $FeCl_2$ and bulk, cm s^{-1}

k_p rate constant for NaCl precipitation/dissolution reaction, cm^3 mol^{-1} s^{-1}

N_r flux of ferrous complex, mol cm^{-2} s^{-1}

R gas constant, J mol^{-1} K^{-1}

$R_{FeCl_2 p}$ precipitation/dissolution rate of $FeCl_2$, mol cm^{-3} s^{-1}

R_{NaClp} precipitation/dissolution rate of NaCl, mol cm^{-3} s^{-1}

r radial distance from the center of current collector, cm

r_0 outer radius of the current collector, cm

r_A outer radius of the separator, cm

r_C outer radius of the negative electrode, cm

r_L outer radius of the positive electrode, cm

r_S outer radius of the electrolyte reservoir, cm

T temperature, K

t time, s

t_1^c transference number of $AlCl_4^-$ relative to the common ion velocity

t_2^c transference number of Cl^- relative to the common ion velocity

t_3^* transference number of Na^+ relative to the molar-average velocity

$\bar{V}_A$ molar volume of molten $NaAlCl_4$ salt, $cm^3\ mol^{-1}$

$\bar{V}_B$ molar volume of molten NaCl salt, $cm^3\ mol^{-1}$

$\bar{V}_e$ molar volume of electrolyte, $cm^3\ mol^{-1}$

$\bar{V}_{Fe}$ molar volume of Fe, $cm^3\ mol^{-1}$

$\bar{V}_{FeCl_2}$ molar volume of $FeCl_2$, $cm^3\ mol^{-1}$

$\bar{V}_{NaCl}$ molar volume of NaCl precipitate, $cm^3\ mol^{-1}$

V cell potential, V

V_{OC} open-circuit cell potential, V

v^* molar-average electrolyte velocity, $cm\ s^{-1}$

x_A mole fraction of $NaAlCl_4$

x_{Asat} saturation mole fraction of $NaAlCl_4$

x_B mole fraction of NaCl

$x_{AlCl_3}, x_{Al_2Cl_6}, x_{Al_2Cl_7^-}, x_{Fe(AlCl_4)_4^{2-}}$ mole fractions of $AlCl_3$, Al_2Cl_6, $Al_2Cl_7^-$ and $Fe(AlCl_4)_4^{2-}$

Greek

α_a, α_c anodic and cathodic transfer coefficients

γ_A $NaAlCl_4$ activity coefficient

ε porosity

ε_{Fe} volume fraction of Fe

ε_{FeCl} volume fraction of $FeCl_2$

ε_{NaCl} volume fraction of NaCl precipitate

η total overpotential, V

κ Electrolyte conductivity, S cm^{-1}

κ_e Electrolyte effective conductivity, S cm^{-1}

σ Iron conductivity, S cm^{-1}

σ_e Iron effective conductivity, S cm^{-1}

ϕ_1 potential in matrix phase, V

ϕ_2 potential in electrolyte phase, V

6.6. References

1. D. Eroglu and A. C. West, *Journal of Power Sources*, **203**, 211 (2012).

2. M. Sudoh and J. Newman, *Journal of the Electrochemical Society*, **137**, 876 (1990).

3. R. Pollard and J. Newman, *Journal of the Electrochemical Society*, **126**, 1713 (1979).

4. L. G. Boxall, H. L. Jones and R. A. Osteryoung, *Journal of the Electrochemical Society*, **120**, 223 (1973).

5. L. G. Boxall, H. L. Jones and R. A. Osteryoung, *Journal of the Electrochemical Society*, **121**, 212 (1974).

6. M. A. Vallance and R. E. White, in *Comsol Conference*, Boston (2008).

7. J. Newman and K. E. Thomas-Alyea, *Electrochemical Systems*, Wiley-Interscience, Hoboken (2004).

8. X. Lu, G. Xia, J. P. Lemmon and Z. Yang, *Journal of Power Sources*, **195**, 2431 (2010).

9. J. S. Weaving and S. Walter Orchard, *Journal of Power Sources*, **36**, 537 (1991).

10. J. L. Sudworth, *Journal of Power Sources*, **51**, 105 (1994).

CHAPTER 7

CONCLUSIONS

In the first part of the dissertation, Ni/SiC co-deposition in the presence of a cationic dispersant, PEI was discussed. In Chapter 3, the effect of the dispersant on micro-particle incorporation was investigated. It has seen that the addition of PEI 60000 into the plating bath up to 200 ppm increases the SiC incorporation without decreasing the current efficiency. SiC fraction in the deposit increases with increasing rotation speed whereas it decreases at high current densities. PEI 1200 suppresses nickel deposition even at very low concentrations, however the SiC vol% is higher for the lower MW polymer. The stability of the SiC particles in the electrolyte was improved significantly with 1000 ppm PEI 60000. The pre-coating procedure developed for the SiC particles leads to high particle incorporation without significant suppression of Ni deposition. In addition, the stability of the suspensions was highly improved. Using these pre-coated particles was also beneficial in the presence of a leveling agent since the plating additives may change the impact of dispersants when they are introduced to the particles at the same time. Finally, it has seen that the efficacy of the pre-coating procedure at longer time scales was still satisfactory.

Ni/SiC co-deposition for the nano-particles was presented in Chapter 4. It has seen that the addition of 500 ppm PEI into the plating bath increases the SiC incorporation without suppressing Ni deposition. However the mechanical properties of the films are poor at this PEI concentration. Pre-coating SiC with PEI prior to plating is highly beneficial also for nano-particles; SiC vol% as high as 23% was obtained with

high particle stability in the electrolyte and high current efficiency. Both the SEM micrographs and surface roughness measurements show that pre-coating also resulted in smoother films.

Following the experimental characterization of Ni/SiC co-deposition for both micro- and nano-particles, the incorporation mechanism of the ceramic particles was described in Chapter 5 with a three-step model: (1) mass transfer of the particles to the electrode surface, (2) adsorption and (3) incorporation into the growing Ni film. In the proposed model, a particle on the electrode surface can only get incorporated if it stays long enough to get buried by the growing Ni film. Therefore, the incorporation rate depends on the residence and burial times of the particle and the number of particles adsorbed on the surface. According to the proposed model, the burial time of a particle is a function of current density and particle size. The residence time of a particle increases with rotation speed whereas it decreases with current density. Cationic dispersants also increase the residence time; in the modeling framework the enhanced SiC incorporation rate with PEI is through this increase in the residence time due to the tethering of the PEI molecules that are adsorbed on SiC surface to the electrode. The effect of particle size on the incorporation rate was also explained through the model; nano-particles are transported to the surface more readily, adsorb at higher number densities, have smaller burial times, but also decreased average residence times.

In the second part of the dissertation, a mathematical model for the porous cathode in a sodium-iron chloride cell was presented. A method to predict the $FeCl_2$ solubility as a function of $NaAlCl_4$ mole fraction and a defined solubility constant $K_{sp,FeCl}$ was described. It has seen that $FeCl_2$ solubility decreases within the cell with increasing

depth of discharge. The flux of the soluble ferrous complex was also included in the model; it has seen that the flux is significant at moderate depth of discharges near r_L resulting in a non-zero electrolyte concentration of the complex although iron chloride is depleted near this boundary. The model can also predict the relocation of iron within the cell. During discharge, the net movement of iron is from r_0 to r_L, whereas the reverse happens during charge. The effect of the solubility constant on the model predictions were also investigated to conclude that increasing $K_{sp,FeCl}$ does not affect the results significantly after $K_{sp,FeCl} = 10^6$. Finally the effect of continuous cycling was examined. The model predicts the iron to be depleted near r_L with continuous cycling. Simulations suggest that after the 5th cycle there is nearly a 1% decrease in the total iron amount at this boundary.